LOUGHBOROUGH UNIVERSITY

Modelling the electronic properties of CdSeTe solar cells

by

Evie Ingold

Supervisors: Prof. Michael Walls, Prof. Roger Smith, Prof. Pooja Goddard

A Master's Thesis submitted in partial fulfillment for the requirements
for the award of
Master of Philosophy of Loughborough University

August 2020

Abstract

by Evie Ingold

Cadmium telluride (CdTe) is an important material for photovoltaic applications because of its low cost and high efficiency. This efficiency may be increased further by alloying cadmium telluride with cadmium selenide (CdSe), to form cadmium selenium telluride (CdSeTe). Understanding the electronic and atomic structure of CdSeTe is important for understanding how to create the most efficient photovoltaic devices possible. In this study, density functional theory is used to model the behaviour of CdSeTe. An appropriate choice of functionals is developed, and these are used to analyse the properties of CdSeTe, including crystal structure, band structure, density of states, and molecular binding energies. Analysis of the results shows a good match between the predicted band gap and experimental results. The model is then used to explore the distribution of selenium within the CdSeTe, the free energy of mixing between CdTe and CdSe, and the formation energies of point defects with CdSeTe.

Contents

Chapter 1

Introduction

1.1 CdSeTe solar cells

Over the last several decades, CO_2 emissions have caused global temperatures to rise, affecting the climate across the world. Renewable forms of energy such as solar cells provide a solution to this problem, but more work needs to be done to increase efficiency and lower costs and technical issues.

Photovoltaic cells work by using a semiconductor whose band gap is at the appropriate level to absorb sunlight. An incident photon is absorbed, exciting an electron across the band gap and creating an electron-hole pair. The presence of a p-n junction within the semiconductor then serves to drive the electron and hole apart, creating a voltage that can be used to generate power.

Cadmium telluride (CdTe) is an important material for use in thin film solar cells due to its 1.5 eV direct band gap [1], which is well suited to absorbing solar radiation [2]. It is also the lowest cost solar technology due to the low materials usage and its relative ease of manufacture over competing technologies such as crystalline silicon and copper indium gallium selenide (CIGS). The current record for the conversion efficiency of a CdTe solar cell is 22.1% [3], with a theoretical maximum efficiency of 33% [4]. Figure 1.1 shows the increase in efficiency of solar cells over the past several decades.

Substituting selenium in place of tellurium at the front of the cell allows the band gap of the material to be tuned to increase current collection [6]. Although cadmium selenide

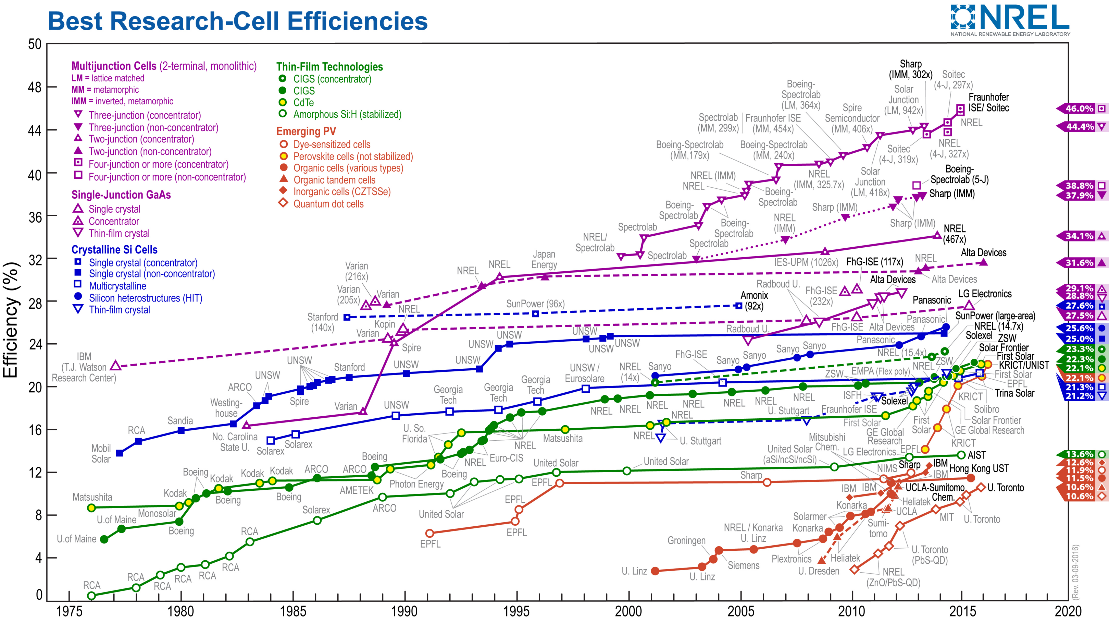

Figure 1.1: Record solar cell efficiencies for mainstream PV materials [5].

(CdSe) has a higher band gap than cadmium telluride, at 1.7 eV [1], alloyed CdSeTe can exhibit a reduced band gap depending on the selenium concentration, thanks to band gap bowing, allowing the cell to absorb solar radiation across a wider spectrum [6] and reducing losses at interfaces through improved band alignment. The introduction of selenium also improves efficiency by increasing carrier lifetimes [7]. Density functional theory (DFT) can be used to predict the effects of varying the Te:Se ratio on the properties of the system. The theoretical maximum efficiency of a single p-n junction solar cell is given by the Shockley-Queisser limit, which takes into account the blackbody radiation of the cell, energy lost due to the solar spectrum, recombination effects, and the atmosphere [4]. The value of this limit depends on the band gap of the solar cell, and peaks at 33.7% for an ideal cell (see figure 1.2) under AM1.5G conditions. AM1.5G refers to the optical path length relative to the depth of the atmosphere, as incoming sunlight travels at an angle through the atmosphere. AM1.5G conditions means that the sunlight is presumed to pass through 1.5 atmospheric thicknesses before reaching the ground, which approximately models the effect of the atmosphere at temperate latitudes.

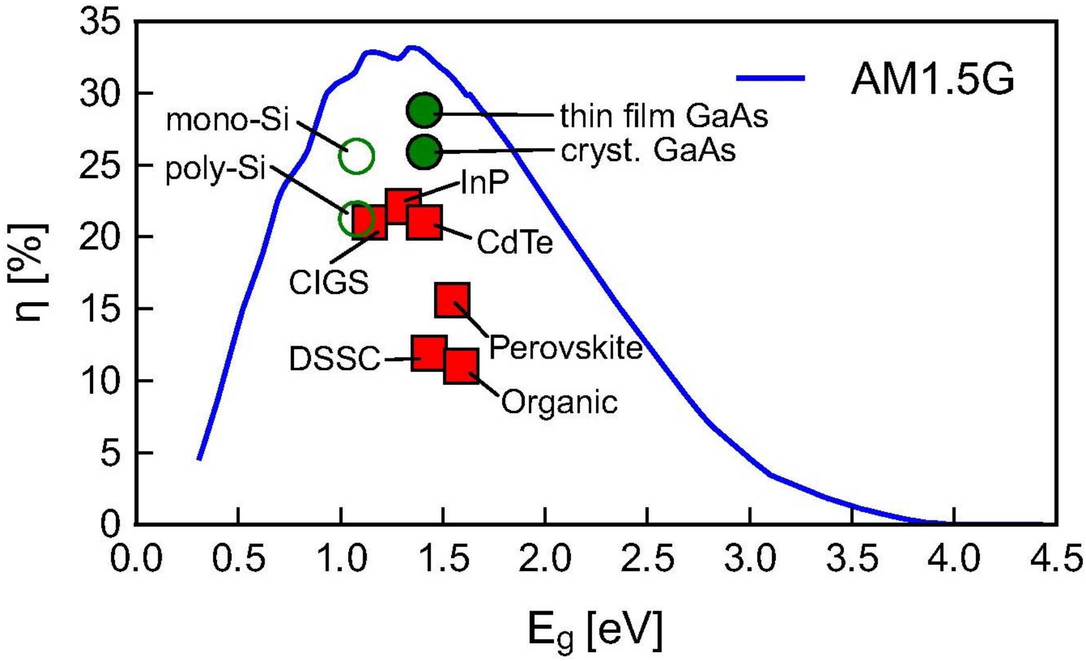

Figure 1.2: Shockley-Queisser limit under AM1.5G conditions as a function of band gap, with several materials' current record efficiency shown relative to their theoretical maximum efficiency. Adapted from Rühle [8].

1.2 Project goals

The aim of this project is to use density functional theory to model the effects of alloying selenium with cadmium telluride solar cells. This alloying is expected to improve the efficiency of these solar cells through a number of effects. Firstly, adding small amounts of selenium to the cell will lower the band gap slightly and increase the infrared response [6]. Secondly, it has been found that introducing selenium into the cell greatly increases the carrier lifetime, which improves efficiency [7]. Finally, grading the selenium concentration allows the band gap to be graded across the material. Band gap grading is known to increase efficiency in CIGS solar cells [9] and it is hoped that a similar effect will be observed in CdSeTe. To understand these effects, it will be useful to be able to model these devices so that their properties may be investigated without needing to manufacture prototypes.

In order to model these devices, we will use the Vienna *Ab initio* Simulation Package (VASP). VASP uses projector augmented-wave (PAW) [10] or Vanderbilt ultrasoft pseudopotentials with a plane-wave basis set well suited to tackling periodic systems. One issue with performing DFT calculations is that the electron wavefunction can oscillate sharply close to each atomic nucleus. This makes accurately capturing its behaviour difficult. To alleviate this, the PAW pseudopotentials replace the wavefunction close to each nucleus with an augmented version that is much easier to compute, while the wavefunction at a distance from the nucleus is maintained. Combined with the frozen-core approximation, that the inner electrons are unaffected by the atom's environment, this greatly increases the speed of any DFT calculation.

When performing DFT calculations with a plane-wave basis set, it is necessary to place an upper limit of the energy of plane waves included in the expansion of the wavefunction. Several properties of a material will also depend on integrals across the Brillouin zone. Since these integrals must be performed numerically, it is required to split the Brillouin zone into a number of discrete k-points [11]. The choice of energy cutoff and number of k-points is highly important. If they are set too low, the calculation will be inaccurate. As they are increased, the calculated properties of the material will tend towards a particular value. This is known as convergence. Setting them too high is wasteful, as once the results are well-converged, additional increases to the energy cutoff and number of k-points will have little effect on the accuracy of the simulation. As the size of the irreducible Brillouin zone is inversely proportional to the size of the unit cell, larger cells require smaller k-point grids to reach convergence. This can be used to save time when performing calculations on large cells.

To begin with, it will be necessary to establish which functional to use, and where to set the energy cutoff and number of k-points to obtain well converged results. LDA and GGA functionals are known to underestimate the band gaps of semiconductors, so a hybrid method must be used. HSE06 gives very accurate results for CdTe, but slightly underestimates the band gap of CdSe. B3LYP gives good results for CdSe [12], but overestimates the band gap of CdTe.

Once the appropriate method is decided, it should be a relatively straightforward matter to find the band gap of mixed systems. Once that has been achieved, the energy of point defects in these mixed systems will be analysed, which will hopefully lead to an explanation of the increased carrier lifetimes in CdSeTe.

1.3 CdTe and CdSe crystal structures

Both CdTe and CdSe exist in zinc blende and wurtzite crystal structures (see figure 1.3). Zinc blende is based on a face-centred cubic lattice while wurtzite is based on an hexagonal lattice. Cadmium telluride is most stable in the zinc blende structure [13], while cadmium selenide is marginally more stable as wurtzite [14]. For the mixed system of $CdSe_xTe_{1-x}$ (CST), experimental studies have found that a phase transition from zinc blende to wurtzite occurs at approximately $x = 0.6$ to 0.7 [6].

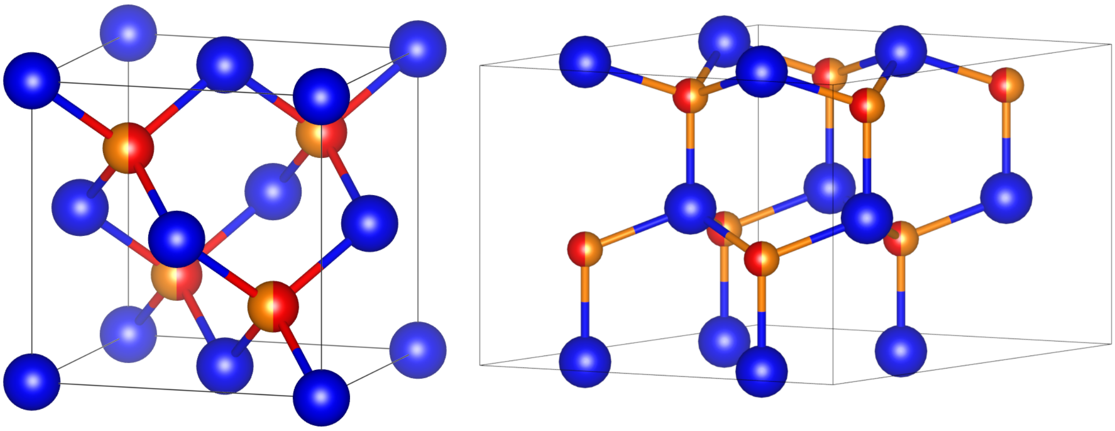

FIGURE 1.3: Zinc blende (left) and wurtzite (right) unit cells. Cadmium atoms are represented by blue while orange and red indicate selenium or tellurium atoms [15].

A cadmium telluride solar cell consists of a metal contact with a layer of CdTe deposited on top. The CdTe acts as the p-type material. A buffer layer, usually consisting of cadmium sulphide or magnesium zinc oxide, is then added, which acts as the n-type material, thereby forming a heterojunction. Next, a layer of transparent conductive oxide is added as a front contact, and finally a layer of glass to seal the cell. This is illustrated in figure 1.4.

After deposition, the cell has very poor efficiency, and must undergo an annealing treatment with cadmium chloride to raise the efficiency to viable levels. The precise mechanism that causes this increase in efficiency is unknown, but is believed to be due to passivation of grain boundaries by chlorine atoms. This is an area of active research.

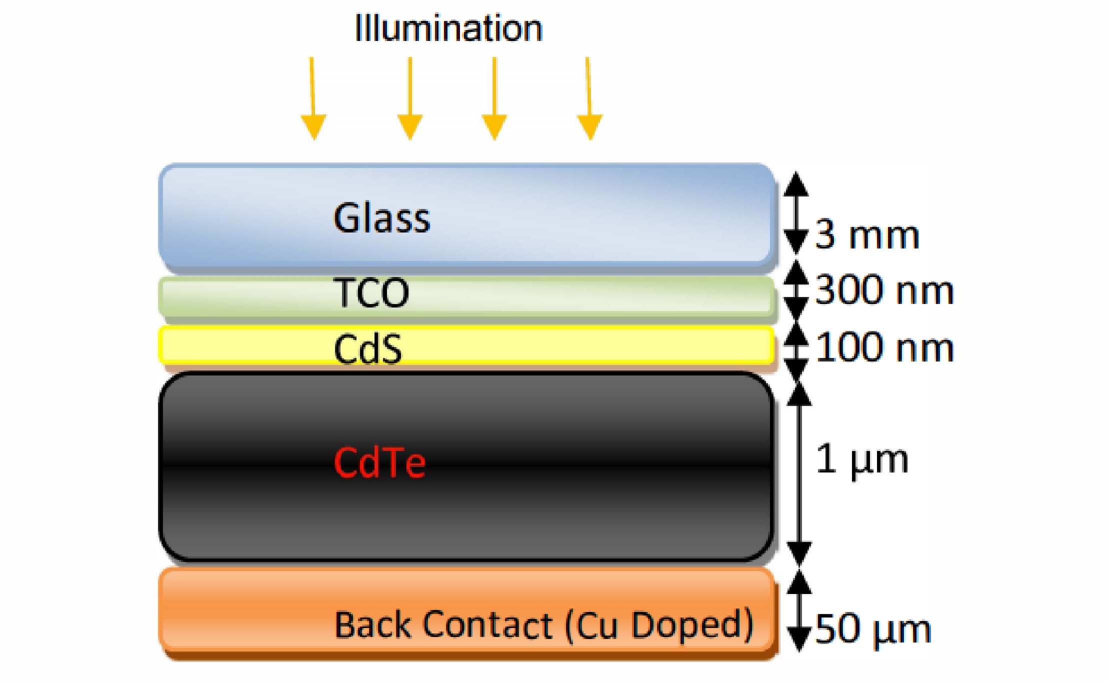

FIGURE 1.4: Structure of a CdTe thin film solar cell [16].

Chapter 2

Density Functional Theory

2.1 Kohn-Sham DFT

Density functional theory is a computational method for modelling the electronic structure of many-body quantum mechanical systems. It is based on the Hohenberg-Kohn theorems, which show that the energy of a many body system can be expressed in terms of a functional of the electron density. Minimising this functional then provides the correct ground state of the system [17]. This work was later expanded on by Kohn and Sham, who developed Kohn-Sham DFT, which reduces the problem of electrons interacting in a static potential to one of non-interacting particles in an effective potential [18]. In Kohn-Sham DFT, the wavefunction of an N-electron system satisfies a Schrödinger-like equation:

$$\left(-\frac{\hbar^2}{2m}\nabla^2 + V_{\text{eff}}(\mathbf{r})\right)\phi_i(\mathbf{r}) = \varepsilon_i\phi_i(\mathbf{r}) \tag{2.1}$$

where $V_{\text{eff}}(\mathbf{r})$ is the effective potential, $\phi_i(\mathbf{r})$ is the i-th Kohn-Sham orbital, and ε_i is the corresponding energy. The electron density is given by:

$$\rho(\mathbf{r}) = \sum_{i=1}^{N} |\phi(\mathbf{r})|^2 \tag{2.2}$$

The energy functional of the system is then given by:

$$E[\rho] = T[\rho] + \int V_{\text{ext}}(\mathbf{r})\rho(\mathbf{r})\,d\mathbf{r} + E_{\text{Coulomb}}[\rho] + E_{xc}[\rho] \tag{2.3}$$

where $T[\rho]$ is the kinetic energy of the electrons, given by:

$$T[\rho] = \sum_{i=1}^{N} \int \phi^{\star}(\mathbf{r}) \left(-\frac{\hbar^2}{2m} \nabla^2 \right) \phi(\mathbf{r})\, d\mathbf{r} \tag{2.4}$$

$V_{\text{ext}}(\mathbf{r})$ is the external potential acting on the electrons (this includes the electron-nuclei interaction), $E_{\text{Coulomb}}[\rho]$ is a Hartree term that takes into account electron-electron interaction:

$$E_{\text{Coulomb}}[\rho] = \frac{e^2}{2} \iint \frac{\rho(\mathbf{r})\rho(\mathbf{r}')}{|\mathbf{r} - \mathbf{r}'|}\, d\mathbf{r} d\mathbf{r}' \tag{2.5}$$

and E_{xc} is an exchange-correlation term. The precise form of the exchange-correlation functional is not known, and many methods and approximations have been developed to attempt to model it accurately [19]. Choosing the appropriate functional is an important aspect of performing DFT calculations.

2.2 Specific exchange-correlation functionals

A number of exchange-correlation functionals exist that may be used to calculate electronic states. These vary considerably in complexity, accuracy and computational cost.

2.2.1 Local density approximation

The simplest approximation is the local density approximation, or LDA, which makes the assumption that the functional depends only on the value of the electron density, and not, for instance, on its gradient. This is based on a homogeneous electron gas model, and gives an exchange-correlation functional of:

$$E_{xc}^{\text{LDA}}[\rho] = \int \rho(\mathbf{r}) \epsilon_{xc}(\rho)\, d\mathbf{r} \tag{2.6}$$

where $\epsilon_{xc}(\rho)$ is the exchange-correlation energy per particle of a homogeneous electron gas of density ρ. This can itself be broken down into a sum of exchange and correlation parts, such that:

$$E_{xc}^{\text{LDA}} = E_{x}^{\text{LDA}} + E_{c}^{\text{LDA}} \tag{2.7}$$

E_x^{LDA}, the exchange term, is exactly known, and is given by [20]:

$$E_x^{\text{LDA}} = -\frac{3}{4}\left(\frac{3}{\pi}\right)^{\frac{1}{3}} \int \rho(\mathbf{r})^{\frac{4}{3}}\, d\mathbf{r} \tag{2.8}$$

The correlation term E_c^{LDA} is known in the high and low density limits, and these results must be interpolated to derive intermediate values. Several interpolations exist, including the Vosko-Wilk-Nusair (VWN) method [21] and the Perdew-Zunger (PZ81) method [22].

2.2.2 Generalised gradient approximation

The generalised gradient approximation, or GGA, aims to improve on the local density approximation by including terms that depend on the gradient of the electron density. This gives more accurate results than the LDA or Hartree-Fock method [23, 24] As a result, GGA functionals are the most widely used functional in solid state physics. The typical form for a GGA functional is given by:

$$E_{xc}^{\text{GGA}} = \int \rho(\mathbf{r})\epsilon_{xc}(\rho)F_{xc}[\rho(\mathbf{r}), \nabla\rho(\mathbf{r})]\, d\mathbf{r} \tag{2.9}$$

where F_{xc} is the enhancement factor. This is often written in terms of a dimensionless parameter s, where:

$$s = \frac{|\nabla\rho|}{2k_F\rho} \tag{2.10}$$

where k_F is the Fermi wavevector, given by:

$$k_F = \left(3\pi^2\rho\right)^{\frac{1}{3}} \tag{2.11}$$

Unlike in the LDA, there is no general form for this enhancement factor, and several different variants exist. These include the Perdew-Wang (PW91) method [25, 26], Perdew-Burke-Ernzerhof (PBE) method [27] and the Becke-Lee-Yang-Parr (BLYP) method [28, 29].

2.2.3 Meta-GGAs

Meta-GGA methods attempt to extend the definition of the generalised gradient approximation to include terms depending on higher-order derivatives of the electron density in the exchange-correlation functional, as well as terms depending on the kinetic energy of the electron gas [30, 31]. Meta-GGAs provide greater accuracy than conventional GGAs in some cases [32], however, they are less widely used due to their increased computational cost.

2.2.4 Hybrid functionals

One weakness of GGA and LDA models is that they can fail to accurately capture the exchange interaction between electrons. An exact treatment of exchange can be found by the Hartree-Fock method [33], although this does not take into account the electronic correlation. Hybrid functionals combine the GGA exchange with the Hartree-Fock exchange term, like so:

$$E_{xc}^{\text{hybrid}} = \alpha E_x^{\text{HF}} + (1-\alpha)E_x^{\text{GGA}} + E_c^{\text{GGA}} \tag{2.12}$$

The E_x^{HF} Hartree-Fock exchange term for a system of N electrons is given by:

$$E_x^{\text{HF}} = -\frac{1}{2}\sum_{i=1}^{N}\sum_{j=1}^{N}\iint \frac{\phi_i^\star(\mathbf{r})\phi_i(\mathbf{r}')\phi_j^\star(\mathbf{r}')\phi_j(\mathbf{r})}{|\mathbf{r}-\mathbf{r}'|}\,d\mathbf{r}d\mathbf{r}' \tag{2.13}$$

where ϕ_i is the i-th Kohn-Sham orbital. This is not, strictly speaking, a true Hartree-Fock method, as Hartree-Fock does not use the Kohn-Sham orbitals, but in practice it is close enough [34].

A number of different hybrid models have been developed over the years. The following subsections will describe some of the more prominent ones used in computational quantum chemistry.

2.2.4.1 B3LYP

B3LYP is a mixing of the Becke 88 exchange functional E_x^{B88}, the Lee-Yang-Parr correlation functional E_c^{LYP}, the Vosko-Wilk-Nusair LDA functional $E_{xc}^{\mathrm{VWN}} = E_x^{\mathrm{LDA}} + E_c^{\mathrm{VWN}}$, and the Hartree-Fock exchange functional E_x^{HF} [35]. It is defined by:

$$E_{xc}^{\mathrm{B3LYP}} = 0.8E_x^{\mathrm{LDA}} + 0.2E_x^{\mathrm{HF}} + 0.72E_x^{\mathrm{B88}} + 0.81E_c^{\mathrm{LYP}} + 0.19E_c^{\mathrm{VWN}} \tag{2.14}$$

2.2.4.2 PBE0

PBE0 mixes the Hartree-Fock exchange energy E_x^{HF} with the PBE exchange energy E_x^{PBE} in a 1 to 3 ratio, and uses the full PBE correlation energy E_c^{PBE} [36]:

$$E_{xc}^{\mathrm{PBE0}} = \frac{1}{4}E_x^{\mathrm{HF}} + \frac{3}{4}E_x^{\mathrm{PBE}} + E_c^{\mathrm{PBE}} \tag{2.15}$$

2.2.4.3 HSE

The Heyd-Scuseria-Ernzerhof (HSE) hybrid functional is a modification of the PBE0 functional that breaks up the exchange terms into short-range and long-range terms, and then mixes these terms in certain proportions [37]. To break up the terms in this way, the $\frac{1}{r}$ term in the Coulomb potential is broken up into short range and long range terms:

$$\frac{1}{r} = \underbrace{\frac{\mathrm{erfc}(\omega r)}{r}}_{\text{short-range}} + \underbrace{\frac{\mathrm{erf}(\omega r)}{r}}_{\text{long-range}} \tag{2.16}$$

where ω is a parameter adjusting the ”short-rangedness” of the interaction. The use of the error function is arbitrary but convenient as it can be integrated analytically. Once this has been performed, the HSE functional takes the form:

$$E_{xc}^{\mathrm{HSE}}(\omega) = aE_x^{\mathrm{HF,\ short\ range}}(\omega) + (1-a)E_x^{\mathrm{PBE,\ short\ range}}(\omega) + E_x^{\mathrm{PBE,\ long\ range}}(\omega) + E_c^{\mathrm{PBE}} \tag{2.17}$$

Typical choices for the values of a and ω are $a = \frac{1}{4}$ and $\omega = 0.2$. This choice of parameters is knows as the HSE06 functional. For the case $\omega = 0$, HSE06 is equivalent to the PBE0 functional.

2.3 Other methods for DFT

2.3.1 DFT+U

One type of material that DFT fails to predict the properties of accurately is a Mott insulator [38]. This is because of the presence of strongly localised d or f electrons. Since the approximations used in DFT are based on a homogeneous electron gas model, DFT fails to accurately capture the behaviour of these localised electrons. To correct this, the Hubbard model [39] is used to explicitly describe the behaviour of these localised electrons, while DFT is used for s and p electrons. To achieve this, a Hubbard-like term is added onto the Hamiltonian [40]:

$$\hat{H}_{\text{Hubbard}} = \underbrace{\frac{U}{2} \sum_{m,m',\sigma} \hat{n}_{m,\sigma}\hat{n}_{m',-\sigma}}_{\text{electrons with opposite spin}} + \underbrace{\frac{U-J}{2} \sum_{m \neq m',\sigma} \hat{n}_{m,\sigma}\hat{n}_{m',\sigma}}_{\text{electrons with same spin}} \tag{2.18}$$

where $\hat{n}_{m,\sigma}$ is the number of electrons with spin σ and angular orbital projection m ($m = -2, -1, 0, 1, 2$ for d electrons), U is the on-site Coulomb repulsion energy, and J is the exchange energy.

Rearranging slightly and adding this to the DFT functional, we obtain:

$$E_{\text{DFT+U}} = E_{DFT} + \frac{U-J}{2} \sum_{m,\sigma} \left(n_{m,\sigma} - n_{m,\sigma}^2 \right) \tag{2.19}$$

It can be seen that in order to minimise the energy, the additional term will drive electron occupancy numbers to be either 0 or 1, which counteracts the tendency of DFT to delocalise these electrons [41].

2.3.2 Time dependent DFT

While density functional theory is capable of providing good approximations to ground states for many materials, it is incapable of handling excited states, as it is fundamentally based on the time-independent Schrödinger equation. Time-dependent DFT aims to rectify this by using the time-dependent Schrödinger equation instead. This is mathematically more complicated, but results in an analogue of the Hohenberg-Kohn theorems, called the Runge-Gross theorem, which shows that there exists a one-to-one mapping between the density of a many-body system and the potential in which it evolves [42]. The Kohn-Sham formalism can then be applied to this to give time-dependent Kohn-Sham DFT. One significant difference is that, since the energy in a time-dependent system is not necessarily conserved, energy functionals cannot be used. Instead, the state of the system is found using the stationary points of the system's quantum mechanical action [43].

Chapter 3

Choice of functional

For the initial stage of the project, it is necessary to find a suitable method within DFT for the study of CST alloy. Many studies of CdTe [44, 45] and CdSe [12] have been conducted using Density Functional Theory (DFT) but little theoretical work has been performed on mixed systems to date. To achieve this, it is important for the simulation parameters to provide accurate models of both CdSe and CdTe. However, electronic properties of semiconductors are difficult to model accurately with DFT, requiring the addition of the somewhat empirical Hubbard U parameters [38] or computationally expensive hybrid exchange-correlation functionals [33]. It is therefore necessary to obtain the optimal simulation parameters for an accurate description of CST using DFT methods.

3.1 Convergence parameters

All calculations were performed using the Vienna *Ab initio* Software Package (VASP) code [46].

We begin by determining the appropriate values for the plane-wave energy cutoff and k-point grid size. A unit cell of zinc blende cadmium telluride was constructed, and DFT single point calculations were performed with the PBE functional at different values of energy cutoff and k-point density. The free energies resulting from these calculations are shown in figure 3.1.

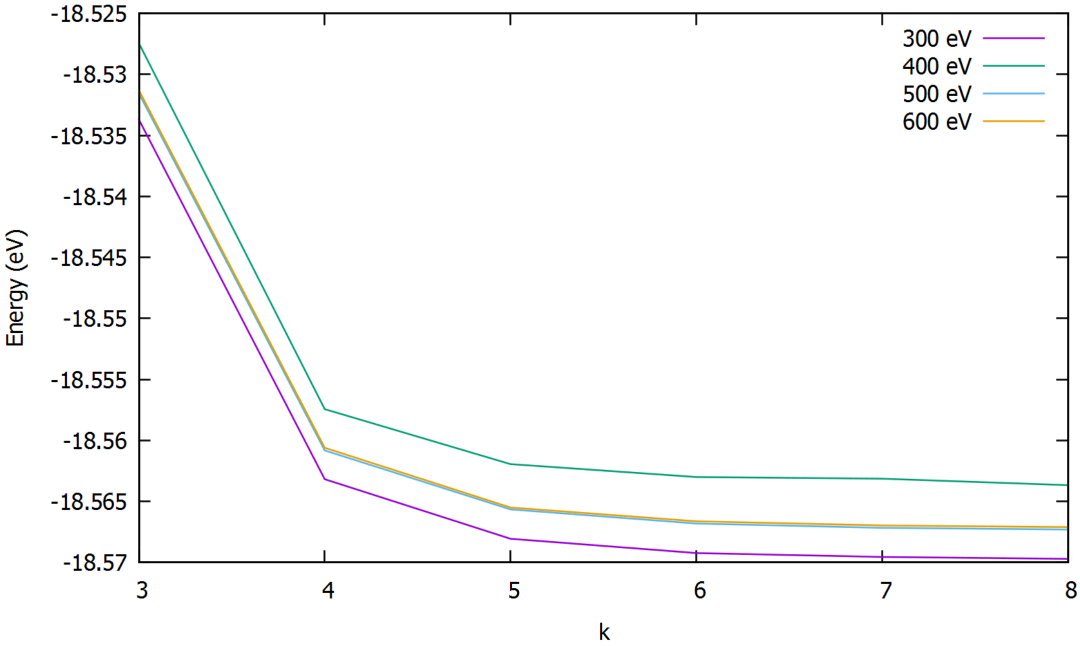

FIGURE 3.1: Plot of free energies against k for various values of energy cutoff. The value of k refers to the cube root of the total number of k-points, as zinc blende is based on a cubic system (e.g. k = 4 indicates a 4 x 4 x 4 k-point grid)

A common threshold for convergence in this type of work is 1 meV. If the value of the free energy changes by less than 1 meV when increasing some parameter, we can say that the system is converged with respect to that parameter. By looking at these results, we can therefore see that the system is converged with respect to number of k-points at a value of k = 6, and with respect to the energy cutoff at a value of 500 eV. These parameters were then used for the next stage of calculations.

3.2 DFT+U

The first method tried was DFT+U. A paper by Aras and Kılıç [47] used DFT+U and the HSE06 hybrid functional to produce accurate values for the band gaps in CdTe and CdSe. They found that a U* parameter of 0.8 provided the best results for CdTe, giving a band gap of 1.48 eV, and a parameter of 3.4 provided the best results for CdSe, giving a band gap of 1.75 eV. VASP allows for separate U* parameters to be assigned to each species within a system, so it was hoped that by choosing different values for U* for both selenium and tellurium, and keeping the U* for cadmium the same in both systems, a single method could be reached that would correctly interpolate between CdTe and CdSe. This was attempted by modelling CdSe and CdTe via the HSE06

Te U* parameter Cd U* parameter	0	3.5	7
0	1.54	1.54	1.54
3.5	1.68	1.68	1.68
7	1.83	1.83	1.83

Table 3.1: Table showing band gaps for different values of U* parameter in CdTe

Se U* parameter Cd U* parameter	0	3.5	7
0	1.52	1.52	1.52
3.5	1.69	1.69	1.69
7	1.87	1.87	1.87

Table 3.2: Table showing band gaps for different values of U* parameter in CdSe

hybrid functional with separate U* parameters on Cd, Te and Se atoms, ranging from 0 to 7, and then examining the calculated band gaps to see if a consistent choice for cadmium's U* parameter could be made while still getting accurate band gaps. Results for this are shown in tables 3.1 and 3.2. For comparison, the experimental band gap for CdTe is 1.5 eV [1], and the experimental band gap for CdSe is 1.7 eV [1].

Disappointingly, while a value of $U^* = 0$ and $U^* = 3.5$ for the cadmium atoms gives good results for CdTe and CdSe respectively, it can be seen that adjusting the U* parameter on the tellurium or selenium atoms has no observable effect on the band gap. Upon examination, it was found that the pseudopotential for cadmium includes terms for d electrons, whereas the pseudopotentials for selenium and tellurium do not. As the DFT+U correction is applied to d electrons, this means that a U* parameter will only have an effect when applied to the cadmium atoms. It is therefore not possible to find a set of parameters that works for CdTe and CdSe simultaneously.

3.3 Dispersion corrections

With the DFT+U approach having failed, the next method tried was to include dispersion forces. DFT fails to accurately predict the London dispersion forces [48], but these can be explicitly modelled by the inclusion of a dispersion correction term. A paper by Szemjonov *et al.* [12] found that dispersion corrections were highly important in predicting correctly the band gap of CdSe. A wider range of hybrid functionals was also explored.

Firstly, single point calculations with several different hybrid functionals were performed on unrelaxed experimental crystal structures to determine which hybrid technique was most appropriate. This was done first as different hybrid functionals can vary considerably in their estimation of band gaps, and given the expense of hybrid calculations, it was determined that it would be more efficient to choose the hybrid functional using only two experimental structures, as opposed to the dozen structures generated by ionic relaxation with dispersion techniques.

After the hybrid functional was chosen, CdTe zinc blende and CdSe wurtzite structures were optimised using standard DFT functionals with dispersion corrections until interatomic forces converged to <0.01 eV/Å. Since it is known that LDA and GGA-type functionals underestimate band gaps in semiconductors, single point calculations of the optimised structures were performed using the selected hybrid functional to calculate electronic properties. Hybrid functionals were not used for structural relaxation, as they have a considerably higher cost than standard GGA functionals, and GGA functionals are already very accurate for structural purposes. The lattice parameters and band gaps were compared to experimental data [1] to find the most accurate choices (see tables 3.3 and 3.4).

3.3.1 Hybrid functional choice

Five hybrid functionals were chosen for electronic calculations: PBE0, HSE03, HSE06, HSEsol, and B3LYP. Additionally, the modified Becke-Johnson (mBJ) meta-GGA was also chosen, as it has been shown to provide good results for calculations of II-VI semiconductors such as CdTe and CdSe [49]. Figure 3.2 and table 3.3 show the calculated band gaps for zinc blende CdTe and wurtzite CdSe for each hybrid functional compared to the experimental band gaps of 1.5 eV [1] and 1.7 eV [1] respectively. HSEsol and HSE03 underestimate the band gaps of both materials, while PBE0 and B3LYP overestimate both band gaps. mBJ provides good results, but a problem exists in the implementation of mBJ within VASP, causing mBJ to behave unpredictably when different parallelisation settings are applied, and thus is discarded. HSE06 overestimates the band gap of CdTe, but underestimates the band gap of CdSe. HSE06 most accurately represents the band gap of CdTe while maintaining similar a band gap difference to all other tested hybrid functionals, and so HSE06 was selected as the hybrid functional to be used going forward.

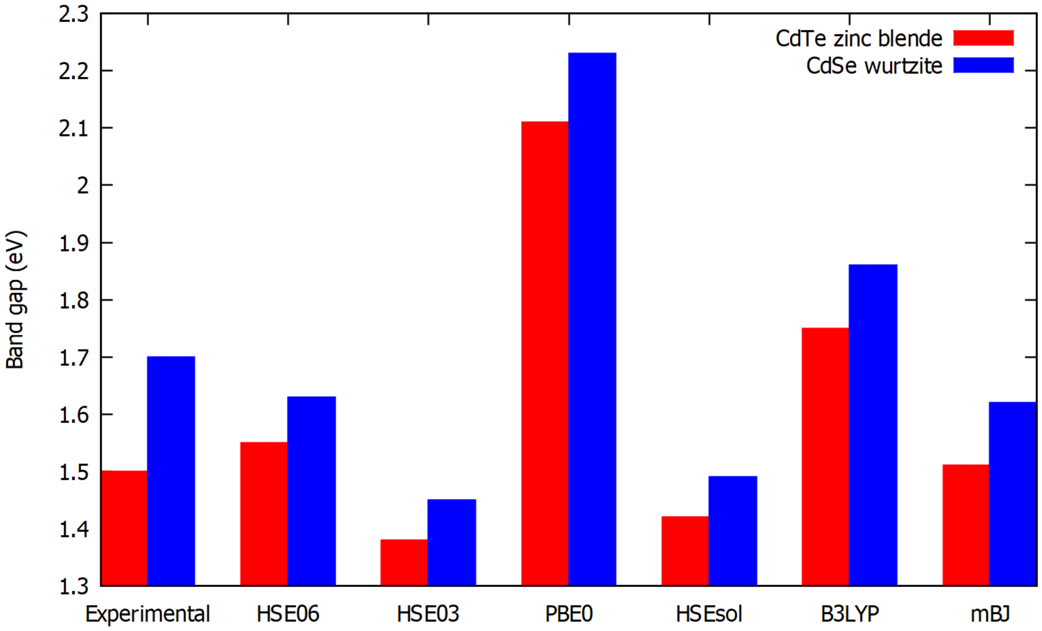

FIGURE 3.2: Plot of band gaps for zinc blende CdTe and wurtzite CdSe for each hybrid method tested. Also shown are experimental band gaps.

Method	Band gap (eV)	
	CdTe zinc blende	CdSe wurtzite
Experimental	1.5	1.7
HSE06	1.55	1.63
HSE03	1.38	1.45
PBE0	2.11	2.23
HSEsol	1.42	1.49
B3LYP	1.75	1.86
mBJ*	1.52	1.61

TABLE 3.3: Band gaps for zinc blende CdTe and wurtzite CdSe for each hybrid method. Also shown are experimentally measured band gaps for CdTe [1] and CdSe [1]. *mBJ data varies depending on parallelisation settings - see appendix.

3.3.2 Structural relaxation functional choice

With the hybrid functional selected, it was next necessary to determine the functional for structural minimisation. Various DFT functionals were chosen for the relaxations: LDA [50], PBE [51], PBEsol [52] and PW91 [53]. Dispersion corrections were also applied to PBE: DFT-D2 [54], DFT-D3 [55], DFT-D3 with Becke-Johnson damping [56], Tkatchenko-Scheffler [57], many-body dispersion energy method [58], and the dDsC dispersion correction [59]. PBEsol with the damped DFT-D3 dispersion method was also used. In order to provide a baseline for comparison, the hybrid results for non-relaxed experimental structures were included. These results are shown in table 3.4 and figure 3.3.

For each functional, an ionic relaxation was performed on both the zinc blende CdTe unit cell and the wurtzite CdSe unit cell followed by a HSE06 self consistent single point calculation to obtain more accurate bandgaps. The calculated band gaps and the percentage deviation of cell volume from experimental values for zinc blende CdTe and wurtzite CdSe are shown in table 3.4 and figure 3.3. The experimental lattices for CdTe and CdSe were calculated with the HSE06 single point method for comparison, labelled "Unrelaxed" in figure 3.3 and table 3.4.

Method	% deviation from experimental cell volume		Hybrid band gap (eV)	
	CdTe	CdSe	CdTe	CdSe
Unrelaxed	0	0	1.55	1.63
LDA	-2.83	-2.58	1.65	1.70
PBE	6.63	6.53	1.35	1.46
PBE+D2	1.52	1.55	1.51	1.60
PBE+D3 damped	1.87	2.37	1.49	1.57
PBE+D3 undamped	2.30	2.29	1.48	1.57
PBE+dDsC	3.43	3.46	1.44	1.54
PBE+TS	1.43	1.99	1.51	1.58
PBE+MBD@rSC	3.69	3.75	1.44	1.53
PBEsol	0.68	0.92	1.53	1.61
PBEsol+D3 damped	-2.99	-2.24	1.65	1.69
PW91	6.32	6.24	1.35	1.47

TABLE 3.4: Deviation from experimental cell volume and hybrid band gaps for zinc blende CdTe and wurtzite CdSe for various relaxation methods within VASP.

The agreement of both band gaps and cell volumes with experimental data is critical to perform accurate simulations. All methods trialled underestimate the difference in band gaps; PW91 and PBE have the largest difference in band gaps but are also the furthest from the experimental cell volume. Introducing dispersion effects into PBE and PBEsol lowers the cell volumes calculated by both functionals. Since PBEsol already accurately models lattice parameters, this addition causes it to considerably underestimate lattice parameters, while PBE, which normally considerably overestimates lattice parameters, now more accurately predicts them. PBEsol and PBE+D2 yield cell volumes within

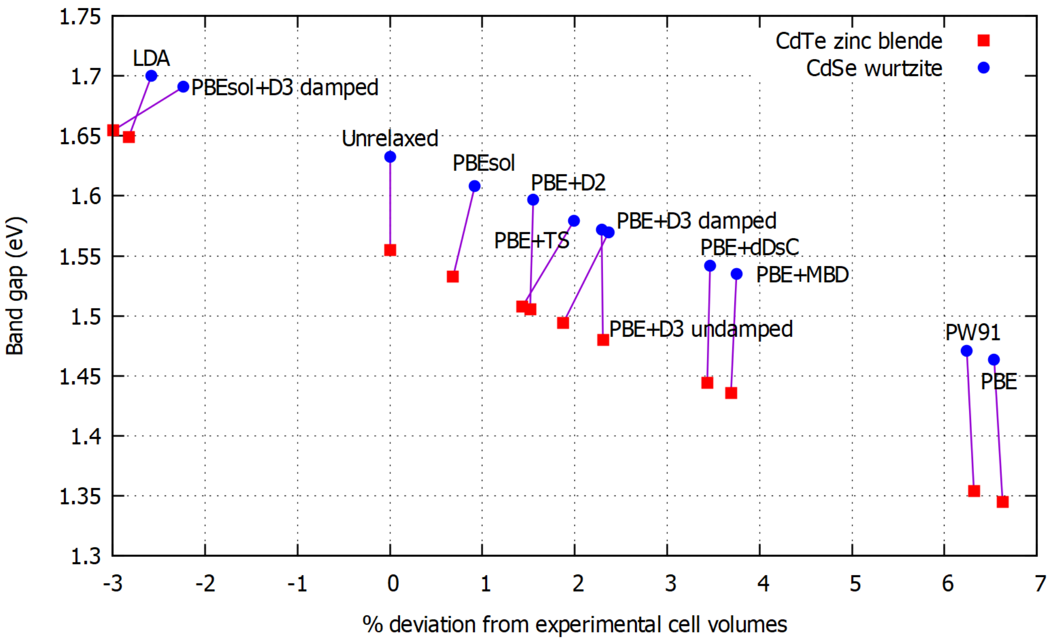

Figure 3.3: (color online) Deviation from experimental cell volume and hybrid band gaps for zinc blende CdTe and wurtzite CdSe is shown for various relaxation methods within VASP, followed by single point HSE06.

2% of experimental values and both show good estimates for the band gap difference compared to the other methods. Both PBEsol and PBE+D2 were therefore selected for further investigation.

PBE+DFT-D2 and PBEsol were then used to study the $\mathrm{CdSe}_x\mathrm{Te}_{1-x}$ system. Supercells of 16 atoms in both zinc blende and wurtzite structures at selenium concentrations of $x = 0$, 0.125, 0.25, 0.375, 0.5, 0.625, 0.75, 0.875 and 1 were simulated to compare the calculated band gap bowing. In order to select the appropriate structures, structural relaxations were performed on all possible arrangements (up to the symmetries of the crystal lattice) of selenium in 16 atom cells. The most stable structure at each concentration was then used to perform a single point hybrid calculation. The increased size of this supercell allows for a reduced k-point grid of 4x4x4 while maintaining convergence. For details on the precise structures used, and the binding energies and band gaps calculated, see the appendix.

It can be seen from the energies calculated that in almost all cases, the most stable zinc blende structure is more stable than the most stable wurtzite structure, although the ranges of energies for the intermediate selenium concentrations overlap with each other. For the CdSe with the PBE+D2 functional, the zinc blende and wurtzite phases have the same energy. The closeness of the energies in these calculations suggests that identifying the whereabouts of the phase transition from zinc blende to wurtzite is beyond the resolution of these functionals in DFT. No structural change was observed between the PBEsol and PBE+DFT-D2 functionals (i.e. the most stable configurations were the same in most cases).

3.4 CdSe$_x$Te$_{1-x}$

3.4.1 Band gap and lattice parameters of CdSe$_x$Te$_{1-x}$

PBEsol and PBE+DFT-D2 method were both used to investigate the full spectrum of CdSe$_x$Te$_{1-x}$ (CST). CST structures were relaxed with these methods to determine the lattice parameters and then an HSE06 single point hybrid calculation was carried out using the most stable relaxed selenium configuration to determine the band gap. The lattice parameter for the cubic zinc blende system, and the a and c parameters for the hexagonal wurtzite system, were calculated using PBEsol, and are plotted against x in figure 3.4, figure 3.5, and figure 3.6. PBEsol was used as it was shown to provide a more accurate value for the lattice parameters. The lattice parameters can be seen to closely follow a linear relationship. This indicates that CST lattice parameters follow Vegard's law, which states that the lattice parameter of a mixture of two solids is a weighted mean of the lattice parameters of the two solids, weighted by their relative abundance in the material [60].

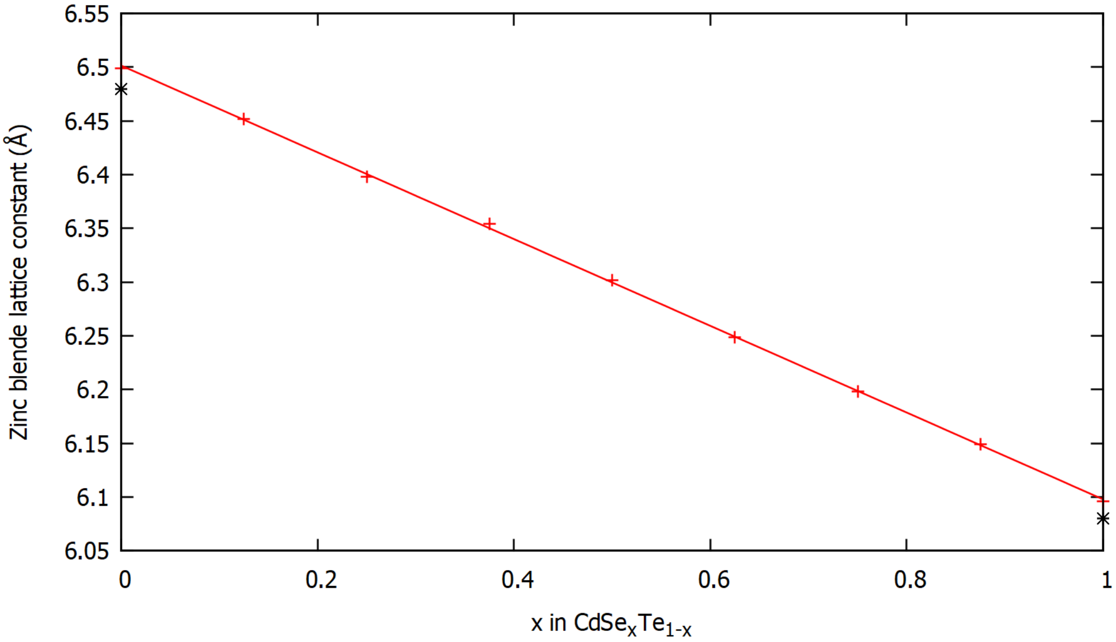

FIGURE 3.4: Plot of zinc blende lattice parameter against x in CdSe$_x$Te$_{1-x}$ for PBEsol, with line of best fit. Experimental lattice parameters are shown in black.

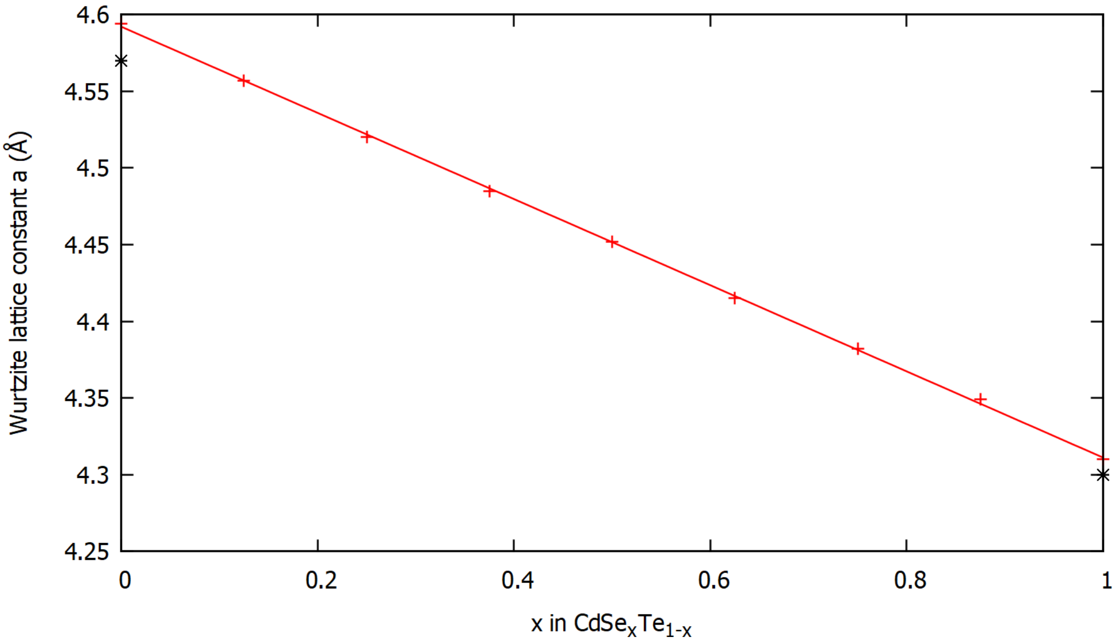

FIGURE 3.5: Plot of wurtzite lattice parameter a against x in CdSe$_x$Te$_{1-x}$ for PBEsol, with line of best fit. Experimental lattice parameters are shown in black.

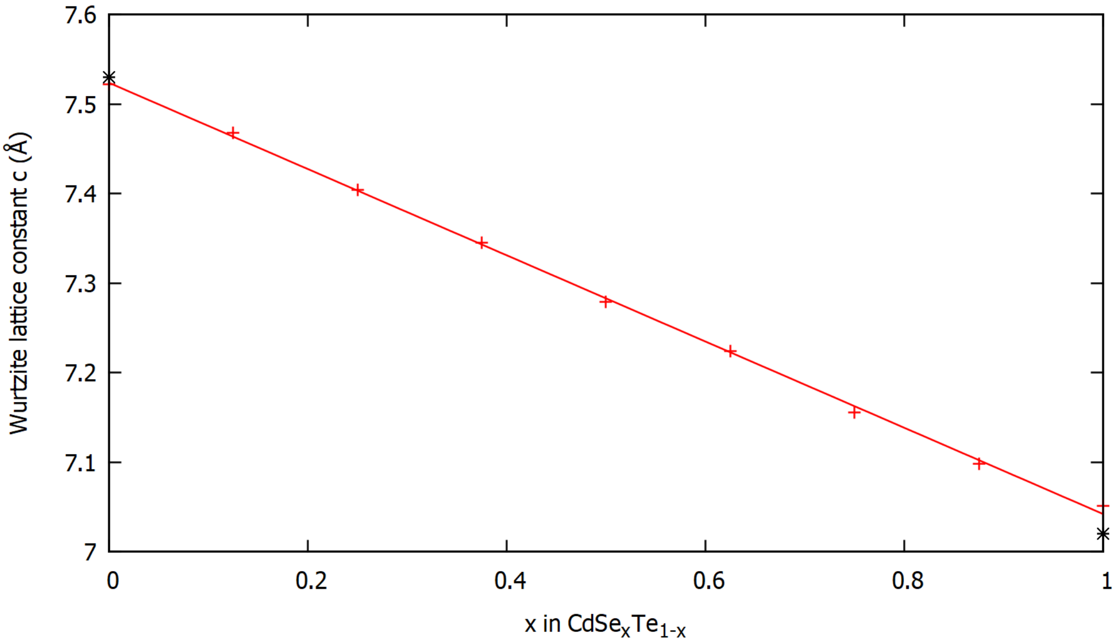

Figure 3.6: Plot of wurtzite lattice parameter c against x in CdSe$_x$Te$_{1-x}$ for PBEsol, with line of best fit. Experimental lattice parameters are shown in black.

For the band gaps, both the zinc blende and wurtzite phases were trialled independently, as shown in figure 3.7. As experiment shows a phase transition occurs in CdSe$_x$Te$_{1-x}$ from zinc blende to wurtzite phases at approximately $x = 0.6$ to 0.7 [6], the results for zinc blende and wurtzite phases are combined by using the zinc blende structures for the $x = 0$, 0.125, 0.25, 0.375, 0.5 and 0.625 concentrations, and the wurtzite structures for $x = 0.75$, 0.875 and 1 in figure 3.8. Experimental data [1] was also included for comparison. Calculated band gaps are also shown in table 3.5.

This procedure involves testing all possible configurations of 16 atom CST cells for each concentration. The most stable structures are those where the selenium atoms prefer to be spread out in the material, as opposed to clustering together. In all the models tested the zinc blende structure was always marginally energetically more favourable than the wurtzite structure although the difference effectively vanished when $x = 1$, highlighting the phase transition in the CST as x increases, in line with experiment [6].

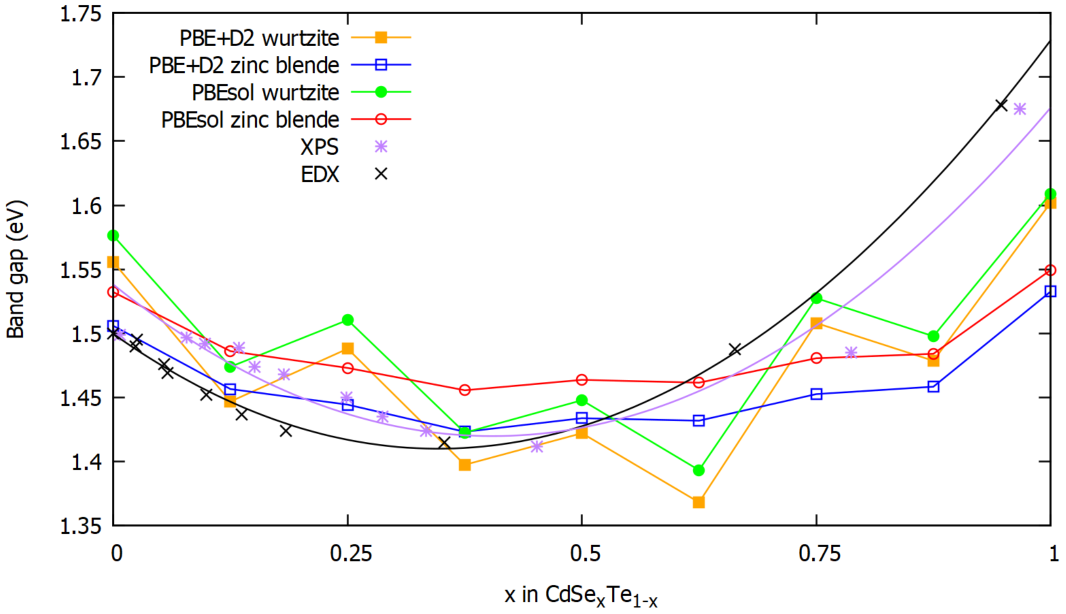

FIGURE 3.7: Plot of band gaps against x in CdSe$_x$Te$_{1-x}$ for PBEsol and PBE+DFT-D2, in both zinc blende and wurtzite phases. Also included are X-ray photoelectron spectroscopy (XPS) and energy dispersive X-ray (EDX) data taken from Swanson *et al.* (2017) [1], with quadratic fits.

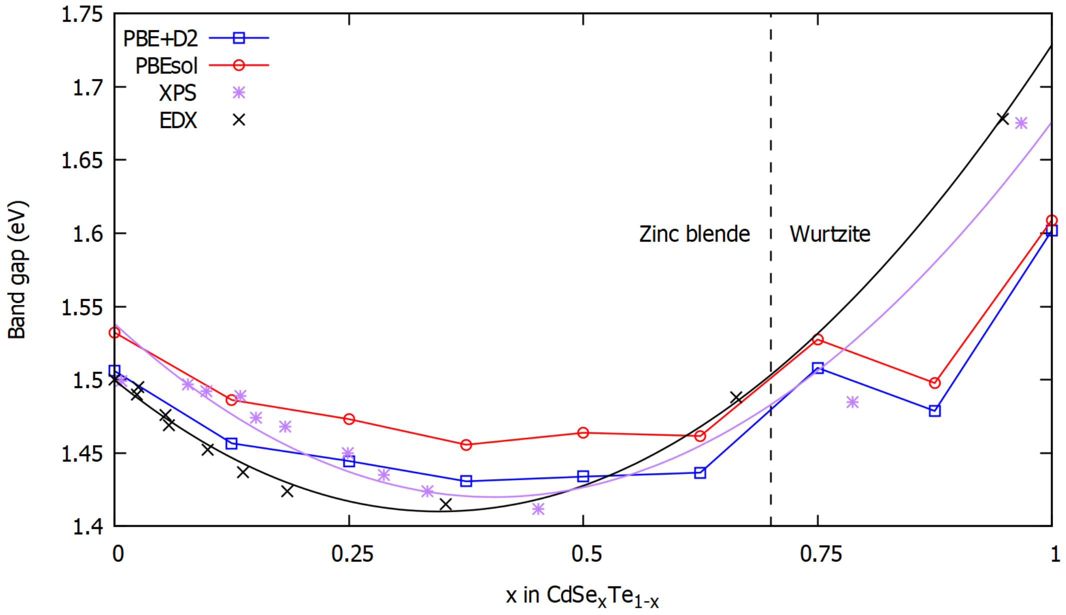

FIGURE 3.8: Plot of band gaps against x in CdSe$_x$Te$_{1-x}$ for PBEsol and PBE+DFT-D2, with zinc blende and wurtzite phases combined. The same experimental data as used in Fig. 3.7 is also shown.

Both functionals underestimate the total bowing and, while both perform well for the CdTe band gap, the CdSe band gap is considerably underestimated. At the $x = 0$

x	PBE+D2 band gap (eV)		PBEsol band gap (eV)	
	Zinc blende	Wurtzite	Zinc blende	Wurtzite
0	1.51	1.56	1.53	1.58
0.125	1.46	1.45	1.49	1.47
0.25	1.44	1.49	1.47	1.51
0.375	1.42	1.40	1.46	1.42
0.5	1.43	1.42	1.46	1.44
0.625	1.43	1.37	1.46	1.39
0.75	1.45	1.51	1.48	1.53
0.875	1.46	1.48	1.48	1.50
1	1.53	1.60	1.55	1.61

Table 3.5: Calculated band gaps of both zinc blende and wurtzite CST for the PBE+D2 + HSE06 and PBEsol + HSE06 methods.

end of the spectrum, the PBE+DFT-D2 functional performs better, as the predicted band gaps lie within the spread of the experimental results, while the PBEsol functional slightly overestimates the band gap at low Se concentrations. For these reasons, the PBE functional with Grimme's DFT-D2 dispersion correction method is deemed to be the most suitable method for the study of CST. By comparing figures 3.7 and 3.8, it can also be seen that combining the wurtzite and zinc blende phases in the aforementioned fashion produces improved fitting of the results than using either phase separately.

3.4.2 Spin-orbit coupling

An important effect to consider when calculating electronic properties with DFT is the effect of spin-orbit coupling. Particularly in materials containing heavy elements such as tellurium, spin-orbit coupling can affect band structures and band edges [61–63]. However, HSE06 already produces an accurate band gap of approximately 1.5 eV for CdTe, and the inclusion of spin-orbit coupling lowers this band gap by approximately 0.3 eV [64]. However, two modifications can be made to HSE06 in order to adjust the band gap to be closer to the experimental values. The first method involves increasing the amount of exact Hartree-Fock exchange included in the hybrid functional from 0.25 to 0.33 [65]. The second method involves reducing the range parameter found in HSE06 to a smaller value, effectively interpolating between the HSE06 and PBE0 hybrid functionals [64].

Although both of these modified methods have been shown to produce accurate band gaps for CdTe while including spin-orbit coupling, their effects on CdSe or the intermediate $\text{CdSe}_x\text{Te}_{1-x}$ system have not been studied. To this end, spin-orbit calculations with adjusted range and exact exchange mixing parameters were performed upon PBE+DFT-D2 relaxed structures. Initially, calculations on the parent structures of CdTe and CdSe were performed in order to optimise the adjusted parameters for the parent structures before studying the mixed system. The optimal parameters were found to be a range parameter of $\mu = 0.09$ Å^{-1} and a Hartree-Fock mixing fraction of $\alpha = 0.33$. These values were then used to calculate band gaps for the mixed CST systems. Results are shown in figure 3.9.

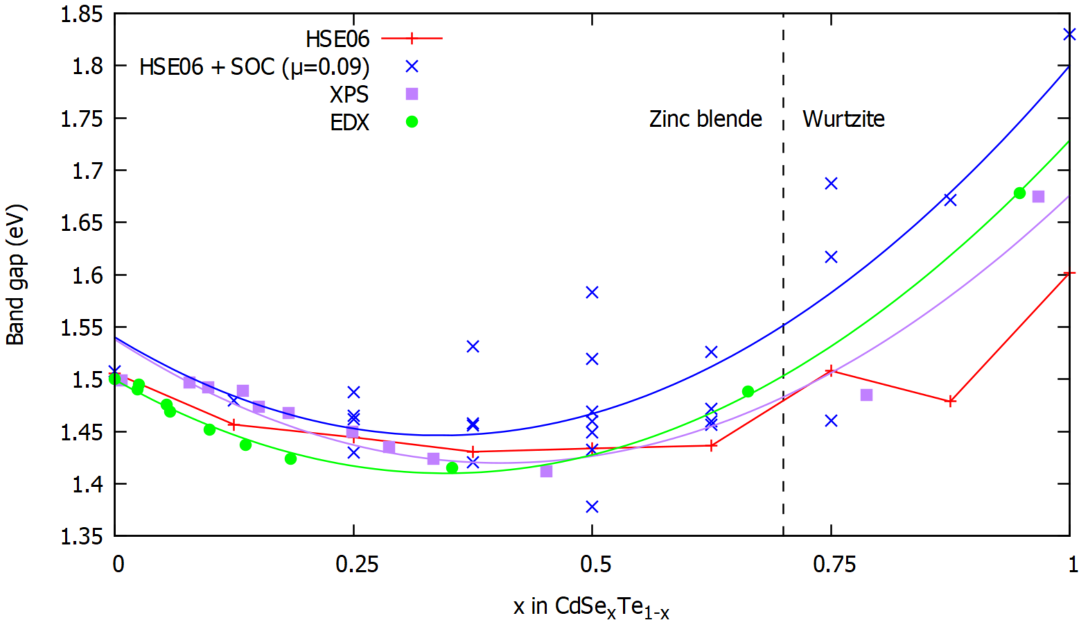

Figure 3.9: Band gaps against x in $\text{CdSe}_x\text{Te}_{1-x}$ for PBE+D2 relaxed structures, with both HSE06 and modified HSE + spin-orbit coupling hybrids. As in figure 3.8, zinc blende structures are used for $x < 0.7$, and wurtzite structures are used for $x > 0.7$.

The results show that while modified HSE + spin-orbit coupling produces reasonably accurate band gaps for the parent structures, it fails to recreate the experimentally observed band gap bowing in the mixed systems. Both modified methods produce an accurate band gap of 1.5 eV for CdTe, while both overestimate the band gap of CdSe by approximately 0.15 eV, in contrast with HSE06, which underestimates CdSe by a similar amount. For the mixed systems, however, it is evident that the spin-orbit coupling results fail to produce a good fit to the experimental results. The bowing observed is too small, and the band gap minimum occurs at $x = 0.25$ compared to the experimental value of approximately $x = 0.4$. For these reasons, spin-orbit calculations are considered to not be a good method for studying $\mathrm{CdSe}_x\mathrm{Te}_{1-x}$. Full results for the bind energy and band gap of each studied structure with spin-orbit coupling may be seen in the tables in the appendix.

3.4.3 Density of states of $\mathrm{CdSe}_x\mathrm{Te}_{1-x}$

3.4.3.1 Density of states

Having established the DFT method to coherently investigate CST systems, we can analyse the density of states (DOS) and hence electronic structure of $\mathrm{CdSe}_x\mathrm{Te}_{1-x}$, where $0 \leq \mathrm{x} \leq 1$. Cathodoluminescence studies of $\mathrm{CdSe}_x\mathrm{Te}_{1-x}$ have shown the presence of a sub-band gap emission peak at very low concentrations of selenium [66]. For this reason, a 64 atom supercell containing a single atom of selenium (giving a concentration of $x = 0.03125$) was studied alongside other concentrations, to determine whether the sub-band gap peak could be identified by the chosen DFT model.

The DOS shown in Figure 3.10 highlights a strong selenium contribution close to the valence band maximum. A clear peak (marked with *) in the density of states can be observed in the conduction band in the 3% composition, and this peak is dominated by selenium contributions. Interestingly, as the selenium concentration increases the selenium peak hybridises much more strongly with the tellurium suggesting a fully saturated valence band. If we partially resolve the selenium density of states, as in figure 3.11 we show that selenium *s* electrons are responsible for the contribution at the valence band maximum with the *p* orbital character dominant in the unoccupied states. Interestingly, if we analyse the equivalent orbital resolved tellurium DOS for the 3% compositions we see both *s* and *p* contributions at the valence band maximum while the unoccupied states are dominated by tellurium and selenium-*p* states at 3% as shown in figure 3.11.

3.5 Conclusion

The best method for the study of $\mathrm{CdSe}_x\mathrm{Te}_{1-x}$ available in VASP is found to be the use of the PBE functional with DFT-D2 dispersion to perform structural relaxations, followed by single point HSE06 hybrid calculations on the relaxed structures to calculate the

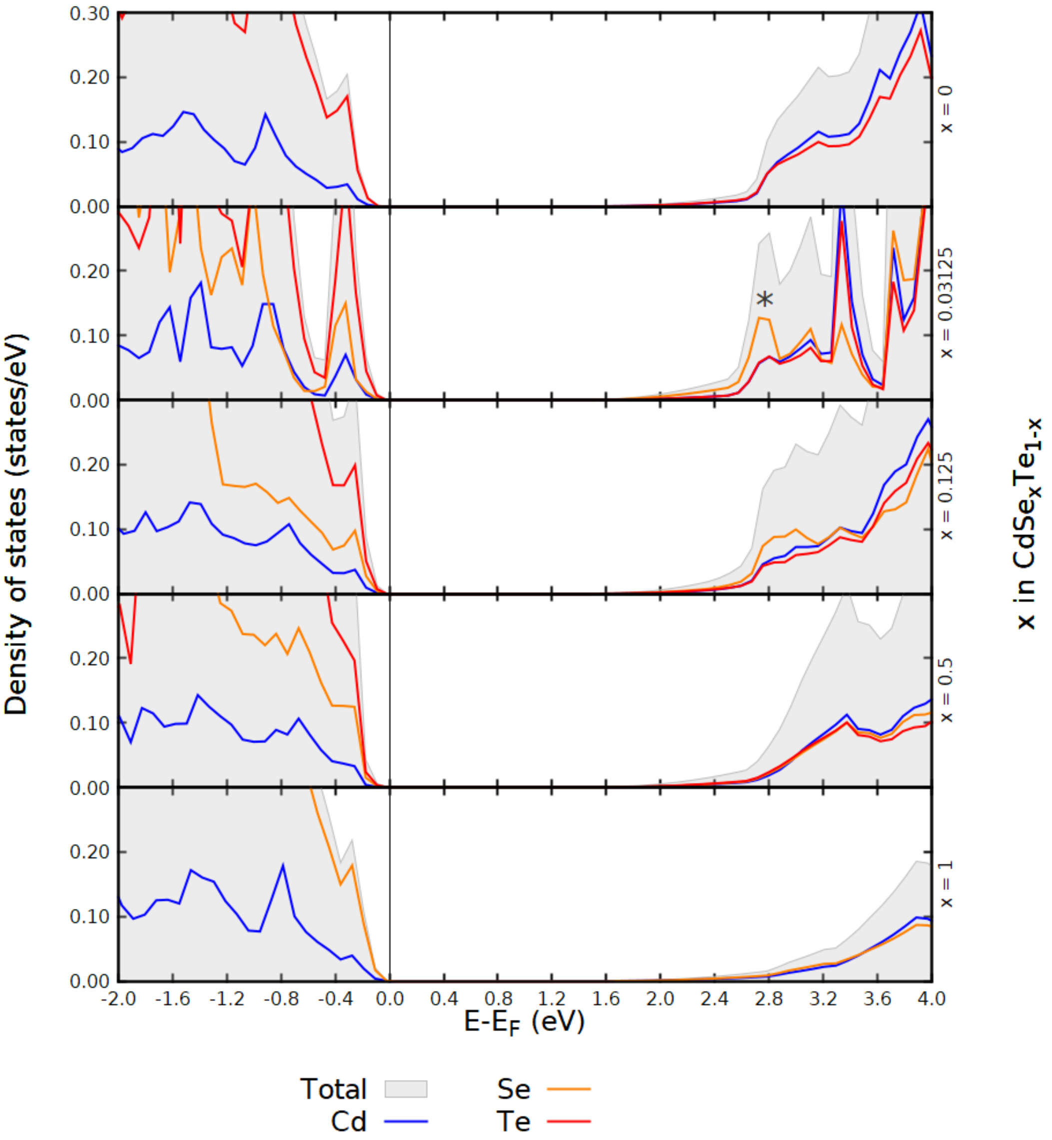

Figure 3.10: (color online) Density of states (DOS) for zinc blende CdSe$_x$Te$_{1-x}$, x = 0, 0.03125, 0.125, 0.5 and 1 showing significant selenium contributions at the valence band maximum and in the conduction band at low selenium concentrations (3-12.5%)

band gaps. This method can now be used to perform detailed analysis of the properties of CST, such as the nature of point defects or grain boundaries, and their effects on band gaps and carrier lifetimes.

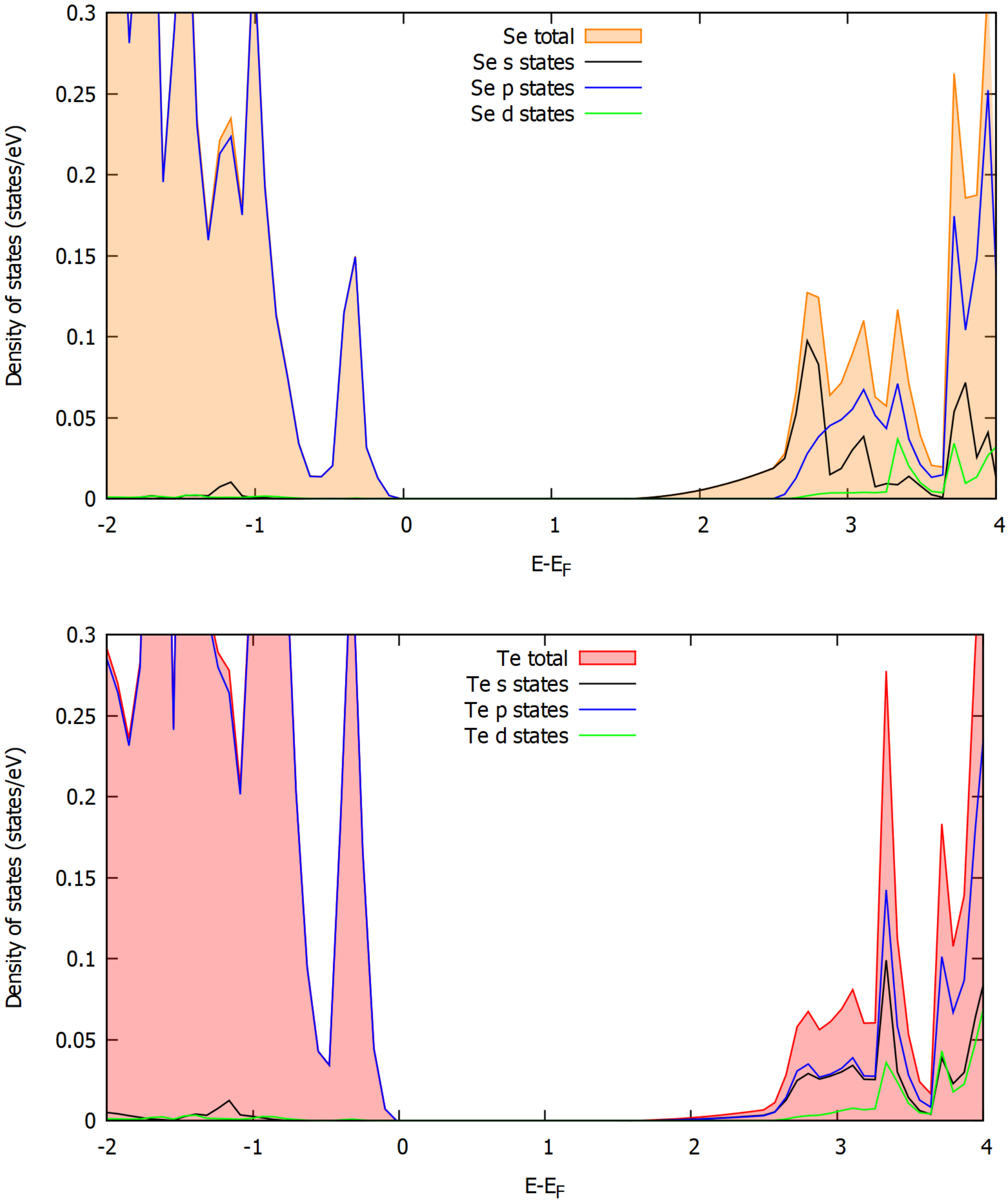

FIGURE 3.11: Computed orbital resolved selenium (top) and tellurium (bottom) DOS for the 3% composition of CST showing the dominant *s* orbital character contributing to the valence band maximum.

Chapter 4

Distribution of selenium in CST

With a suitable functional chosen for the study of $\mathrm{CdSe}_x\mathrm{Te}_{1-x}$, it is possible to study the nature of the selenium alloying itself. Two different methods are chosen for this.

4.1 Cluster expansion and ATAT

One technique for the study of alloy systems is the use of cluster expansions [67]. In these, the energy is parameterised in terms of the possible configurations of atoms on the parent lattice. An occupation variable σ_i is assigned to each site in the lattice, with each possible value corresponding to a particular atomic species, and each possible configuration can be thought of as a vector σ where the entries are the occupation variables of each site. The energy per atom can then be expressed as a polynomial in these variables:

$$(\sigma) = \sum_{\alpha} m_\alpha J_\alpha \left\langle \prod_{i\in\alpha'} \sigma_i \right\rangle \tag{4.1}$$

where α represents a cluster, or set of sites i. The summation is taken over all clusters that are not equivalent by symmetry, while the average is taken over all clusters α' that are equivalent to α by symmetry. m_α is the multiplicity of cluster α, that is, the number of other clusters equivalent to α by symmetry. The J_α then represents the coefficients in this cluster expansions, known as the effective cluster interaction or ECI.

The advantage of this approach is that when the ECI terms are known, the energy of any configuration can be quickly calculated by use of this expression, without requiring any intensive simulations. Finding the ECI, then, is of utmost importance. This can be accomplished by fitting the expression for the energy to the energy of structures calculated with DFT. By calculating the energies of a few dozen structures, the ECI terms can be found to high accuracy, and the cluster expansion can be used to find the energies of many more structures without needing to compute them using DFT.

To this end, the Alloy Theoretical Automated Toolkit [68–72] is employed. This is a collection of codes that interface with a DFT code such as VASP to allow for computation of cluster expansions, generation of special quasi-random structures, Monte Carlo simulations, and more. Special quasi-random structures, or SQS, are structures carefully designed to mimic the most physically relevant radial correlation functions of true random structures. This allows for the generation of structures that capture the essential statistical properties of a much larger number of random structures [73].

ATAT is used to generate special quasi-random structures for calculating the ECI in the cluster expansion. Primitive unit cells are constructed for zinc blende CST, and VASP is used to calculate the energies of progressively larger structures, spanning the spectrum from CdTe to CdSe. 69 structures are generated, and the cluster expansion allows the estimation of the energies of approximately 50000 additional structures. From this, the free energy of each structure is calculated, relative to the energy of the parent structures, which is shown in figure 4.1.

4.1.1 Effect of temperature on free energy

All calculations in VASP are performed at 0 kelvin. However, it is possible to calculate the free energy of mixing at non-zero temperature. The Gibbs free energy G is defined as:

$$G = U + PV - TS \tag{4.2}$$

where U is the internal energy of the system, P and V are the pressure and volume, and T and S are the temperature and entropy. Neglecting the pressure and volume terms,

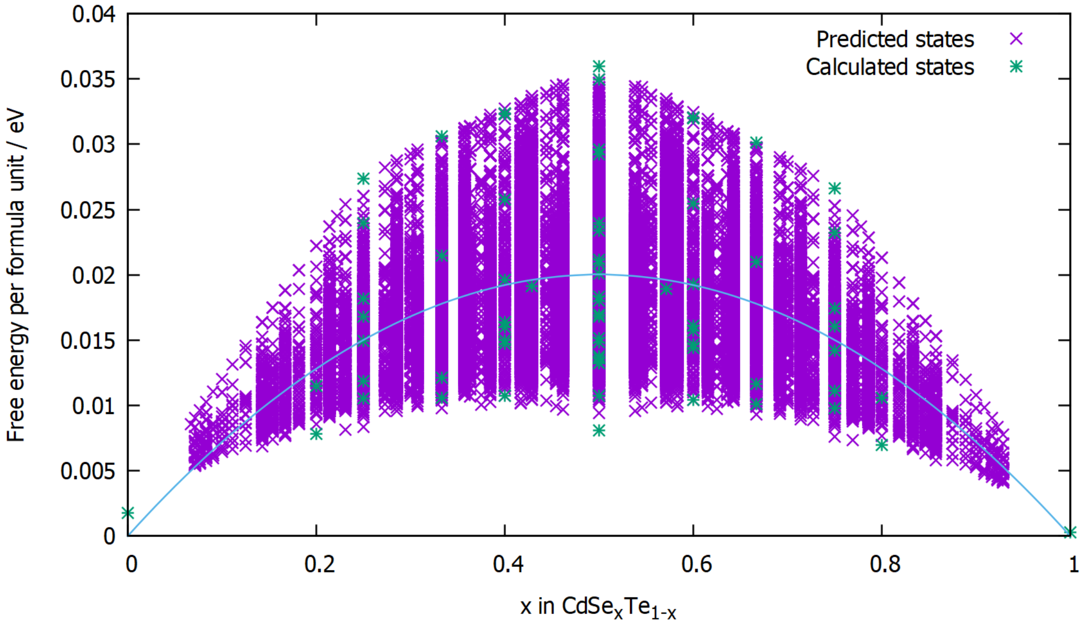

FIGURE 4.1: Graph showing the free energies of approximately 50000 zinc blende CST structures, as calculated by ATAT and VASP. A line of best fit is also shown. Energies shown are relative to the energies of the parent structures.

the entropy term can be calculated explicitly to give the temperature dependence of the free energy.

Entropy is defined as $S = k_B \ln \Omega$ where k_B is the Boltzmann constant and Ω is the number of microstates consistent with the overall macrostate. For a particular concentration x of CdSe$_x$Te$_{1-x}$, with N cadmium atoms, there will be Nx selenium atoms and $N(1-x)$ tellurium atoms. The number of microstates is thus the number of configurations of these atoms, which is $\binom{N}{Nx} = \frac{N!}{Nx!(N-Nx)!}$, and the entropy is $k_B \ln \binom{N}{Nx}$. Applying some algebra gives the following:

$$S = k_B \ln \frac{N!}{Nx!(N-Nx)!} \tag{4.3}$$

$$S = k_B \left(\ln N! - \ln Nx! - \ln N(1-x)!\right) \tag{4.4}$$

Stirling's approximation says that $\ln N! \approx N \ln N - N$. Applying this gives:

$$S = k_B \left(N \ln N - N - Nx \ln Nx + Nx - N(1-x) \ln N(1-x) + N(1-x)\right) \tag{4.5}$$

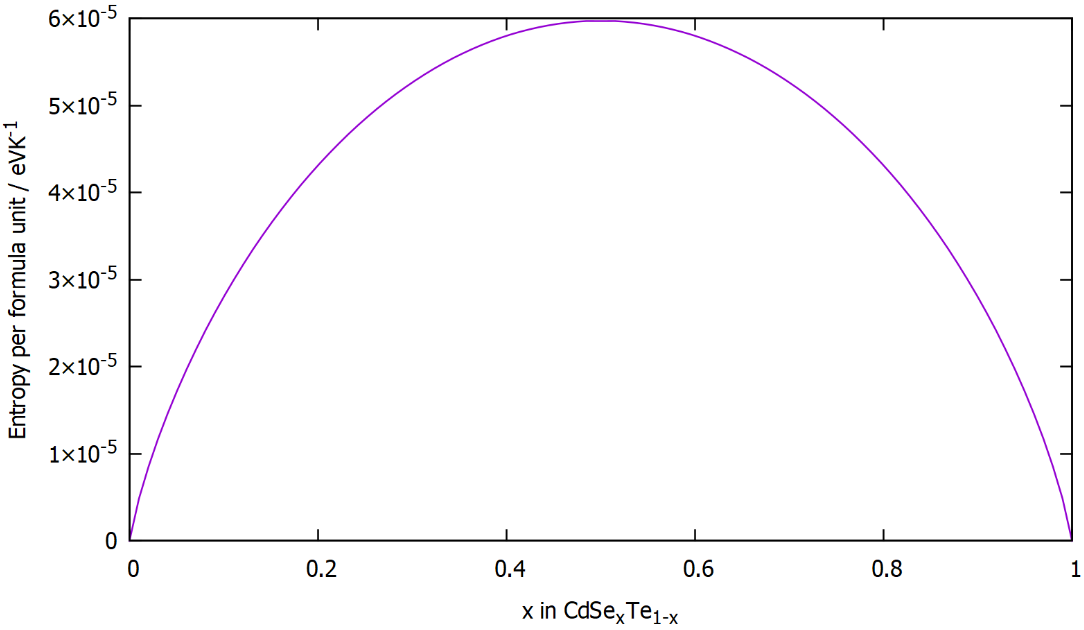

FIGURE 4.2: Graph showing entropy per formula unit of $\mathrm{CdSe}_x\mathrm{Te}_{1-x}$.

$$S = -Nk_B\left(x\ln x + (1-x)\ln(1-x)\right) \tag{4.6}$$

Dividing by N gives the entropy per formula unit as $-k_B\left(x\ln x + (1-x)\ln(1-x)\right)$. This is plotted in figure 4.2.

This allows the calculation of the free energy at temperatures other than 0 kelvin by subtracting this term, multiplied by the temperature, from the line of best fit at 0 kelvin. This is shown in figure 4.3.

It can be seen that this energy is always positive for low temperatures, and as the temperature rises, there are certain concentrations that have a negative free energy. At higher temperatures, all concentrations have negative free energy. This suggests that at low temperatures, it is not energetically favourable for CST to form, as the energy cost of doing so is positive, while at high temperatures, it is favourable. At intermediate temperatures, only certain concentrations of CST may be permitted, and this must be taken into account when considering a concentration to aim for to obtain ideal photovoltaic qualities.

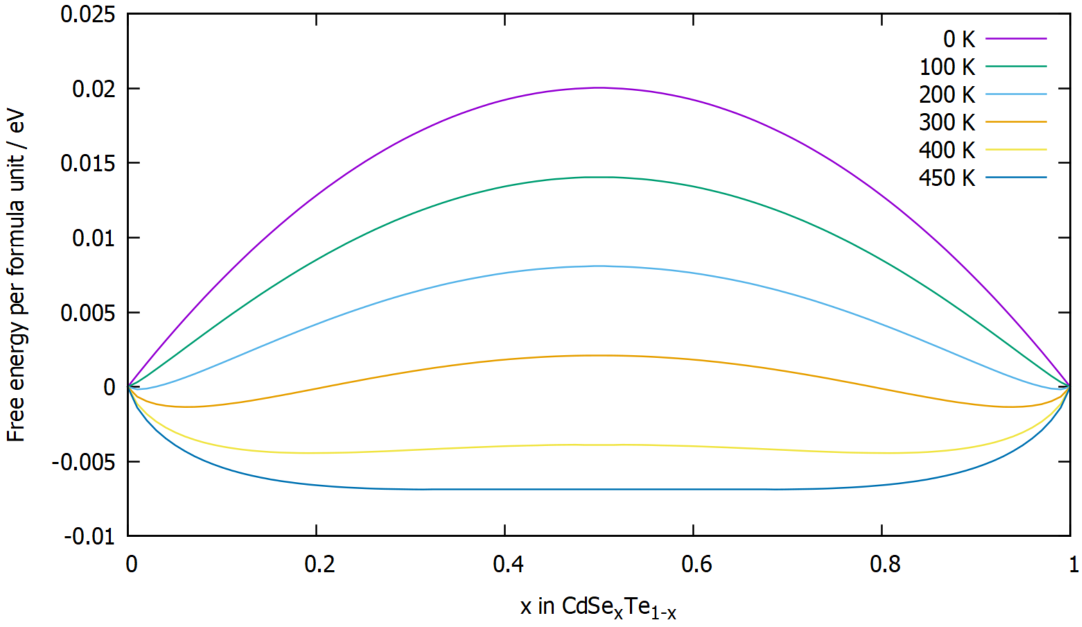

FIGURE 4.3: Graph showing the free energy of mixing per formula unit of $CdSe_xTe_{1-x}$ at non-zero temperatures.

4.2 LAMMPS

LAMMPS, the Large-scale Atomic/Molecular Massively Parallel Simulator [74], is a potential based molecular dynamics code. Though not as accurate as DFT, it is capable of efficiently handling a much larger number of atoms. LAMMPS can be used to study physical or structural properties of a system, such as binding energy or lattice size, but not electronic properties such as band gap. In the case of CST, LAMMPS can be used to investigate the clustering of selenium atoms within the alloy.

The site-occupation disorder code (SOD) [75] can be used to generate all nonequivalent configurations of site substitutions within an arbitrary crystal structure. SOD is used here to generate all 128 atom CST structures with 5 selenium atoms. This results in 5398 different structures. This is far too high to reasonably tackle with VASP, so LAMMPS is used instead. Each structure is minimised using a bond order potential [76], and the binding energy and the selenium-selenium radial distribution functions are calculated.

When calculating a radial distribution function for two particular types of atoms, LAMMPS also calculates a coordination function coord(r), which gives the average number of atoms of the specified type within a distance r of an atom of the other type. As what was calculated in this case was the selenium-selenium radial distribution function, this gives the average number of selenium atoms within a given distance of an arbitrary selenium atom.

For a crystal material, the radial distribution function $g(r)$ will have peaks at specific values of r. These correspond to the nearest-neighbour co-ordination shells, next-nearest-neighbour co-ordination shells, and so on. By plotting the binding energy of each system against the value of $\text{coord}(r)$ at the value of r corresponding to the nearest-neighbour co-ordination shell, a relationship between the binding energy of the system and the clustering of selenium atoms in nearest-neighbour configurations can be established. This is shown in figure 4.5. Each horizontal line on the graph represents all selenium configurations with a particular value for the average number of selenium atoms in nearest neighbour configurations. For example, if the structure contains only one nearest neighbour selenium-selenium pair, then there will be 2 selenium atoms in a nearest neighbour configuration. Since there are 5 selenium atoms in total, the average co-ordination number at the nearest neighbour coordination shell is $2 \div 5$, or 0.4. The highest value generated was 3.2, which corresponds to a tetrahedron of selenium atoms in nearest neighbour configurations, with a 5th selenium atom in nearest neighbour configuration with 2 of the selenium atoms in the tetrahedron (see figure 4.4).

It can be seen that there is a positive correlation between the binding energy and the coordination number at the nearest-neighbour co-ordination shell. This suggests that there is an energy cost associated with selenium atoms being in nearest-neighbour configurations, and thus that the selenium atoms will prefer to spread out throughout the material, rather than cluster together to form regions of CdSe within a CdTe cell.

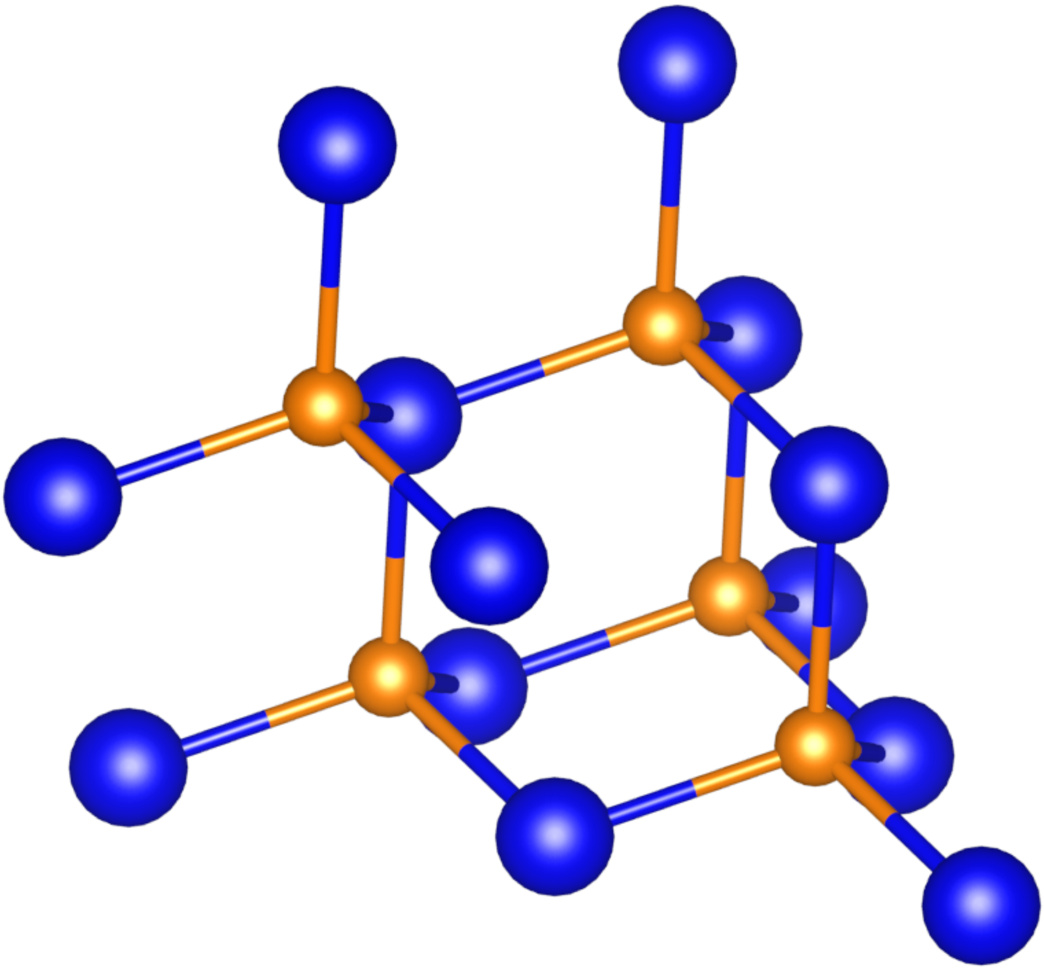

FIGURE 4.4: 5 selenium atoms in the highest clustering configuration. Tellurium atoms and surrounding cadmium atoms have been removed for clarity.

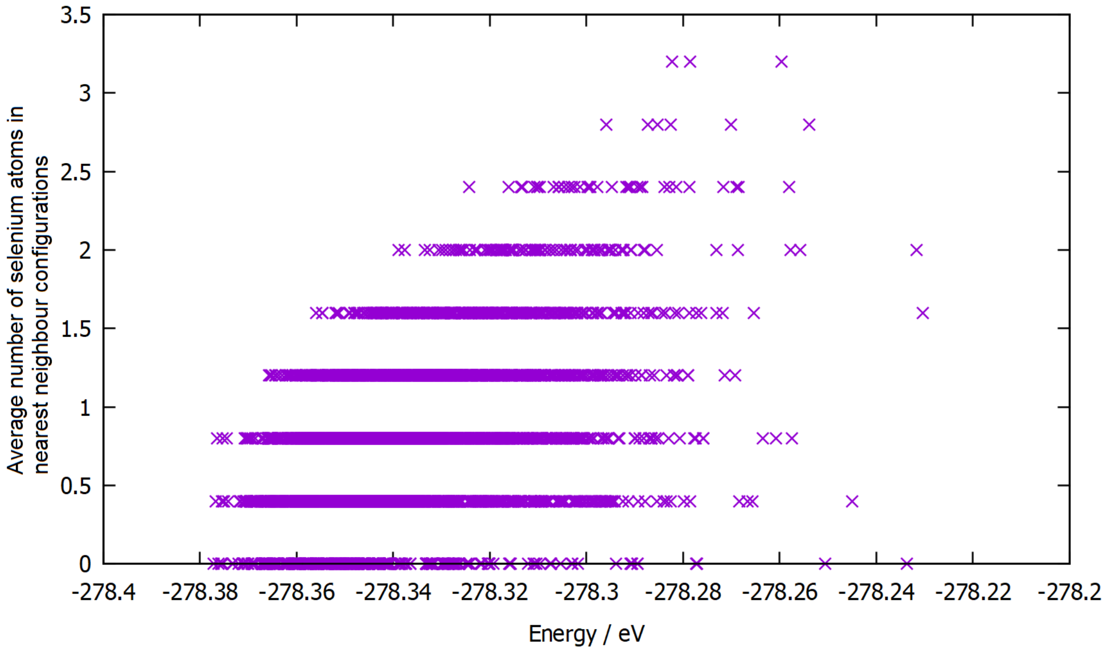

Figure 4.5: Graph showing the relation between the binding energy of CST and the value of the selenium-selenium co-ordination function at the nearest-neighbour co-ordination shell.

Chapter 5

Defects in CdTe

There are several kinds of crystallographic defect that have an important role in determining the electronic properties of a crystalline semiconductor. One kind of important defect is the point defect. There are six kinds of point defects that can be found in CdTe: cadmium and tellurium interstitials $\mathrm{Cd_i}$ and $\mathrm{Te_i}$, cadmium and tellurium vacancies $\mathrm{V_{Cd}}$ and $\mathrm{V_{Te}}$, and cadmium and tellurium anti-sites $\mathrm{Cd_{Te}}$ and $\mathrm{Te_{Cd}}$. Of these, $\mathrm{Cd_{Te}}$ is known to be electrically neutral, $\mathrm{Cd_i}$, $\mathrm{V_{Cd}}$ and $\mathrm{Te_{Cd}}$ are donor states, and $\mathrm{Te_i}$ and $\mathrm{V_{Te}}$ are acceptors [77, 78].

Point defects can act as traps, which capture charge carriers and cause non-radiative recombination to occur [79]. This limits the efficiency of solar cells containing these defects. This process best occurs when the energy of the defect lies in the middle of the band gap, as this maximises the combined capture rate for electrons and holes. However, no point defects in CdTe have such energy. Rather, recombination in CdTe predominantly takes place by way of a two-step process [80]. Firstly, a tellurium anti-site captures an electron near the conduction band. Next, the anti-site relaxes and its structure changes. After this, it lies closer to the valence band, where it can absorb a hole, causing recombination.

With the introduction of selenium into the cell, more types of defects will become available, such as selenium interstitials, selenium vacancies, and selenium anti-sites. Studying the energy of these defects, and their interactions with the existing defects in CdTe will be an important part of this project.

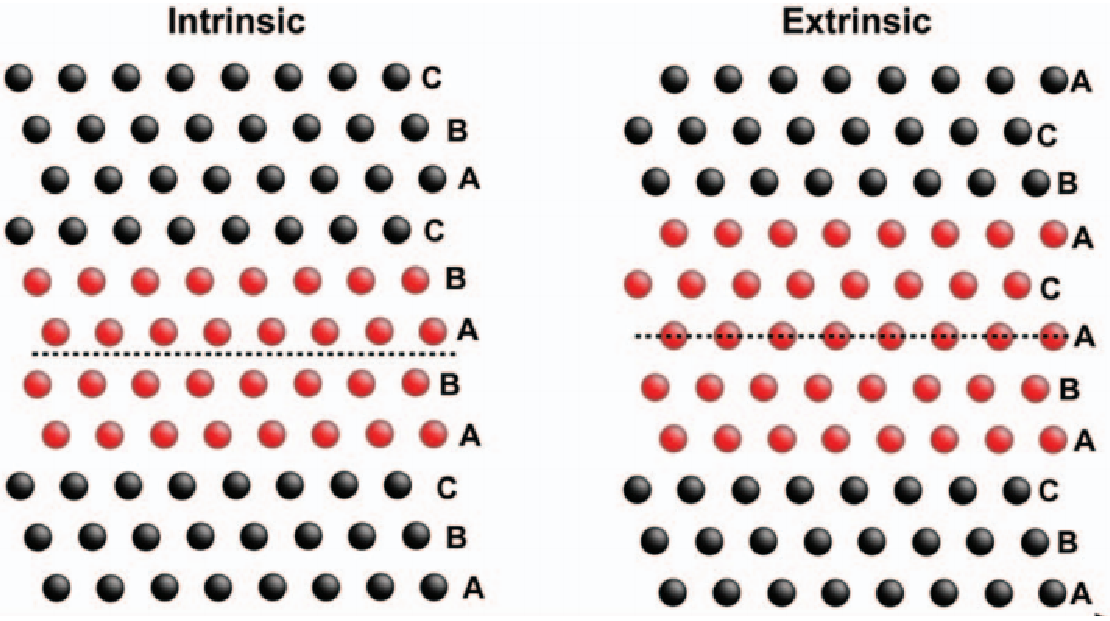

Figure 5.1: Diagram of intrinsic and extrinsic stacking faults. Adapted from [81].

Another important type of defect is the planar defect, which includes stacking faults and grain boundaries. Stacking faults are irregularities in the atomic layering. For instance, a zinc blende structure consists of a repeating structure of 3 layers of atoms, like so: ABCABCABCABC. Stacking faults can be either intrinsic or extrinsic. In an intrinsic stacking fault, a layer is missing, resulting in a structure like $\text{ABC}\underbrace{\text{AB}}_{\text{missing C layer}}\text{ABCABC}$. In an extrinsic stacking fault, an additional layer inserted, like so: $\text{ABC}\underbrace{\text{ABAC}}_{\text{extra A layer}}\text{ABCABC}$. See figure 5.1.

There are also twin stacking faults, which consist of reversals of the layer structure: $\text{ABCAB}\underbrace{\text{CBACBA}}_{\text{Reversed order}}$.

When deposited, CdTe is observed to have a huge number of stacking faults, and has very poor efficiency. After the cadmium chloride treatment, the stacking faults are largely removed, with the exception of some twin faults. Stacking faults, however, are know to be electronically inert, and their presence or absence should not affect the properties of the cell. For this reason, it is believed that the stacking fault removal is merely a side effect of another process that increases the cell efficiency. Currently, this is believed to be passivation of the grain boundary. Grain boundaries are strong recombination centres, and passivating them may cause both the increase in efficiency observed and the removal of the stacking faults.

5.1 Point defects in CdTe

Point defects in semiconductors have an important role in determining the electronic properties of the material. There are six kinds of point defects that can be found in CdTe: cadmium and tellurium interstitials $\mathrm{Cd_i}$ and $\mathrm{Te_i}$, cadmium and tellurium vacancies $\mathrm{V_{Cd}}$ and $\mathrm{V_{Te}}$, and cadmium and tellurium anti-sites $\mathrm{Cd_{Te}}$ and $\mathrm{Te_{Cd}}$. Of these, $\mathrm{Cd_{Te}}$ is known to be electrically neutral, $\mathrm{Cd_i}$, $\mathrm{V_{Cd}}$ and $\mathrm{Te_{Cd}}$ are donor states, and $\mathrm{Te_i}$ and $\mathrm{V_{Te}}$ are acceptors [77, 78].

Point defects can act as traps, which capture charge carriers and cause non-radiative recombination to occur [79]. This limits the efficiency of solar cells containing these defects. This process best occurs when the energy of the defect lies in the middle of the band gap, as this maximises the combined capture rate for electrons and holes. However, no point defects in CdTe have such energy. Rather, recombination in CdTe predominantly takes place by way of a two-step process [80]. Firstly, a charged 2+ tellurium anti-site captures an electron near the conduction band. Next, the anti-site relaxes and its structure changes. After this, it lies closer to the valence band, where it can absorb a hole, causing recombination.

With the introduction of selenium into the cell, more types of defects will become available, such as selenium interstitials, selenium vacancies, and selenium anti-sites. Studying the energy of these defects, and their interactions with the existing defects in CdTe will be an important part of this project.

5.2 Formation energies of defects in CST

The energy of formation E_{form} of a defect in a crystal structure is given by:

$$E_{\mathrm{form}} = E_{\mathrm{defect}} - E_{\mathrm{pure}} + \sum_i n_i \mu_i + qE_{\mathrm{F}} \tag{5.1}$$

where E_{defect} is the energy of the crystal cell containing the defect, E_{pure} is the energy of a cell containing no defects, n_i is the number of atoms of type i removed or added to form the defect (positive for atoms removed, negative for atoms added), μ_i is the chemical potential of an atom of type i, q is the charge of the defect, and E_F is the Fermi energy of the system.

For the chemical potentials μ_i, these can be expressed as:

$$\mu_i = \mu_{i,\mathrm{bulk}} + \Delta\mu_i \tag{5.2}$$

where $\mu_{i,\mathrm{bulk}}$ is the energy of an atom of type i in its bulk form, and $\Delta\mu_i$ is related to the energy of formation of the pure structure of $\mathrm{CdSe}_x\mathrm{Te}_{1-x}$ as follows:

$$E_\mathrm{pure,form} = E_\mathrm{pure}/N - \mu_\mathrm{Cd,bulk} - x\mu_\mathrm{Se,bulk} - (1-x)\mu_\mathrm{Te,bulk} = \Delta\mu_\mathrm{Cd} + x\Delta\mu_\mathrm{Se} + (1-x)\Delta\mu_\mathrm{Te} \tag{5.3}$$

where N is the number of cadmium atoms in the pure CST cell.

Two limits can then be defined for the chemical potentials: the cation-rich limit, and the anion-rich limit. The first limit is defined by $\Delta\mu_\mathrm{Cd} = 0$, and the second is defined by $x\Delta\mu_\mathrm{Se} + (1-x)\Delta\mu_\mathrm{Te} = 0$. For simplicity's sake, we will assume that $\Delta\mu_\mathrm{Se} = \Delta\mu_\mathrm{Te}$.

5.2.1 Defects with LAMMPS and SOD

An important issue with regards to defects in CST is whether the presence of selenium affects the formation energy of defects. If selenium is found to raise the formation energies of defects in CST, then, since defects are implicated in recombination in CdTe [80], this may explain the reduced recombination and heightened carrier lifetimes seen in CST [6]. The cadmium vacancy (V_Cd), tellurium-cadmium antisite (Te_Cd) and selenium-cadmium antisite (Se_Cd) were chosen for analysis. As there are too many configurations of these defects and the CST supercell into which they are embedded, LAMMPS and SOD were used in the same manner as in the previous section. Two supercells generated by SOD were chosen, one with a low degree of selenium clustering, and one with a high degree of clustering, and then the SOD code was used again to generate structures with defects in every possible configuration within these cells. This generates 64 distinct structures for each defect type, for each supercell. This, again, is too many structures to tackle with VASP, so LAMMPS was used to calculate the binding energies of all structures.

For each structure, the number of selenium atoms in nearest-neighbour configurations is calculated, and the formation energy of the defects given by LAMMPS is also calculated. The average formation energy is calculated for all defects with a particular number of selenium neighbours, and this is compared to the number of neighbours. This is shown in tables 5.1 and 5.2. No experimental results for defect formation in $CdSe_xTe_{1-x}$ could be found for comparison.

5.2.1.1 Low clustering

Defect type	Number of selenium neighbours around defect	Average defect formation energy / eV
Cadmium vacancy	0	3.131
	1	3.248
Tellurium-cadmium antisite	0	1.713
	1	1.728
Selenium-cadmium antisite	0	0.929
	1	1.157

Table 5.1: Defect formation energies as calculated by LAMMPS versus number of selenium neighbours in the low clustering configuration

5.2.1.2 High clustering

Defect type	Number of selenium neighbours around defect	Average defect formation energy / eV
Cadmium vacancy	0	3.130
	1	3.237
	2	3.330
Tellurium-cadmium antisite	0	1.753
	1	1.754
	2	1.769
Selenium-cadmium antisite	0	0.968
	1	1.198
	2	1.410

Table 5.2: Defect formation energies as calculated by LAMMPS versus number of selenium neighbours in the high clustering configuration

It can be seen that as the number of selenium neighbours around a defect increases, the defect formation energy typically increases by approximately 0.1 eV per selenium neighbour, does not significantly increase for the tellurium antisite, and increases by approximately 0.2 eV per selenium neighbour for the selenium antisite. This suggests that the presence of selenium within the material inhibits the formation of cadmium vacancies and selenium antisites.

5.2.2 Defects with VASP

However, LAMMPS does not necessarily give the most accurate results for defects. VASP is used to calculate the defect formation energies with higher accuracy, to see if the same trends can be observed. As there are too many structures to study all of them with VASP, the structures with the highest and lowest formation energies according to LAMMPS, for each number of selenium neighbours, for every defect, were chosen and simulated with VASP using the methodology developed in chapter 3. The formation energies were calculated for both cadmium-rich and selenium/tellurium-rich configurations. This is shown in tables 5.3 and 5.4.

5.2.2.1 Low clustering

Defect type	Number of selenium neighbours around defect and formation energy according to LAMMPS	Cadmium-rich formation energy / eV	Anion-rich formation energy / eV
Cadmium vacancy	0, lowest formation energy	1.866	1.352
	0, highest formation energy	1.867	1.353
	1, lowest formation energy	1.963	1.449
	1, highest formation energy	1.960	1.445
Tellurium-cadmium antisite	0, lowest formation energy	3.041	2.011
	0, highest formation energy	2.793	1.764
	1, lowest formation energy	2.299	1.270
	1, highest formation energy	2.303	1.274
Selenium-cadmium antisite	0, lowest formation energy	2.797	1.768
	0, highest formation energy	2.760	1.731
	1, lowest formation energy	2.235	1.206
	1, highest formation energy	2.208	1.179

TABLE 5.3: Defect formation energies as calculated by VASP versus number of selenium neighbours in the low clustering configuration

5.2.2.2 High clustering

Defect type	Number of selenium neighbours around defect and formation energy according to LAMMPS	Cadmium-rich formation energy / eV	Anion-rich formation energy / eV
Cadmium vacancy	0, lowest formation energy	1.884	1.370
	0, highest formation energy	1.816	1.301
	1, lowest formation energy	1.921	1.406
	1, highest formation energy	1.942	1.427
	2, lowest formation energy	2.047	1.532
	2, highest formation energy	2.048	1.533
Tellurium-cadmium antisite	0, lowest formation energy	2.803	1.773
	0, highest formation energy	2.745	1.716
	1, lowest formation energy	2.264	1.234
	1, highest formation energy	2.271	1.241
	2, lowest formation energy	2.255	1.226
	2, highest formation energy	2.300	1.271
Selenium-cadmium antisite	0, lowest formation energy	2.214	1.185
	0, highest formation energy	2.749	1.720
	1, lowest formation energy	2.250	1.221
	1, highest formation energy	2.174	1.145
	2, lowest formation energy	2.311	1.282
	2, highest formation energy	2.290	1.261

TABLE 5.4: Defect formation energies as calculated by VASP versus number of selenium neighbours in the high clustering configuration

It can be seen by comparison between the two tables that although in most cases the energies are similar between the high clustering and low clustering configurations, there are a handful of exceptions, such as the tellurium-cadmium antisite with 0 selenium neighbours. In this case, there is a approximately 0.2 eV difference between the formation energies in the structures identified by LAMMPS as being the least stable defect in each configuration. As each such defect has an identical neighbourhood, this suggest a small influence from next-nearest neighbour atoms or further, that is worth investigating in more depth.

Furthermore, it can be seen that LAMMPS does not provide a good estimate of the relative stability of structures within a particular defect type and number of selenium neighbours. In several cases, the defects identified by LAMMPS as being more stable are predicted by VASP to be less stable, or the difference in VASP is so small as to be within the margin of error of the simulation.

Additionally, the trends shown by LAMMPS concerning defect formation energy as a function of selenium neighbours do not necessarily hold up in VASP, although for some defects, they do. The cadmium vacancy is predicted by LAMMPS to show a approximately 0.1 eV increase in formation energy for each additional selenium atom, and this is replicated in VASP. Although the magnitude of the defect formation energy is different, this trend of a approximately 0.1 eV increase in formation energy per additional selenium neighbour does hold for both LAMMPS and VASP. For the tellurium-cadmium antisite, LAMMPS predicts that there is no significant change in formation energy when selenium neighbours are intoduced, but VASP actually suggests that when a single selenium neighbour is introduced, there is a drop in the defect formation energy by approximately 0.5 eV. This may be due to a change in the symmetry group of the defect, as the introduction of the selenium atom changes the symmetry of the antisite's neighbourhood from $\mathrm{T_d}$ to $\mathrm{C_{3V}}$. For the selenium-cadmium antisite, LAMMPS predicts a approximately 0.2 eV increase in formation energy for each additional selenium neigbour, whereas for VASP, one of the 0 neighbour structures has similar energy to the 1 and 2 neighbour structures, and one is higher by approximately 0.5 eV, perhaps suggesting a similar mechanism to the tellurium-cadmium antisite is at play.

Overall, the results suggest that the introduction of selenium increases the formation energy of cadmium vacancies, and may lower the formation energies of tellurium-cadmium and selenium-cadmium antisites. Further investigation is required to study this in greater detail.

As the tellurium-cadmium and selenium-cadmium antisites both for on cadmium sites within the CST lattice, and both have very similar formation energies, it may be argues that as selenium is introduced, the number of tellurium-cadmium antisites will decrease, as it is equally energetically favourable to replace a tellurium atom on a cadmium site with a selenium atom on the same site. If the tellurium-cadmium antisite is responsible for causing non-radiative recombination in CdTe, as has been suggested [80], and the selenium-cadmium antisite does not cause recombination in the same way, this may explain the reduction in recombination seen when selenium is alloyed with CdTe.

Chapter 6

Conclusion

CdTe is rapidly becoming the cheapest form of solar energy with the advantage of it having a lower carbon footprint than crystalline silicon. Recent developments show that cadmium selenium telluride (CST) can improve cell efficiency and passivate electrically active defects increasing the solar cell efficiency even further through a reduction in the band gap and a significant improvement to carrier lifetimes.

The work carried out in Chapter 3 was a preliminary study of modelling CST through density functional theory (DFT) with the VASP code using the DFT-D2 dispersion correction and PBE functional for structural relaxations and the HSE06 hybrid functional for electronic calculations. Spin-orbit coupling corrections were considered, but were found not to be a good fit for CST. The density of states and band gap bowing of CST were calculated at various concentrations and was found to have a selenium peak in the lower conduction band at low concentrations of selenium. The band gap bowing as a function of Se concentration could be reproduced but there was not 100% agreement with experiment. Work carried out following on from this report has indicated that the use of HSE06 with spin orbit coupling and a 33% Hartree Fock contribution gives excellent agreement with experiment [82]. Further calculations of optical absorption spectra in the same paper suggest a reduced transition probability particularly at higher energies, which confirms experimental predictions that Se passivates the non-radiative recombination centres.

The distribution of selenium within CST was modelled with both LAMMPS and ATAT. LAMMPS showed a positive correlation between the value of the radial distribution function at the first co-ordination shell and the energy of the structure, suggesting that selenium atoms prefer not to be in nearest neighbour configurations with each other. ATAT showed that the free energy of binding for CST is positive at low temperatures, negative and high temperatures, and is positive when selenium concentrations are close to 0 or 1 at intermediate temperatures. This suggests that at these intermediate temperatures, there is an upper limit on the amount of selenium that can be added to a CdTe structure. Extending this work into a more detailed study would help throw light on this phenomenon.

Point defects within CST were modelled with LAMMPS and VASP and show that the formation energy of the cadmium vacancy increases as it acquires selenium nearest neighbours, while the opposite is true for the tellurium-cadmium and selenium-cadmium antisites. Further investigation is required into the effects of next-nearest neighbour selenium atoms and charged or interstitial defects. Since it is expected that Se plays an important role in the passivation of defects in CdTe and that this is a major factor in the increased cell efficiency reported for CST, such a DFT investigation would be an important way to take the work forward.

The work has given hints that modelling can be used as a tool to understand electronic and structural properties of doped CdTe. This suggests that similar modelling studies using other dopants such as arsenic might be used to predict the properties of cells with these dopants allowing the design of cells with even greater efficiency.

Appendix A

Crystal structures

This section details the crystal structures used in evaluating the PBEsol and PBE+D2 functionals. Structures are of the material $CdSe_xTe_{1-x}$, in zinc blende and wurtzite phases, for $x = 0$ (pure CdTe), 12.5%, 25%, 37.5%, 50%, 62.5%, 75%, 87.5%, and 100% (pure CdSe). Cadmium atoms are denoted in blue, tellurium in red, and selenium in orange. In order to select the most stable structures for hybrid calculations it is necessary to perform ionic relaxations on all of these structures. Ionic relaxations are performed with the PBEsol and PBE+D2 exchange-correlation functionals. Shown below are diagrams of the crystal structures used and tables of the lattice energies for each structure after ionic relaxation with each method, and lattice energies and band gaps as calculated with HSE06 and HSE06 + spin-orbit coupling (SOC). Different structures within the same concentration are denoted with a, b, c, etc., but this is an arbitrary labelling, and the specific order chosen does not signify anything.

A.1 Zinc blende structures

1. $x = 0$

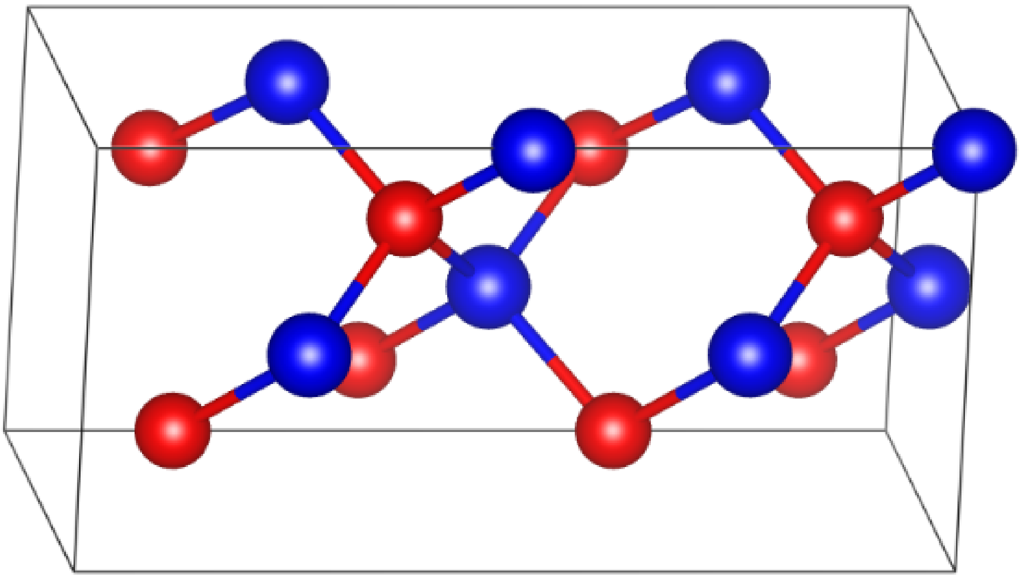

a.

	PBE+D2 energy / eV	PBEsol energy / eV	HSE06 energy / eV	HSE06 band gap / eV	SOC energy / eV	SOC band gap / eV
a	-42.432	-43.920	-48.444	1.5077	-51.831	1.5076

2. $x = 0.125$

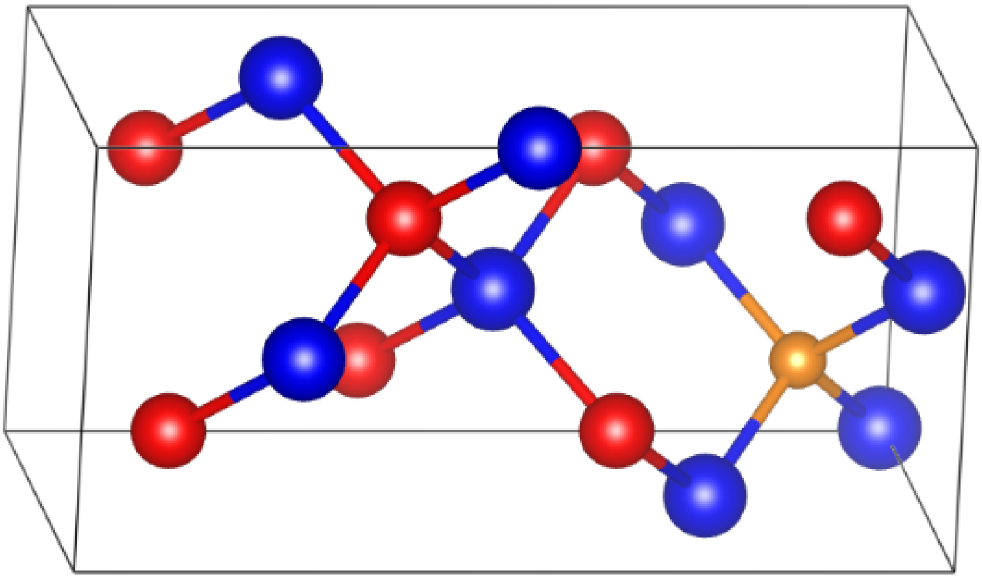

a.

	PBE+D2 energy / eV	PBEsol energy / eV	HSE06 energy / eV	HSE06 band gap / eV	SOC energy / eV	SOC band gap / eV
a	-43.028	-44.537	-49.173	1.4566	-52.495	1.4798

3. $x = 0.25$

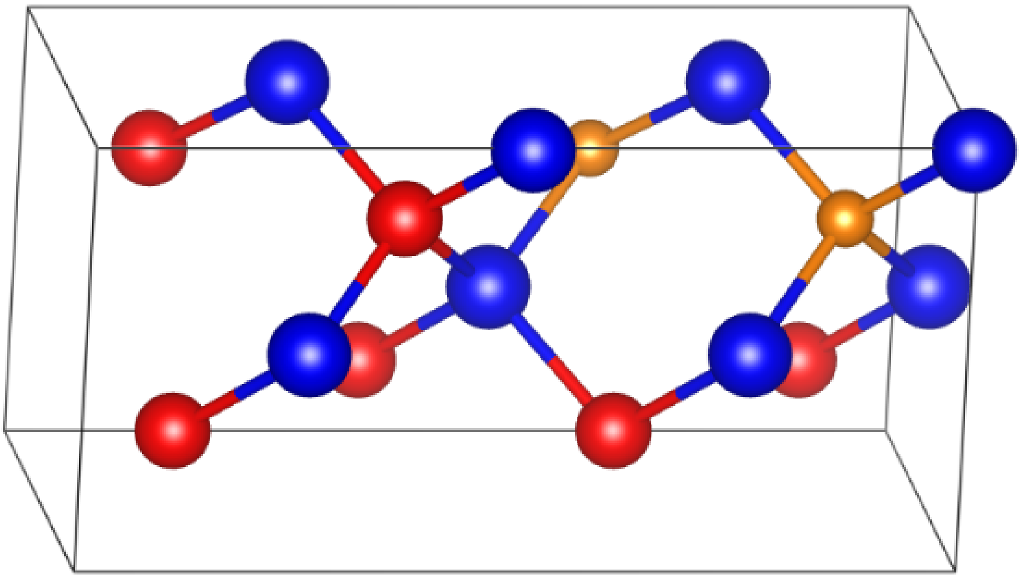

a.

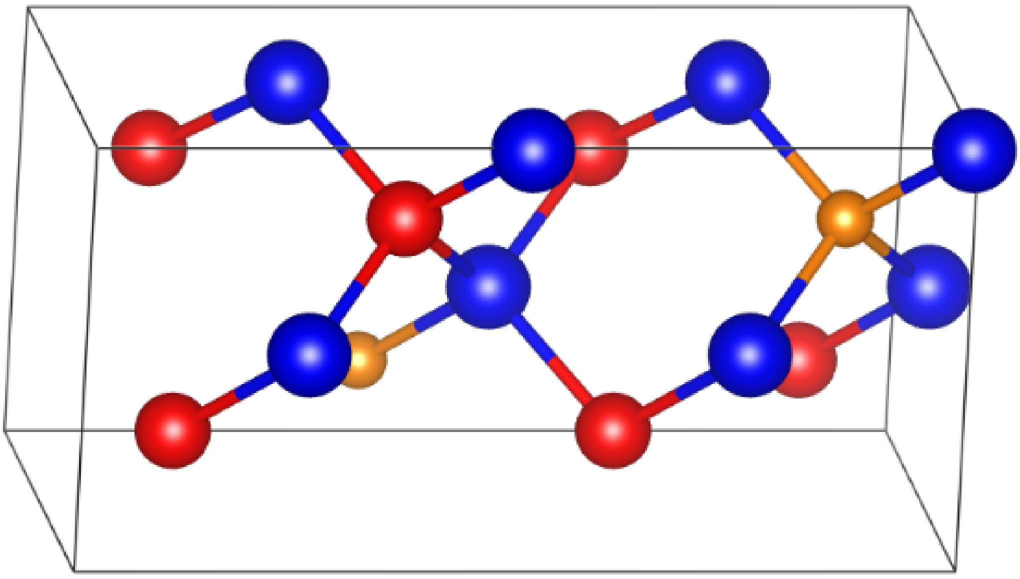

b.

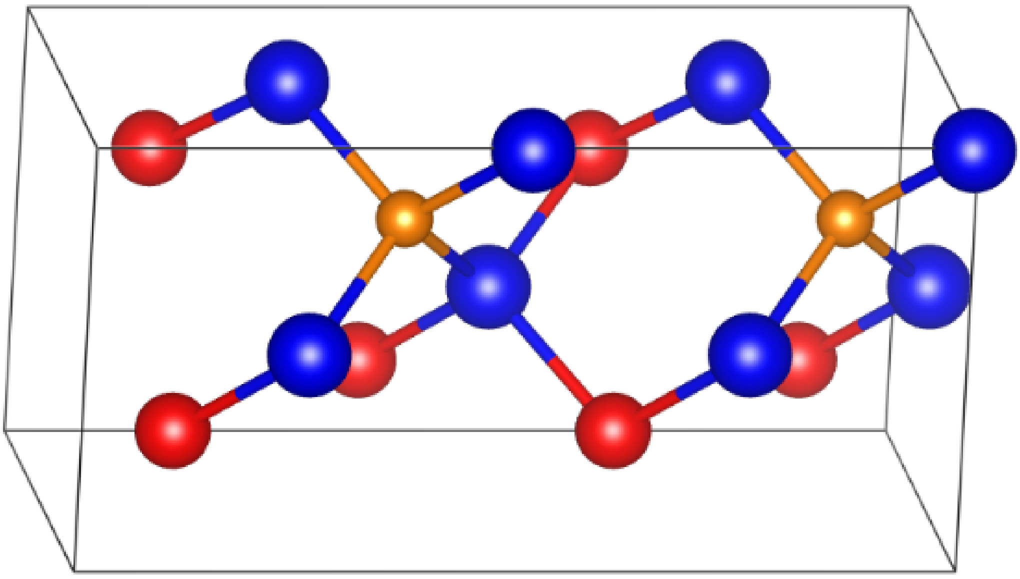

c.

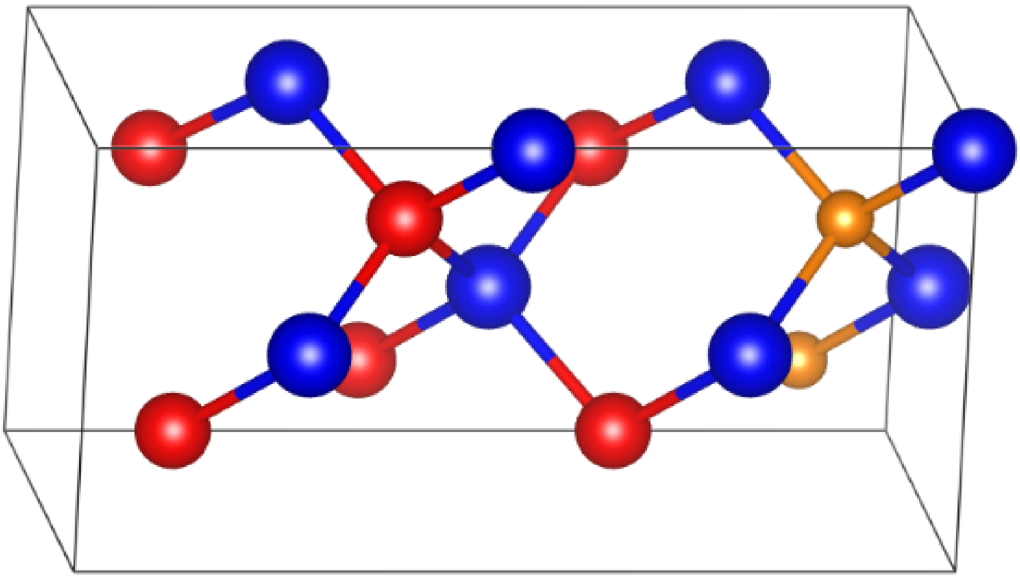

d.

	PBE+D2 energy / eV	PBEsol energy / eV	HSE06 energy / eV	HSE06 band gap / eV	SOC energy / eV	SOC band gap / eV
a	-43.643	-45.176	-49.942	1.4352	-53.184	1.4652
b	-43.663	-45.195	-49.944	1.4445	-53.202	1.4877
c	-43.604	-45.139	-49.907	1.3983	-53.149	1.4296
d	-43.627	-45.160	-49.925	1.4199	-53.166	1.4616

4. $x = 0.375$

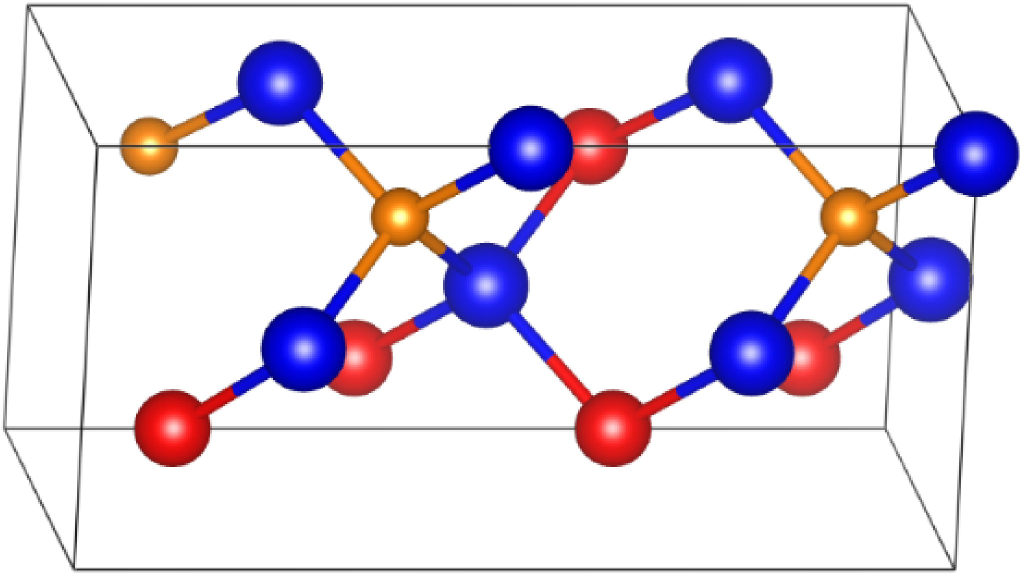

a.

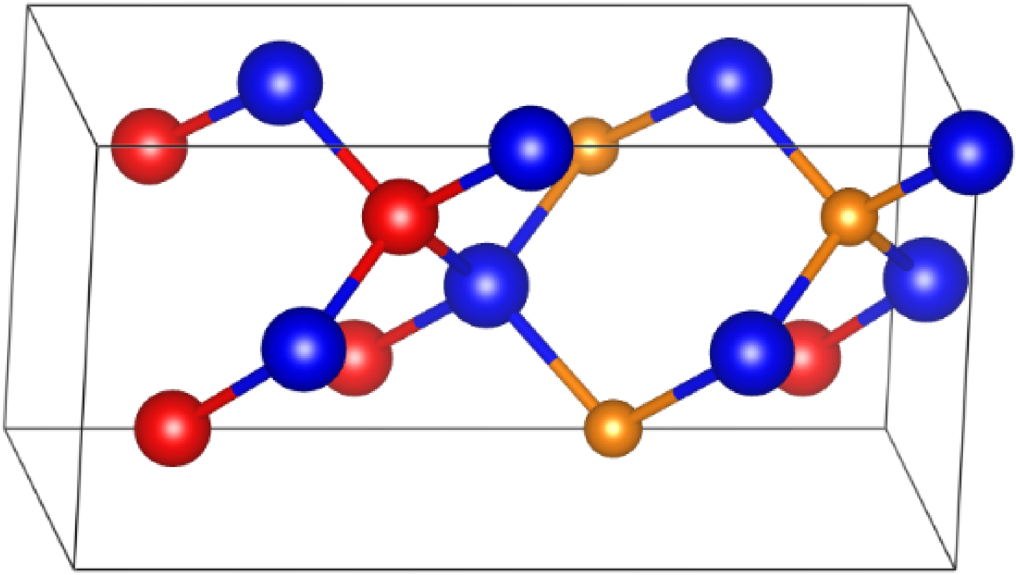

b.

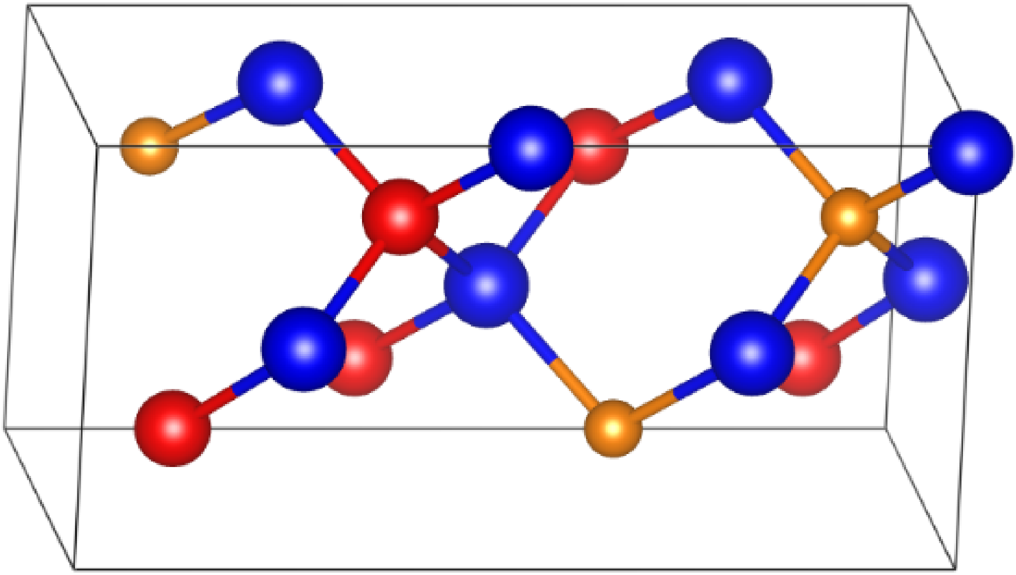

c.

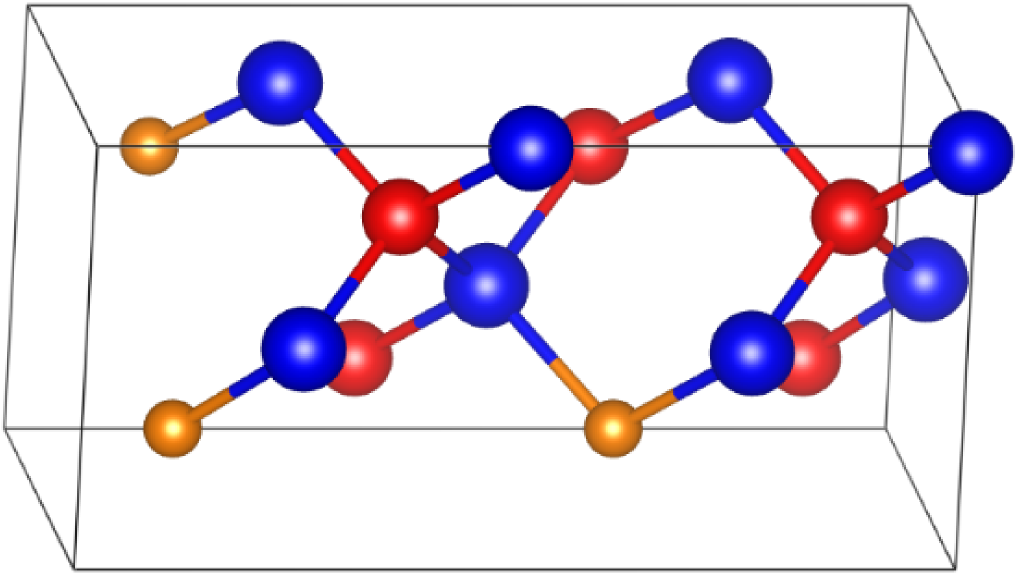

d.

	PBE+D2 energy / eV	PBEsol energy / eV	HSE06 energy / eV	HSE06 band gap / eV	SOC energy / eV	SOC band gap / eV
a	-44.241	-45.802	-50.688	1.3740	-53.864	1.4206
b	-44.266	-45.825	-50.709	1.3994	-53.884	1.4575
c	-44.300	-45.858	-50.725	1.3976	-53.472	1.5312
d	-44.243	-45.804	-50.690	1.3894	-53.865	1.4561

5. $x = 0.5$

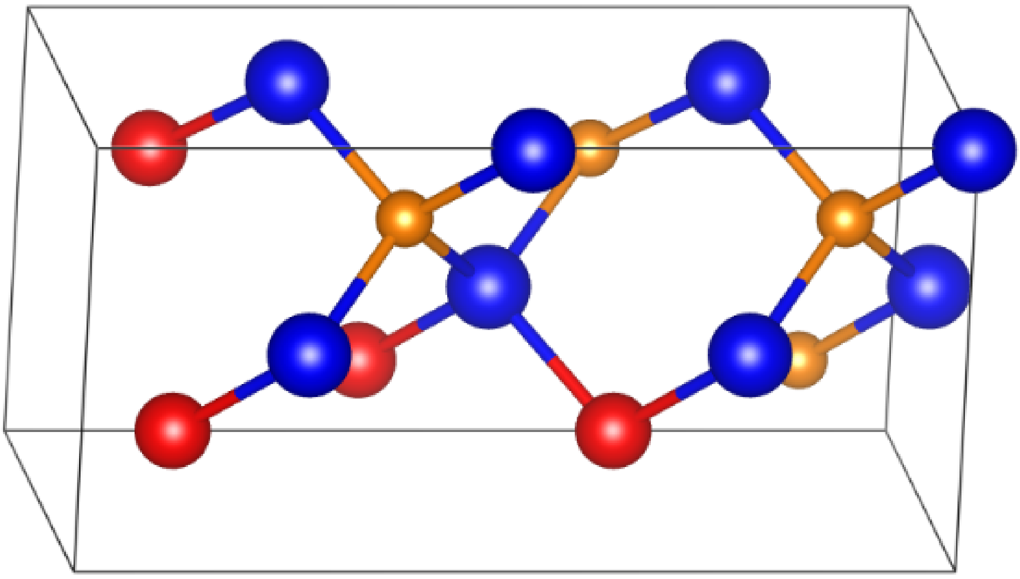

a.

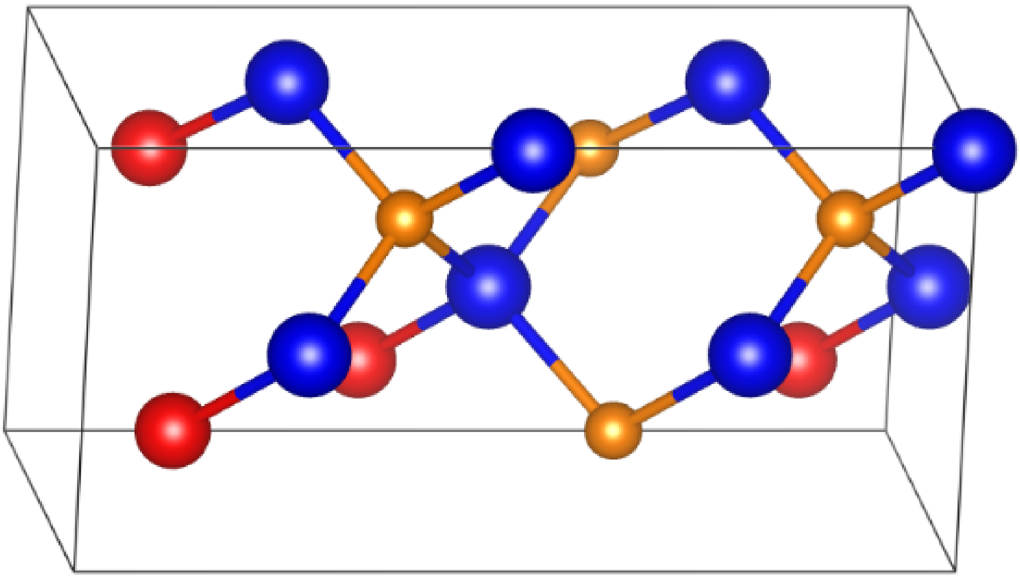

b.

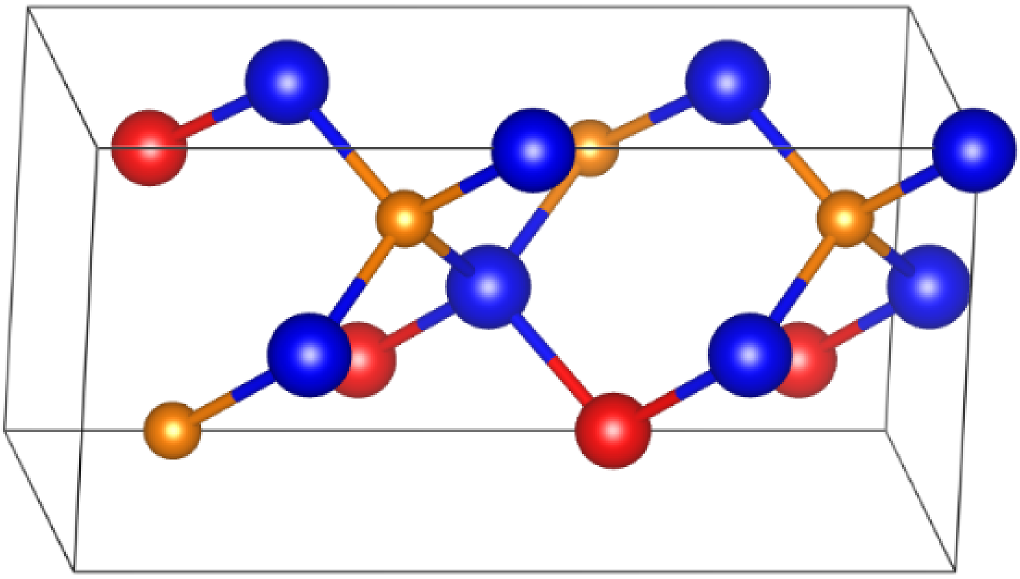

c.

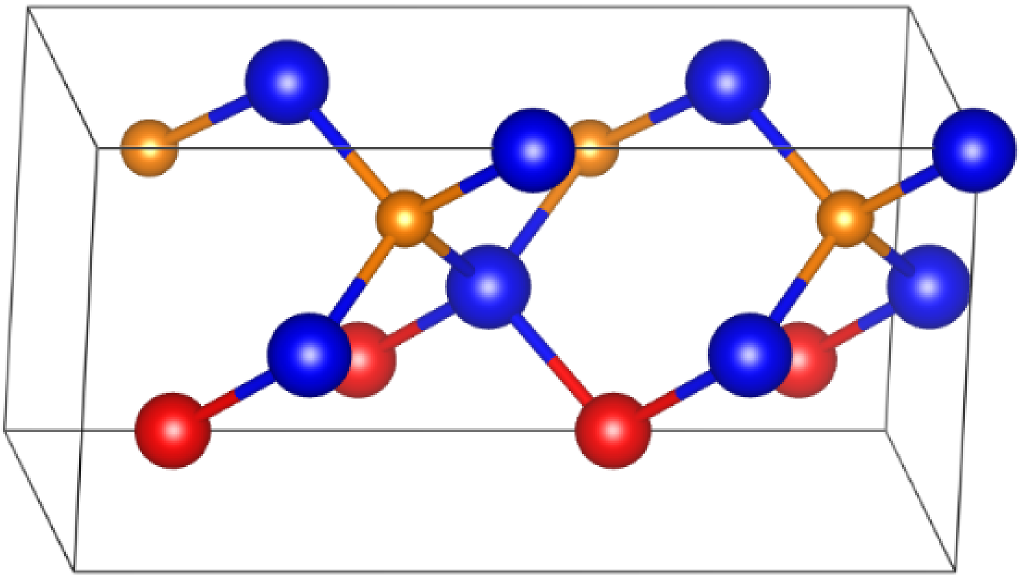

d.

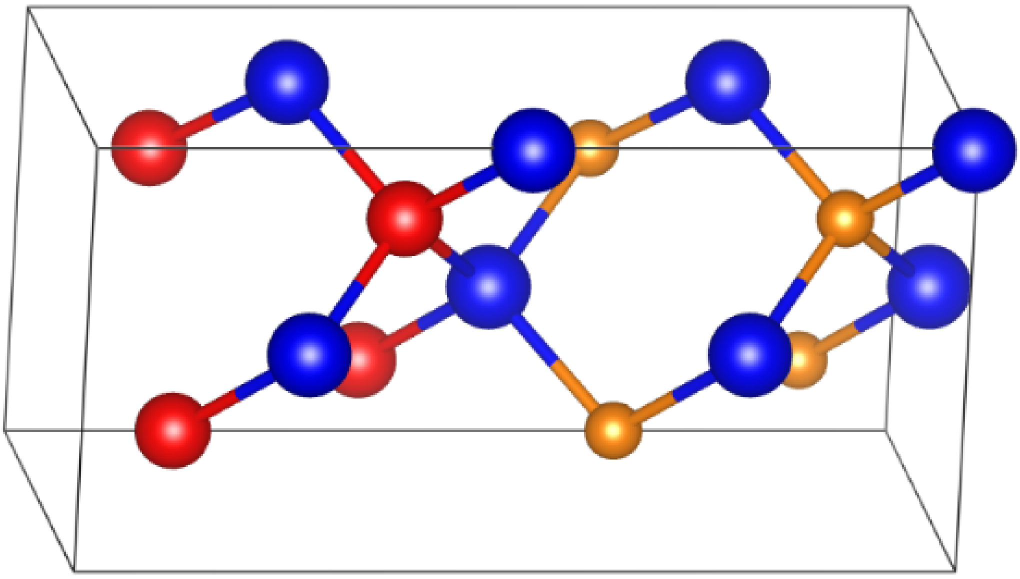

e.

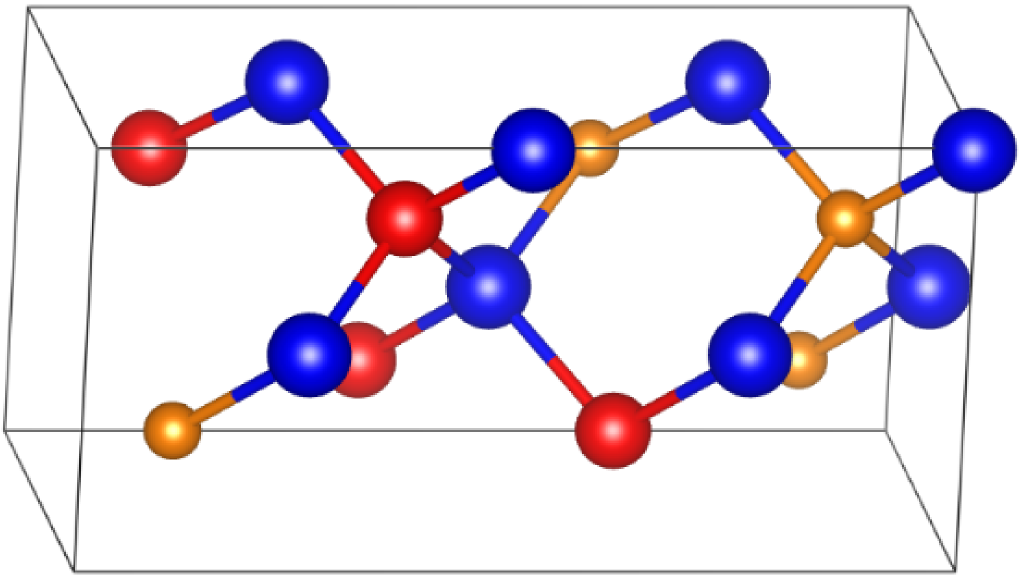

f.

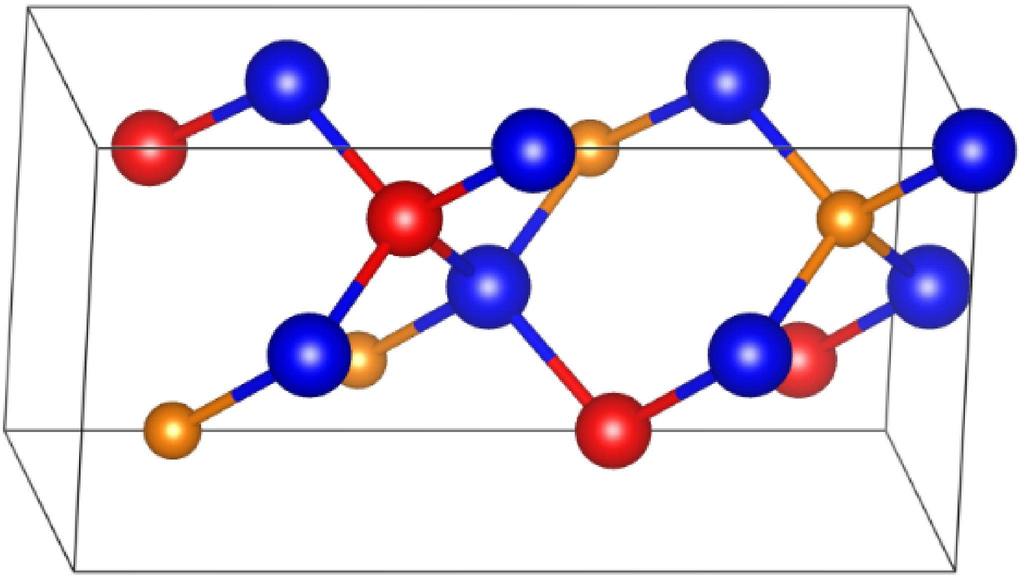

g.

	PBE+D2 energy / eV	PBEsol energy / eV	HSE06 energy / eV	HSE06 band gap / eV	SOC energy / eV	SOC band gap / eV
a	-44.904	-46.494	-51.497	1.3882	-54.607	1.4694
b	-44.888	-46.479	-51.485	1.3706	-54.595	1.4494
c	-44.920	-46.510	-51.512	1.3770	-54.623	1.4600
d	-44.861	-46.455	-51.460	1.3159	-54.570	1.3783
e	-44.915	-46.503	-51.507	1.3677	-54.616	1.4323
f	-44.948	-46.534	-51.537	1.4407	-54.647	1.5193
g	-44.978	-46.564	-51.547	1.4339	-54.753	1.5830

6. $x = 0.625$

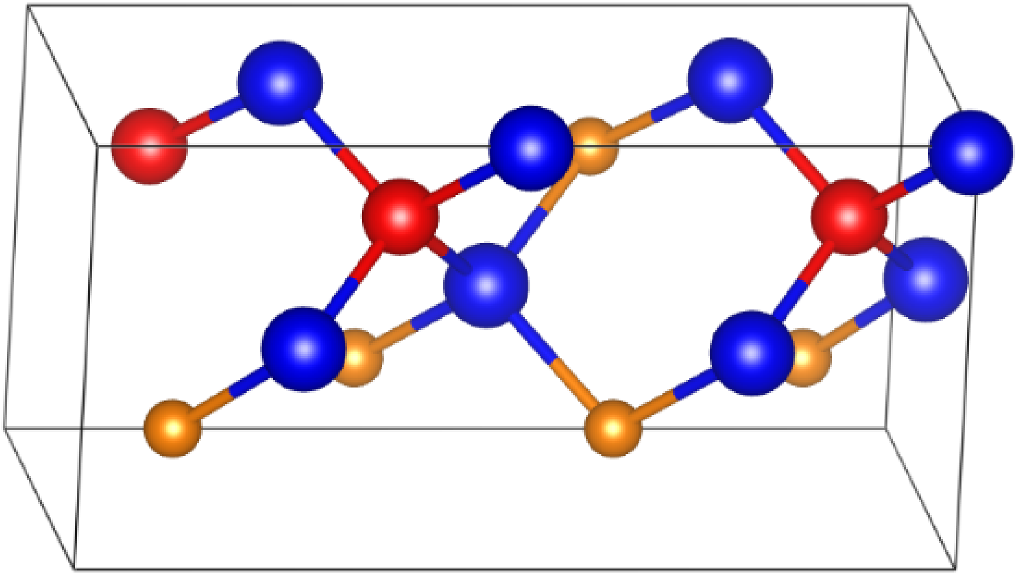

a.

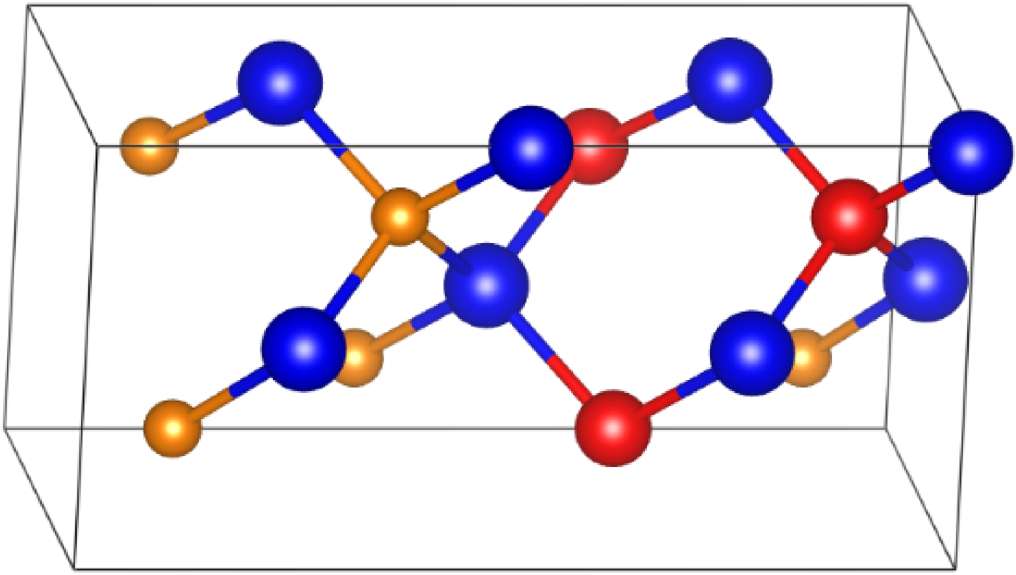

b.

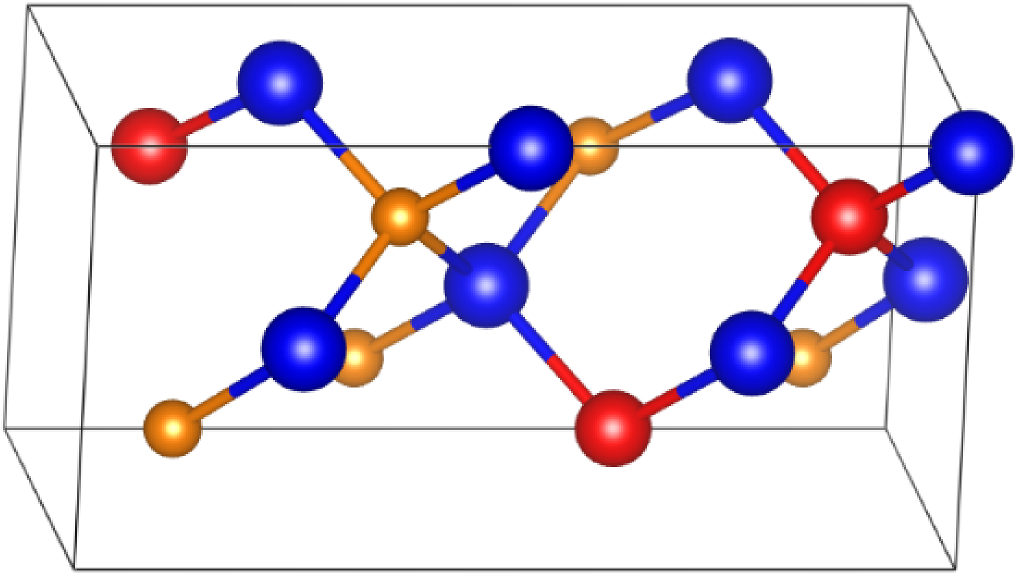

c.

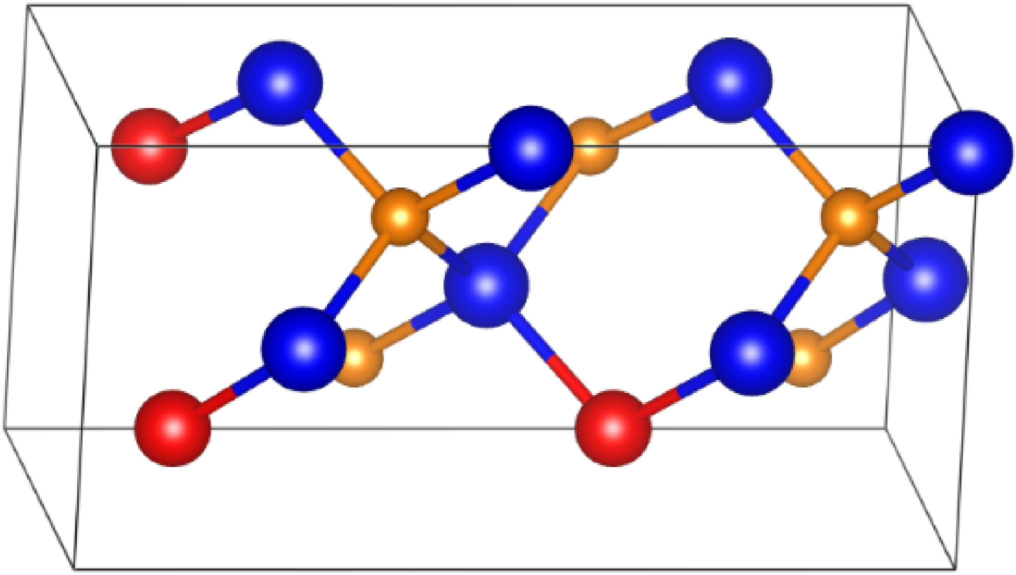

d.

	PBE+D2 energy / eV	PBEsol energy / eV	HSE06 energy / eV	HSE06 band gap / eV	SOC energy / eV	SOC band gap / eV
a	-45.549	-47.173	-52.313	1.3735	-55.357	1.4563
b	-45.577	-47.199	-52.338	1.3829	-55.382	1.4719
c	-45.607	-47.228	-51.223	1.4249	-54.245	1.5262
d	-45.546	-47.171	-52.313	1.3625	-55.356	1.4599

7. $x = 0.75$

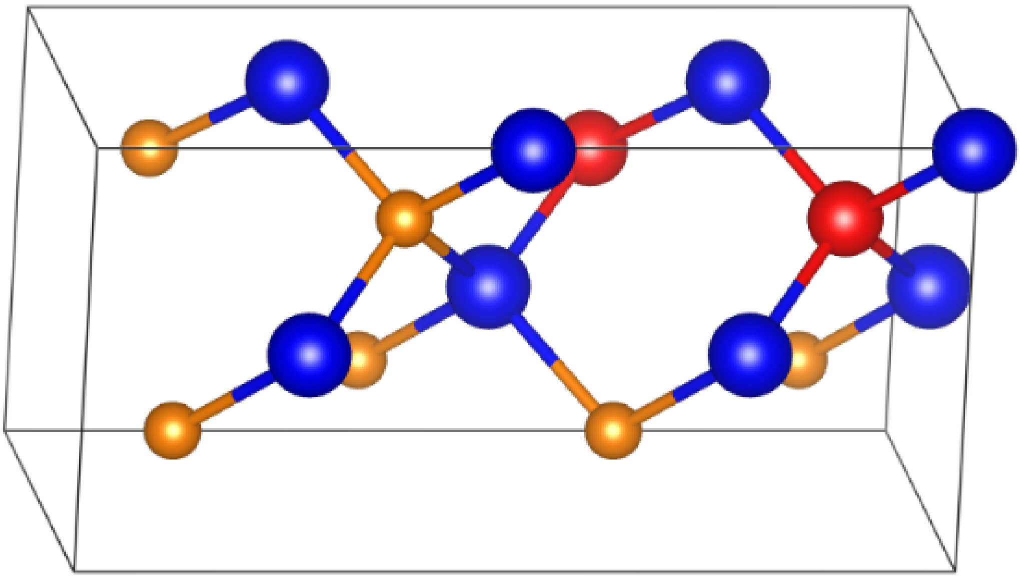

a.

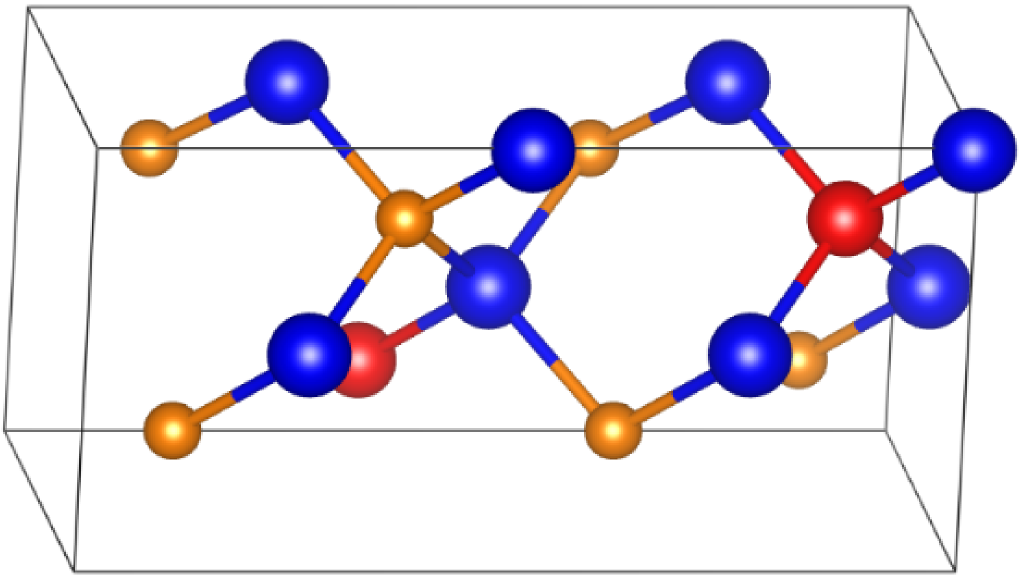

b.

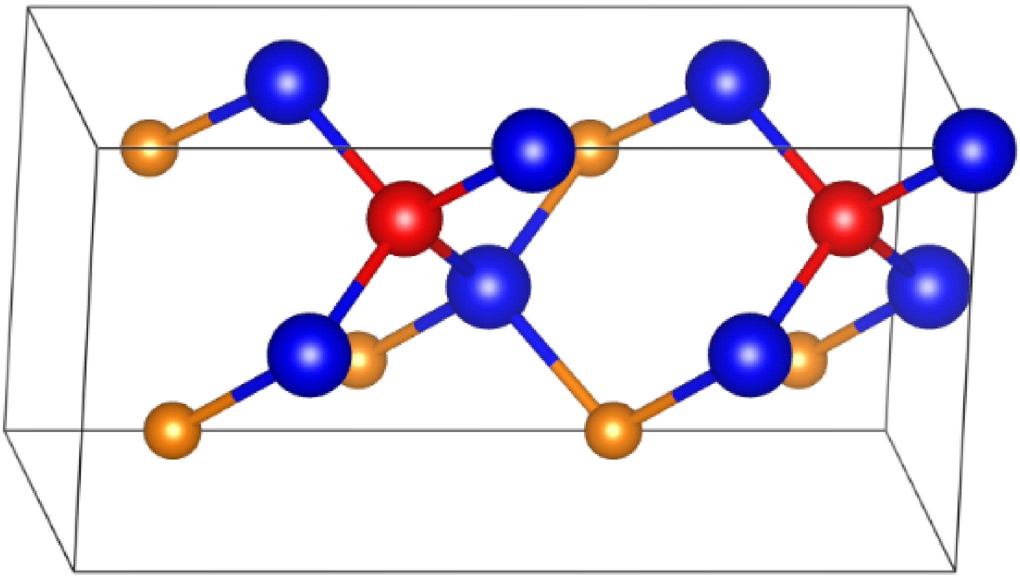

c.

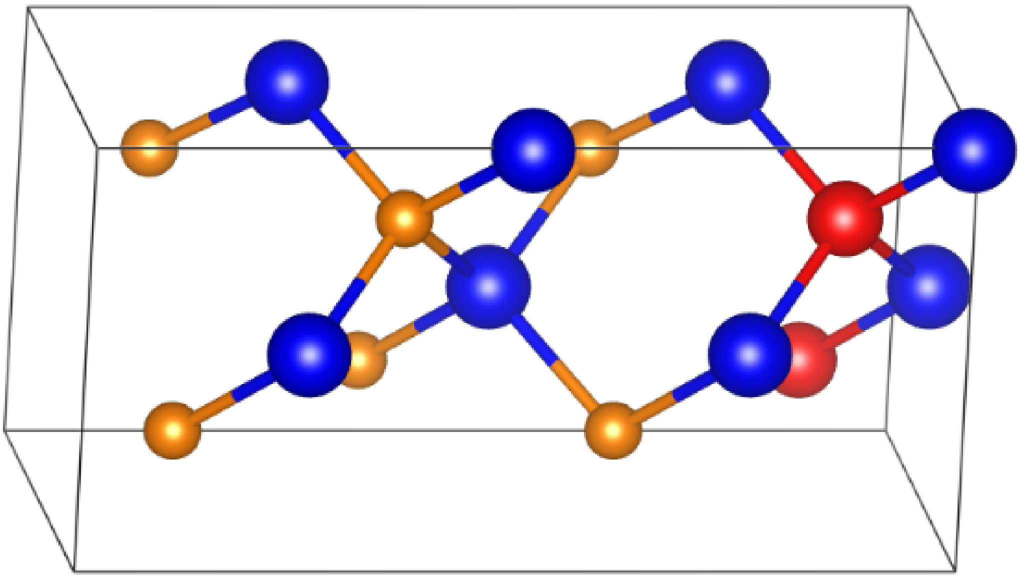

d.

	PBE+D2 energy / eV	PBEsol energy / eV	HSE06 energy / eV	HSE06 band gap / eV	SOC energy / eV	SOC band gap / eV
a	-46.264	-47.922	-53.183	1.4365	-56.161	1.5462
b	-46.276	-47.934	-53.195	1.4567	-56.173	1.5711
c	-46.218	-47.880	-53.144	1.3904	-56.121	1.4995
d	-46.247	-47.906	-53.169	1.3603	-56.147	1.4613

8. $x = 0.875$

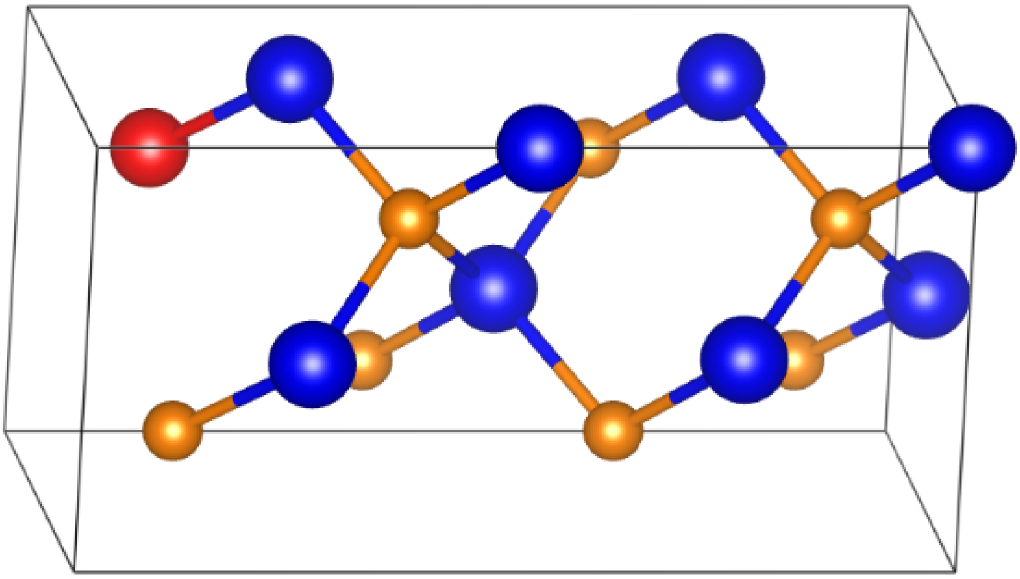

a.

	PBE+D2 energy / eV	PBEsol energy / eV	HSE06 energy / eV	HSE06 band gap / eV	SOC energy / eV	SOC band gap / eV
a	-46.959	-48.655	-54.027	1.4585	-56.959	1.6105

9. $x = 1$

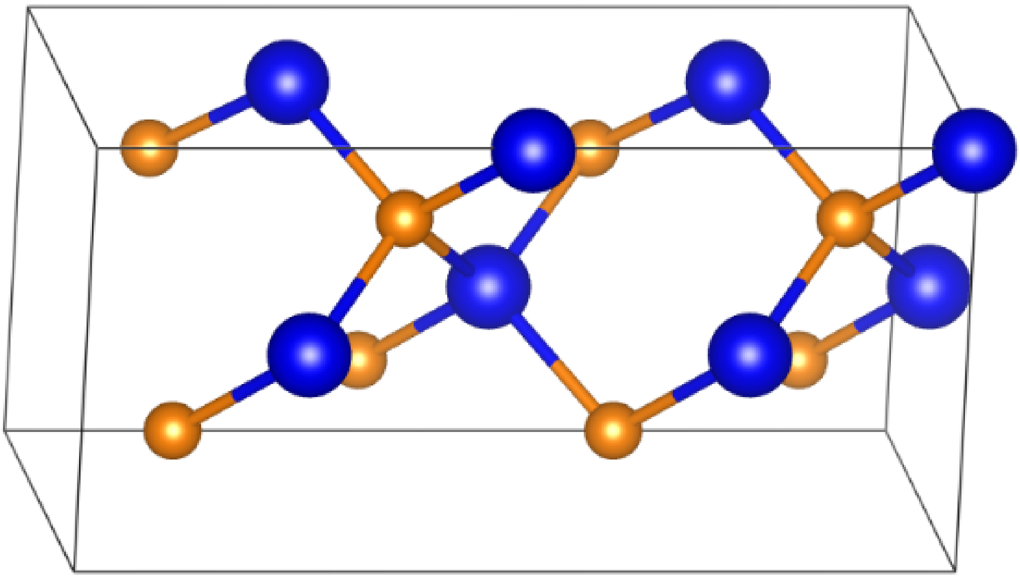

a.

	PBE+D2 energy / eV	PBEsol energy / eV	HSE06 energy / eV	HSE06 band gap / eV	SOC energy / eV	SOC band gap / eV
a	-47.688	-49.426	-54.924	1.5326	-57.791	1.6973

A.2 Wurtzite structures

1. $x = 0$

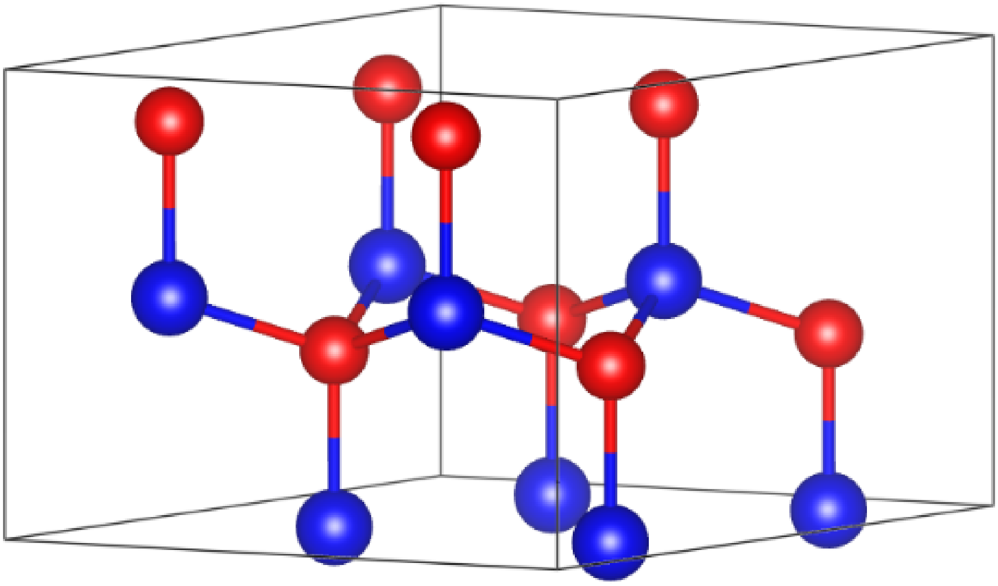

a.

	PBE+D2 energy / eV	PBEsol energy / eV	HSE06 energy / eV	HSE06 band gap / eV	SOC energy / eV	SOC band gap / eV
a	-42.375	-43.851	-48.399	1.5557	-51.725	1.6184

2. $x = 0.125$

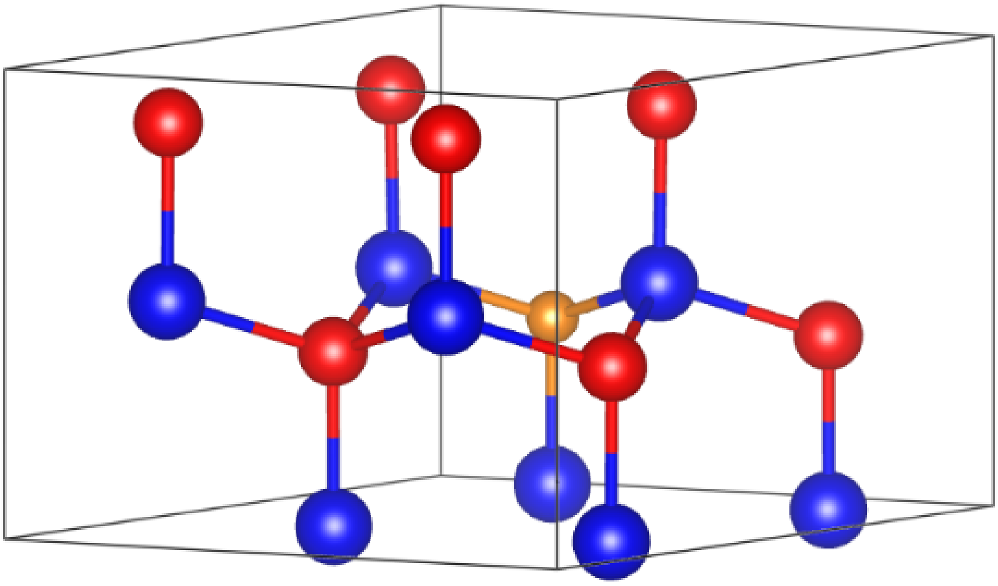

a.

	PBE+D2 energy / eV	PBEsol energy / eV	HSE06 energy / eV	HSE06 band gap / eV	SOC energy / eV	SOC band gap / eV
a	-42.994	-44.482	-49.134	1.4469	-52.396	1.5259

3. $x = 0.25$

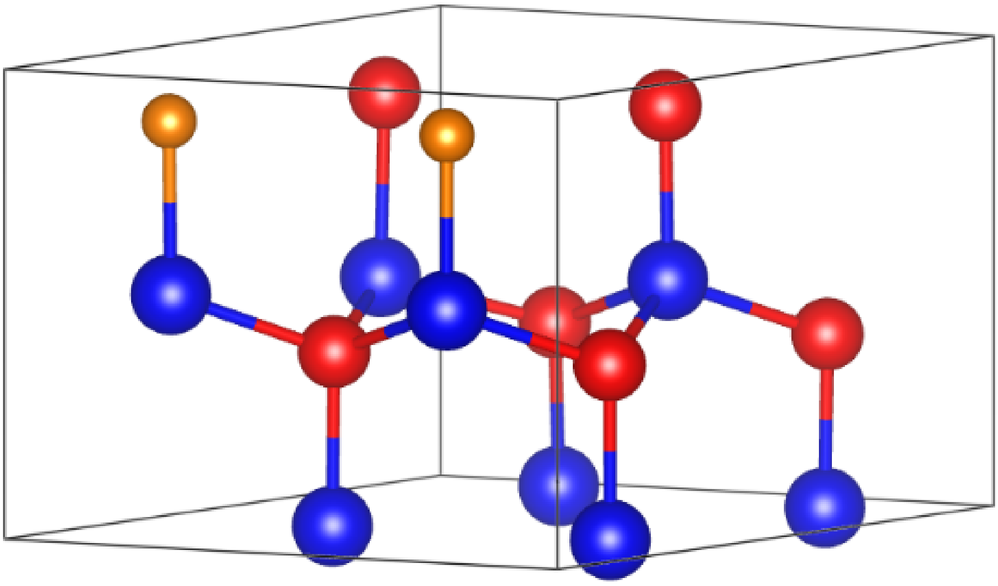

a.

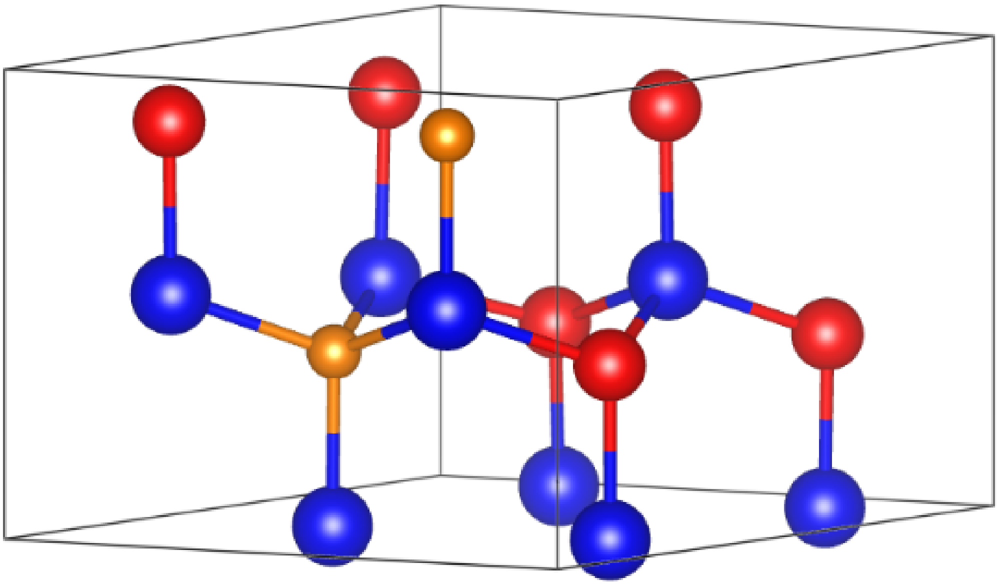

b.

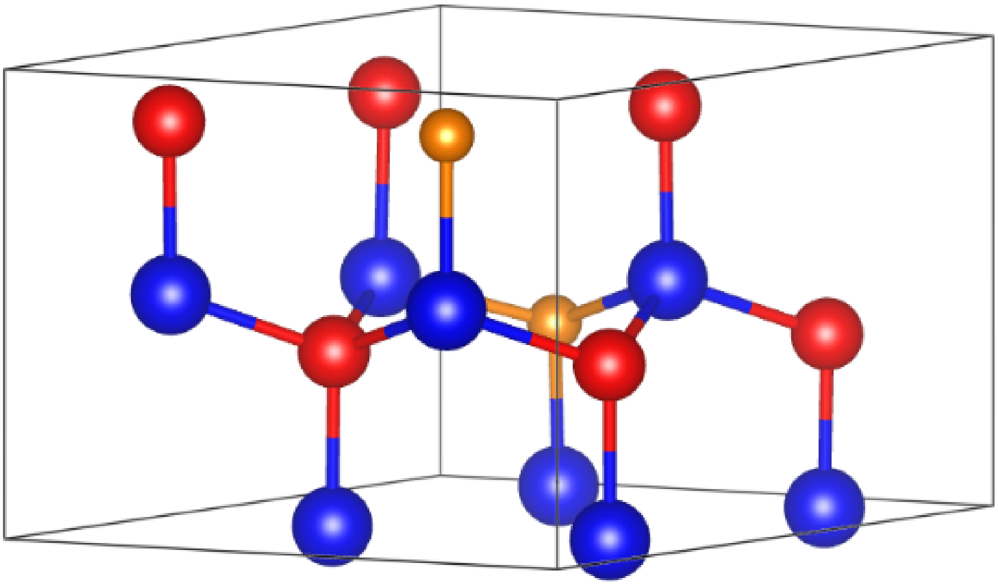

c.

	PBE+D2 energy / eV	PBEsol energy / eV	HSE06 energy / eV	HSE06 band gap / eV	SOC energy / eV	SOC band gap / eV
a	-43.585	-45.097	-49.866	1.3315	-53.062	1.4127
b	-43.606	-45.116	-49.885	1.4224	-53.082	1.5174
c	-43.629	-45.145	-49.920	1.5165	-53.116	1.5888

4. $x = 0.375$

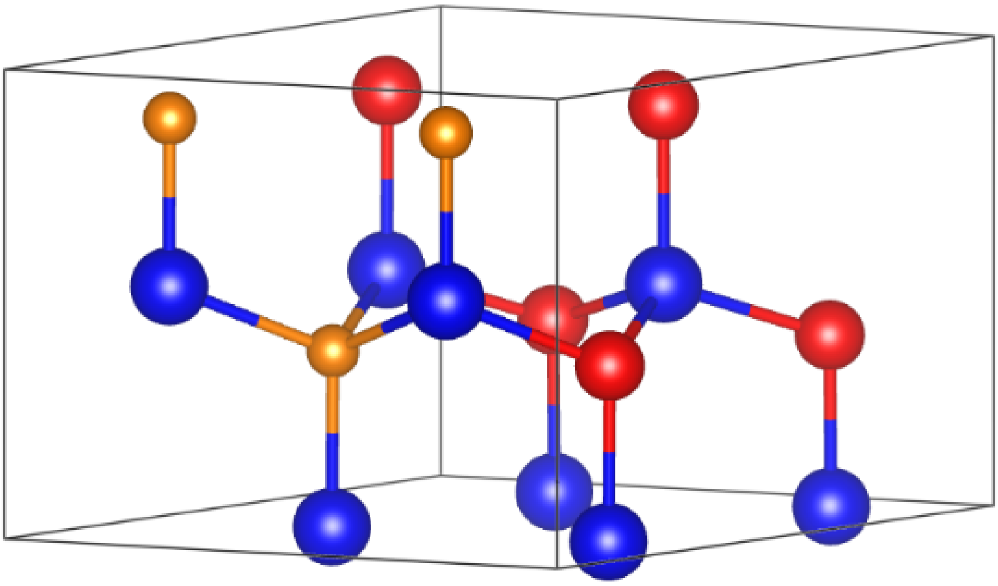

a.

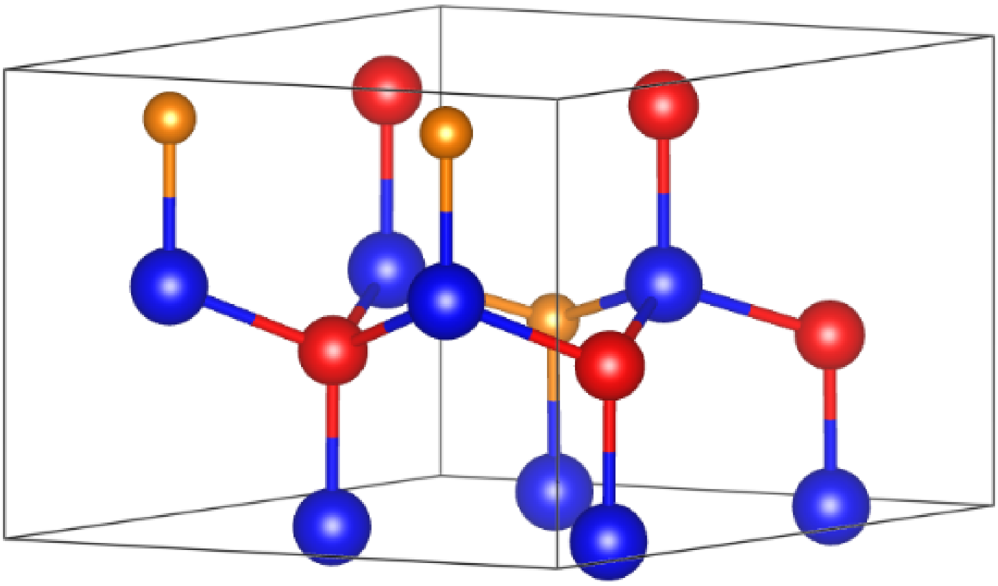

b.

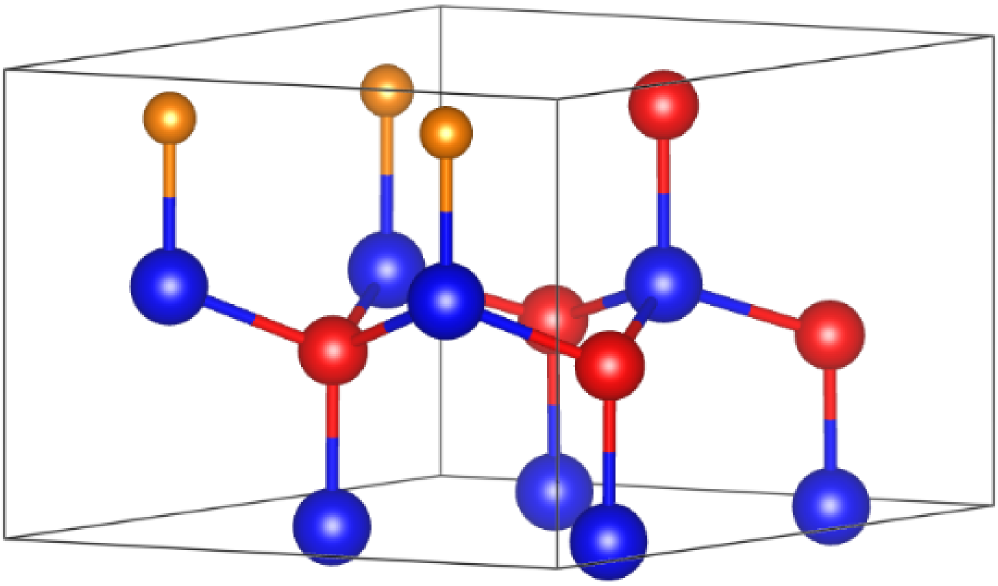

c.

	PBE+D2 energy / eV	PBEsol energy / eV	HSE06 energy / eV	HSE06 band gap / eV	SOC energy / eV	SOC band gap / eV
a	-44.237	-45.768	-50.652	1.3832	-53.785	1.4498
b	-44.259	-45.797	-50.688	1.4966	-53.820	1.5232
c	-44.192	-45.727	-50.615	1.2186	-53.746	1.2794

5. $x = 0.5$

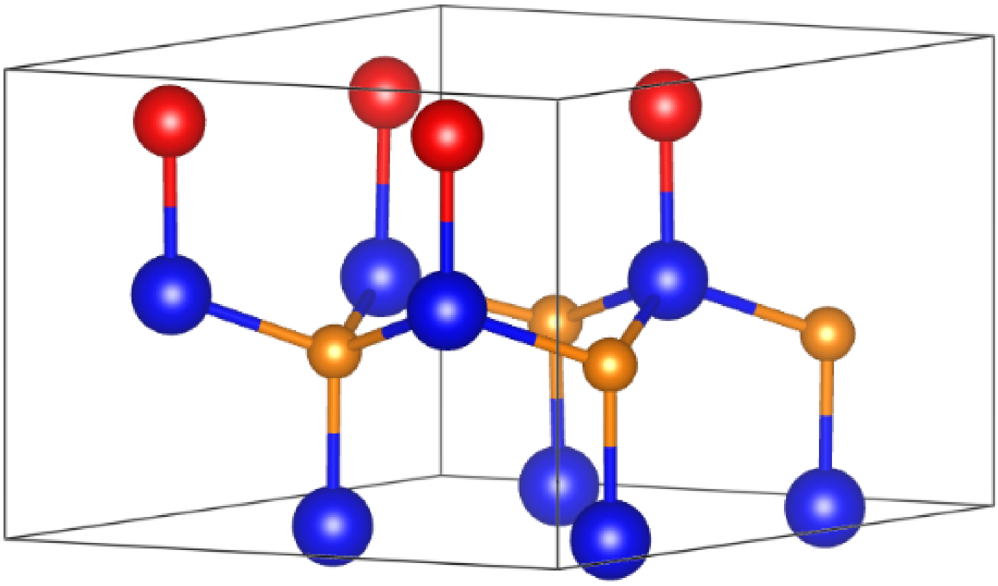

a.

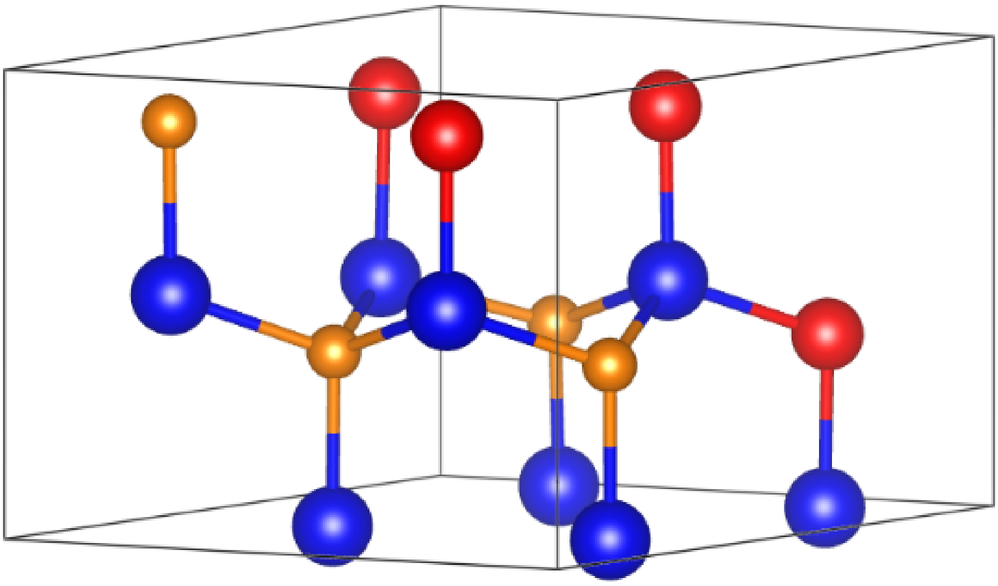

b.

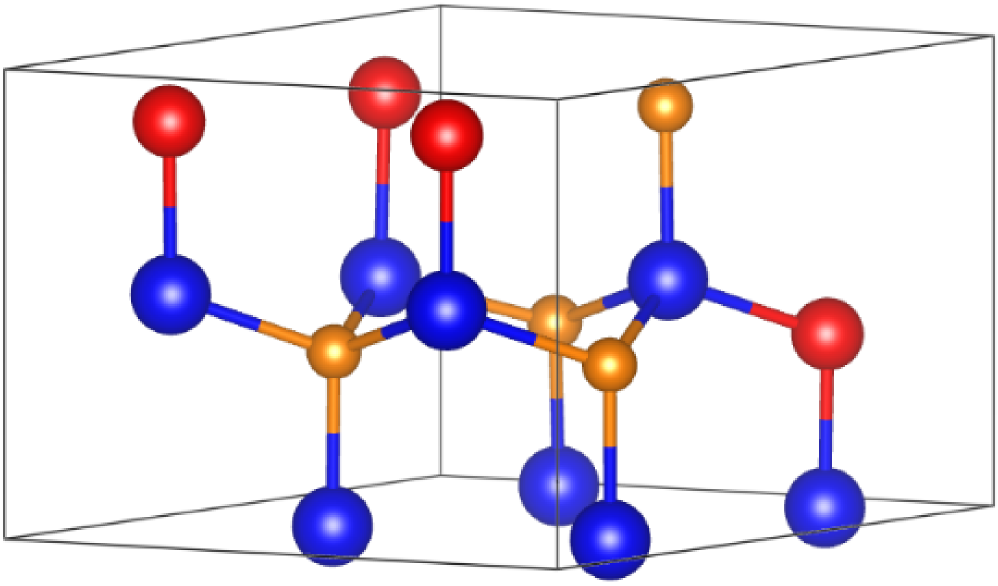

c.

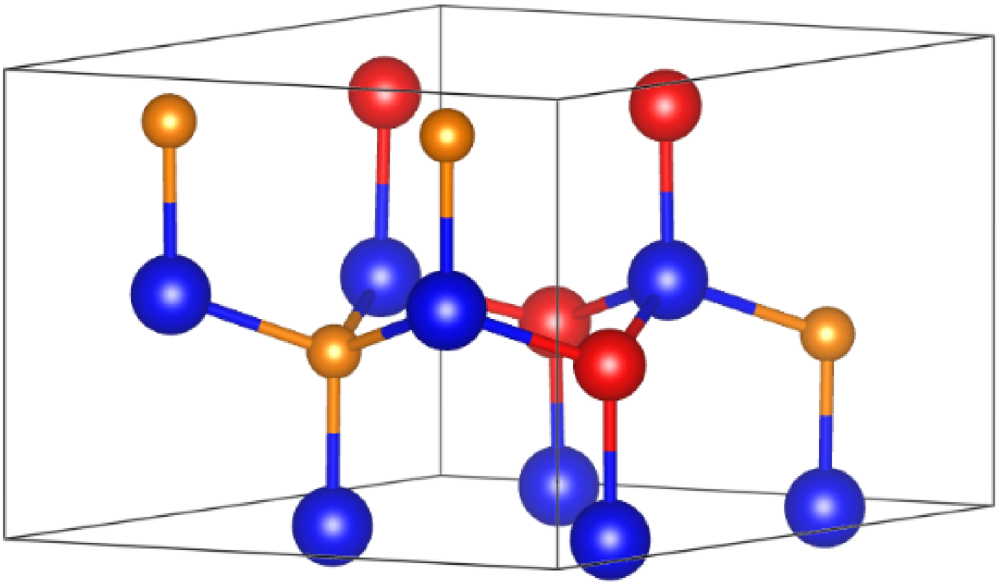

d.

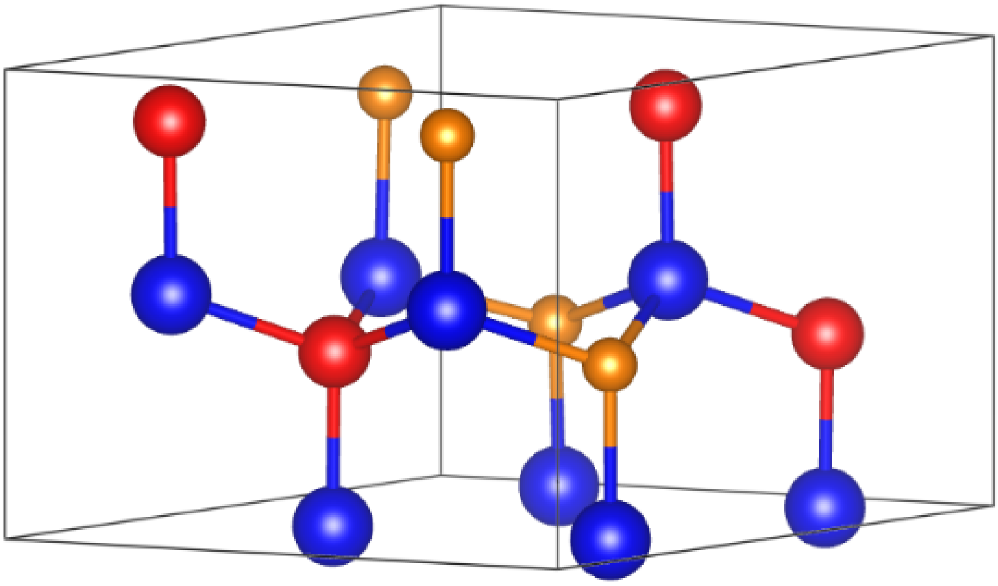

e.

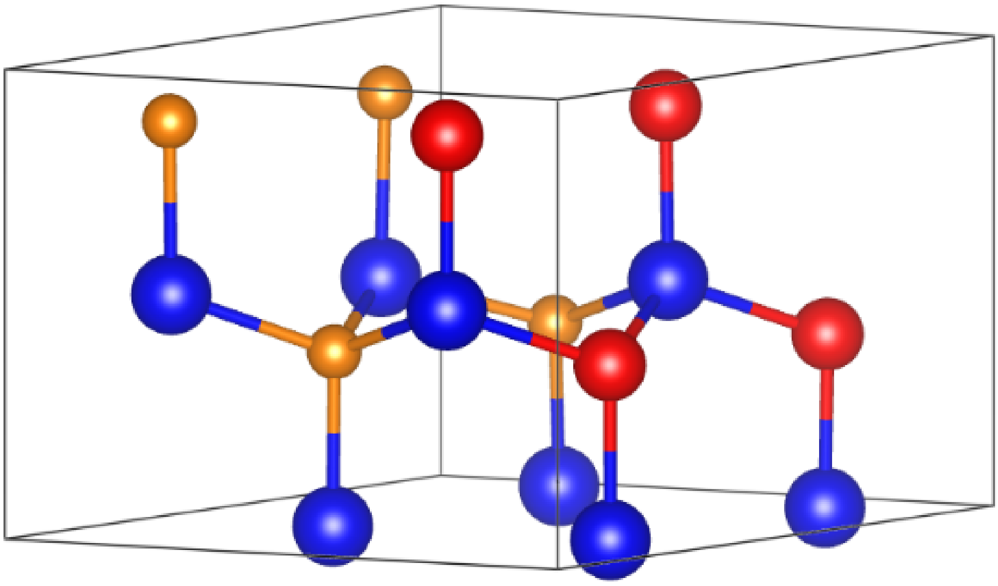

f.

	PBE+D2 energy / eV	PBEsol energy / eV	HSE06 energy / eV	HSE06 band gap / eV	SOC energy / eV	SOC band gap / eV
a	-44.786	-46.352	-51.359	1.0692	-54.427	1.1287
b	-44.856	-46.416	-51.417	1.2884	-54.486	1.3843
c	-44.879	-46.446	-51.454	1.3128	-54.522	1.4280
d	-44.903	-46.468	-51.474	1.3841	-54.543	1.5294
e	-44.925	-46.496	-51.508	1.4512	-54.576	1.5917
f	-44.883	-46.440	-51.438	1.2508	-54.507	1.4175

6. $x = 0.625$

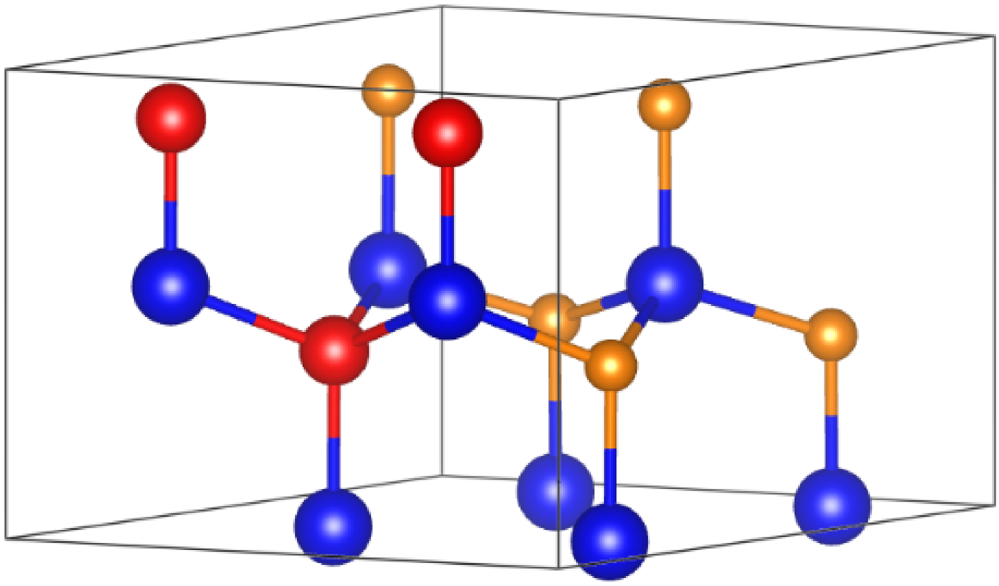

a.

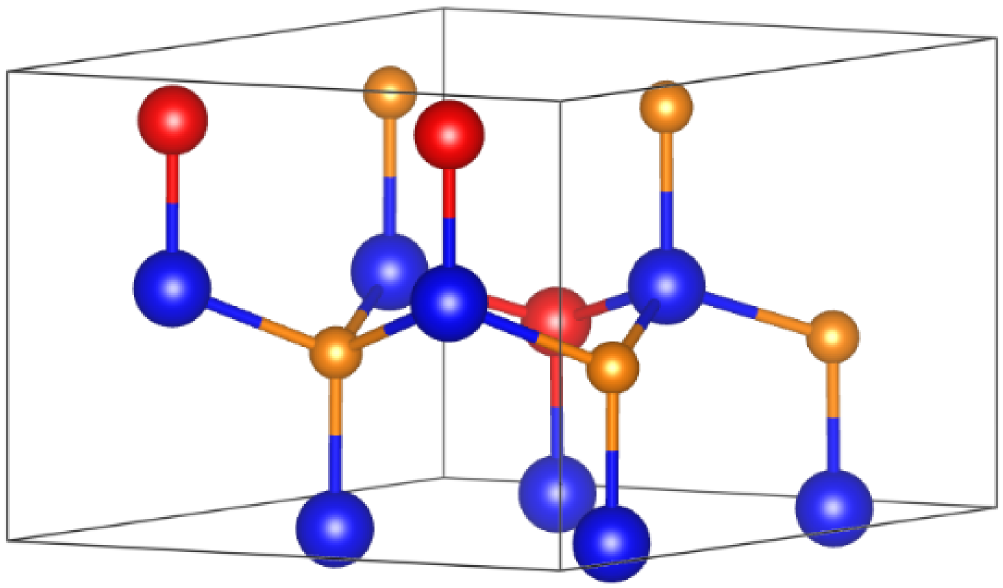

b.

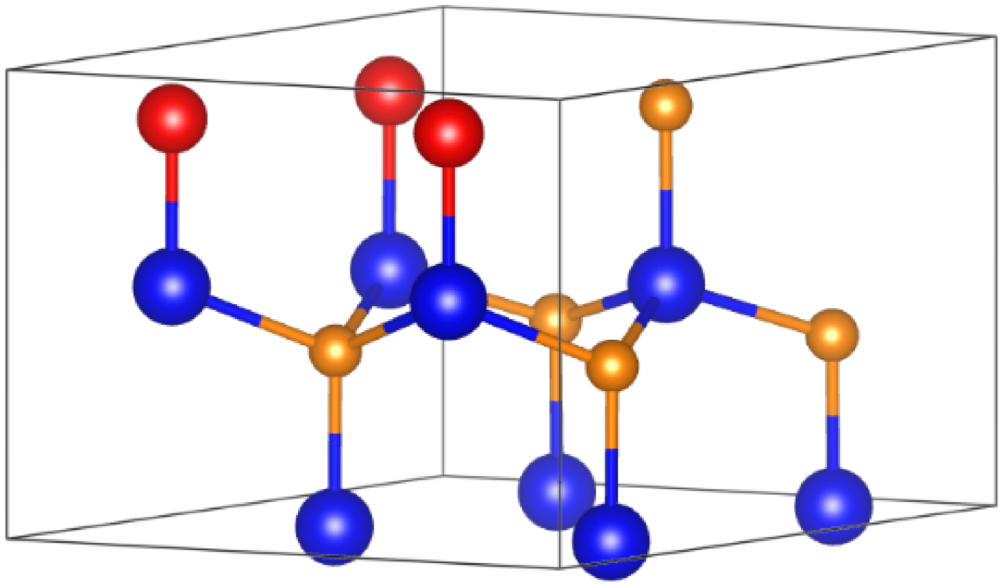

c.

	PBE+D2 energy / eV	PBEsol energy / eV	HSE06 energy / eV	HSE06 band gap / eV	SOC energy / eV	SOC band gap / eV
a	-45.556	-47.150	-52.274	1.3047	-55.279	1.4800
b	-45.577	-47.178	-52.309	1.3977	-55.313	1.5589
c	-45.505	-47.103	-52.232	1.2060	-55.237	1.3039

7. $x = 0.75$

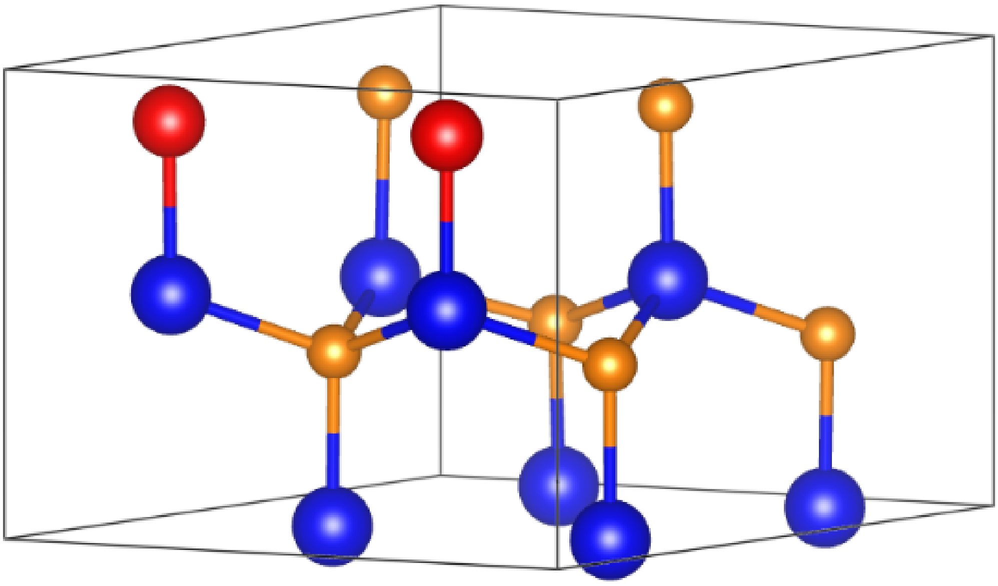

a.

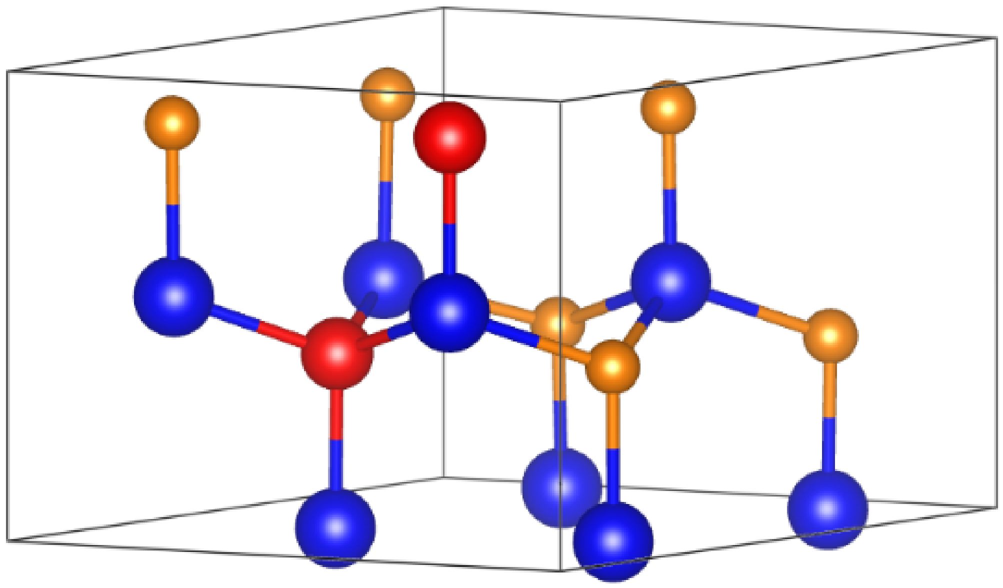

b.

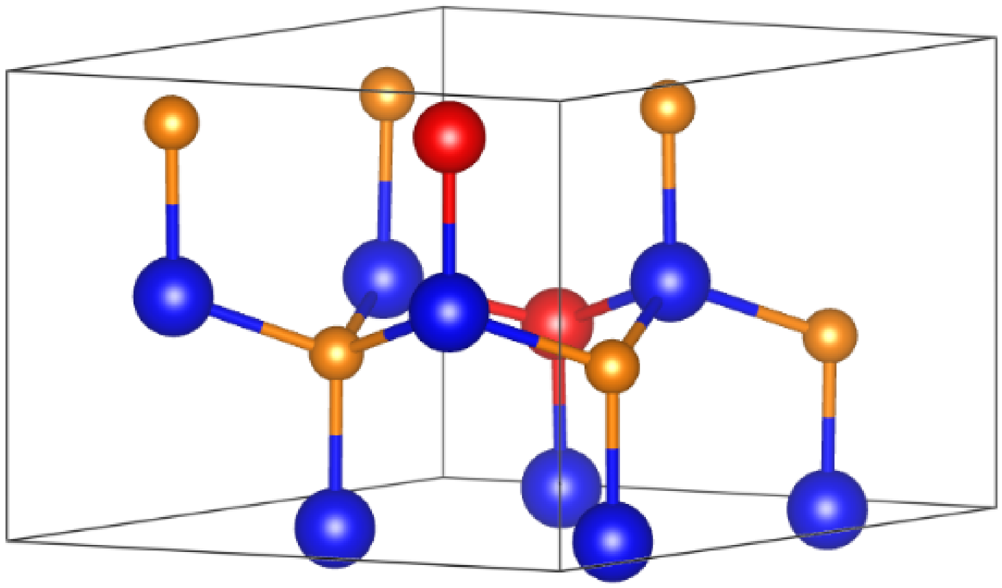

c.

	PBE+D2 energy / eV	PBEsol energy / eV	HSE06 energy / eV	HSE06 band gap / eV	SOC energy / eV	SOC band gap / eV
a	-46.227	-47.861	-53.117	1.2719	-56.058	1.4606
b	-46.254	-47.886	-53.138	1.4471	-56.079	1.6173
c	-46.274	-47.914	-53.168	1.5081	-56.113	1.6872

8. $x = 0.875$

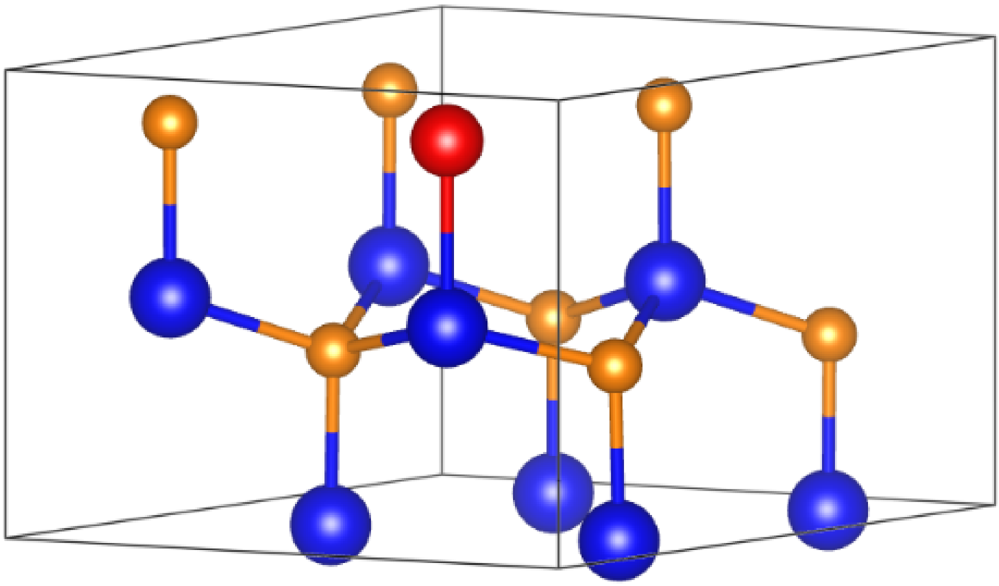

a.

	PBE+D2 energy / eV	PBEsol energy / eV	HSE06 energy / eV	HSE06 band gap / eV	SOC energy / eV	SOC band gap / eV
a	-46.955	-48.630	-54.011	1.4787	-56.892	1.6715

9. $x = 1$

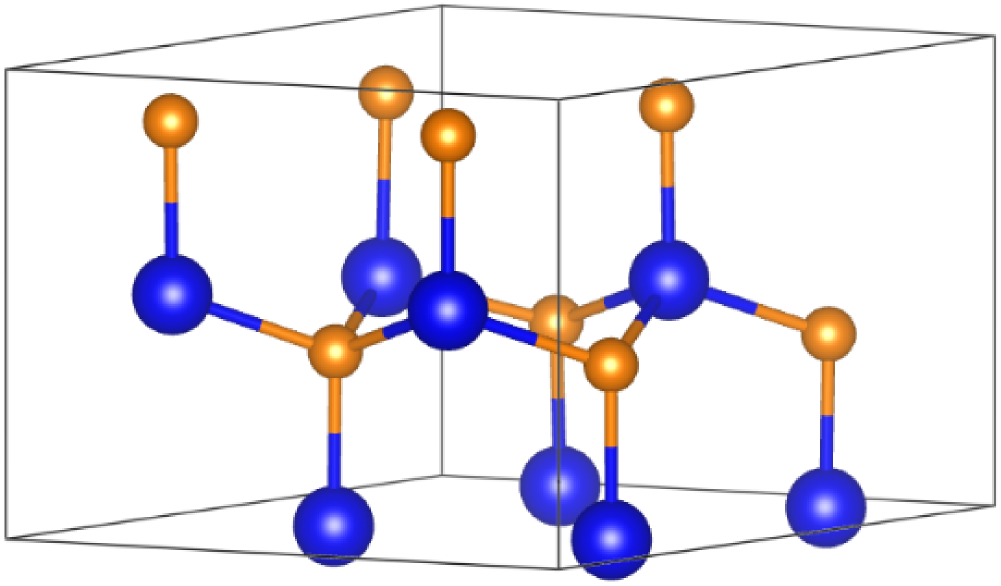

a.

	PBE+D2 energy / eV	PBEsol energy / eV	HSE06 energy / eV	HSE06 band gap / eV	SOC energy / eV	SOC band gap / eV
a	-47.688	-49.408	-54.924	1.6019	-57.741	1.8301

Bibliography

[1] Drew E. Swanson, James R. Sites, and Walajabad S. Sampath. Co-sublimation of CdSe$_x$Te$_{1-x}$ layers for CdTe solar cells. *Solar Energy Materials and Solar Cells*, 159:389 – 394, 2017. ISSN 0927-0248. doi: https://doi.org/10.1016/j.solmat.2016.09.025. URL `http://www.sciencedirect.com/science/article/pii/S0927024816303634`.

[2] G. Fonthal, L. Tirado-Mejía, J.I. Marín-Hurtado, H. Ariza-Calderón, and J.G. Mendoza-Alvarez. Temperature dependence of the band gap energy of crystalline cdte. *Journal of Physics and Chemistry of Solids*, 61(4):579 – 583, 2000. ISSN 0022-3697. doi: https://doi.org/10.1016/S0022-3697(99)00254-1. URL `http://www.sciencedirect.com/science/article/pii/S0022369799002541`.

[3] First Solar, Inc., 2018. URL `http://investor.firstsolar.com/news-releases/news-release-details/first-solar-achieves-yet-another-cell-conversion-efficiency`. Accessed 11/08/20.

[4] William Shockley and Hans J. Queisser. Detailed balance limit of efficiency of p-n junction solar cells. *Journal of Applied Physics*, 32(3):510–519, 1961. doi: 10.1063/1.1736034. URL `https://doi.org/10.1063/1.1736034`.

[5] National Renewable Energy Laboratory Research Cell Efficiency Records, 2020. URL `https://www.nrel.gov/pv/cell-efficiency.html`. Accessed 11/08/20.

[6] Jonathan D. Poplawsky, Wei Guo, Naba Paudel, Amy Ng, Karren More, Donovan Leonard, and Yanfa Yan. Structural and compositional dependence of the CdTe$_x$Se$_{1-x}$ alloy layer photoactivity in CdTe-based solar cells. *Nat Commun*, 7:12537, Jul 2016. ISSN 2041-1723. doi: 10.1038/ncomms12537. URL `http://www.ncbi.nlm.nih.gov/pmc/articles/PMC4974465/`. 27460872[pmid].

[7] J. M. Kephart, A. Kindvall, D. Williams, D. Kuciauskas, P. Dippo, A. Munshi, and W. S. Sampath. Sputter-Deposited Oxides for Interface Passivation of CdTe Photovoltaics. *IEEE Journal of Photovoltaics*, 8(2):587–593, March 2018. ISSN 2156-3381. doi: 10.1109/JPHOTOV.2017.2787021.

[8] Sven Rühle. Tabulated values of the shockley–queisser limit for single junction solar cells. *Solar Energy*, 130(Supplement C):139 – 147, 2016. ISSN 0038-092X. doi: https://doi.org/10.1016/j.solener.2016.02.015. URL `http://www.sciencedirect.com/science/article/pii/S0038092X16001110`.

[9] T Dullweber, G Hanna, U Rau, and H.W Schock. A new approach to high-efficiency solar cells by band gap grading in cu(in,ga)se2 chalcopyrite semiconductors. *Solar Energy Materials and Solar Cells*, 67(1):145 – 150, 2001. ISSN 0927-0248. doi: https://doi.org/10.1016/S0927-0248(00)00274-9. URL `http://www.sciencedirect.com/science/article/pii/S0927024800002749`. PVSEC 11 - PART III.

[10] P. E. Blöchl. Projector augmented-wave method. *Phys. Rev. B*, 50:17953–17979, Dec 1994. doi: 10.1103/PhysRevB.50.17953. URL `https://link.aps.org/doi/10.1103/PhysRevB.50.17953`.

[11] Hendrik J. Monkhorst and James D. Pack. Special points for brillouin-zone integrations. *Phys. Rev. B*, 13:5188–5192, Jun 1976. doi: 10.1103/PhysRevB.13.5188. URL `https://link.aps.org/doi/10.1103/PhysRevB.13.5188`.

[12] Alexandra Szemjonov, Thierry Pauporte, Ilaria Ciofini, and Frederic Labat. Investigation of the bulk and surface properties of cdse: insights from theory. *Phys. Chem. Chem. Phys.*, 16:23251–23259, 2014. doi: 10.1039/C4CP02886D. URL `http://dx.doi.org/10.1039/C4CP02886D`.

[13] Hui Li, Xiangxin Liu, Biao Yang, and Pingjian Wang. Influence of substrate bias and post-deposition cl treatment on cdte film grown by rf magnetron sputtering for solar cells. *RSC Adv.*, 4:5046–5054, 2014. doi: 10.1039/C3RA44831B. URL `http://dx.doi.org/10.1039/C3RA44831B`.

[14] R. B. Kale and C. D. Lokhande. Systematic study on structural phase behavior of cdse thin films. *The Journal of Physical Chemistry B*, 109(43):20288–20294, 2005.

doi: 10.1021/jp053124c. URL http://dx.doi.org/10.1021/jp053124c. PMID: 16853624.

[15] Koichi Momma and Fujio Izumi. *VESTA3* for three-dimensional visualization of crystal, volumetric and morphology data. *Journal of Applied Crystallography*, 44 (6):1272–1276, Dec 2011. doi: 10.1107/S0021889811038970. URL https://doi.org/10.1107/S0021889811038970.

[16] A. Abbas, G. D. West, J. W. Bowers, P. Isherwood, P. M. Kaminski, B. Maniscalco, P. Rowley, J. M. Walls, K. Barricklow, W. S. Sampath, and K. L. Barth. The effect of cadmium chloride treatment on close spaced sublimated cadmium telluride thin film solar cells. In *2012 IEEE 38th Photovoltaic Specialists Conference (PVSC) PART 2*, pages 1–6, June 2012. doi: 10.1109/PVSC-Vol2.2012.6656778.

[17] P. Hohenberg and W. Kohn. Inhomogeneous electron gas. *Phys. Rev.*, 136:B864–B871, Nov 1964. doi: 10.1103/PhysRev.136.B864. URL https://link.aps.org/doi/10.1103/PhysRev.136.B864.

[18] W. Kohn and L. J. Sham. Self-consistent equations including exchange and correlation effects. *Phys. Rev.*, 140:A1133–A1138, Nov 1965. doi: 10.1103/PhysRev.140.A1133. URL https://link.aps.org/doi/10.1103/PhysRev.140.A1133.

[19] John P. Perdew and Karla Schmidt. Jacob's ladder of density functional approximations for the exchange-correlation energy. *AIP Conference Proceedings*, 577(1): 1–20, 2001. doi: 10.1063/1.1390175. URL http://aip.scitation.org/doi/abs/10.1063/1.1390175.

[20] P. A. M. Dirac. Note on exchange phenomena in the thomas atom. *Mathematical Proceedings of the Cambridge Philosophical Society*, 26(3):376–385, 1930. doi: 10.1017/S0305004100016108.

[21] S. H. Vosko, L. Wilk, and M. Nusair. Accurate spin-dependent electron liquid correlation energies for local spin density calculations: a critical analysis. *Canadian Journal of Physics*, 58(8):1200–1211, 1980. doi: 10.1139/p80-159. URL https://doi.org/10.1139/p80-159.

[22] J. P. Perdew and Alex Zunger. Self-interaction correction to density-functional approximations for many-electron systems. *Phys. Rev. B*, 23:5048–5079, May

1981. doi: 10.1103/PhysRevB.23.5048. URL https://link.aps.org/doi/10.1103/PhysRevB.23.5048.

[23] Alain St.-Amant, Wendy D. Cornell, Peter A. Kollman, and Thomas A. Halgren. Calculation of molecular geometries, relative conformational energies, dipole moments, and molecular electrostatic potential fitted charges of small organic molecules of biochemical interest by density functional theory. *Journal of Computational Chemistry*, 16(12):1483–1506, 1995. ISSN 1096-987X. doi: 10.1002/jcc.540161206. URL http://dx.doi.org/10.1002/jcc.540161206.

[24] David C. Patton, Mark R. Pederson, and Dirk V. Porezag. *The Generalized-Gradient Approximation to Density Functional Theory and Bonding*, pages 37–50. Springer Berlin Heidelberg, Berlin, Heidelberg, 1998. ISBN 978-3-642-80478-6. doi: 10.1007/978-3-642-80478-6_3. URL https://doi.org/10.1007/978-3-642-80478-6_3.

[25] John P. Perdew, J. A. Chevary, S. H. Vosko, Koblar A. Jackson, Mark R. Pederson, D. J. Singh, and Carlos Fiolhais. Atoms, molecules, solids, and surfaces: Applications of the generalized gradient approximation for exchange and correlation. *Phys. Rev. B*, 46:6671–6687, Sep 1992. doi: 10.1103/PhysRevB.46.6671. URL https://link.aps.org/doi/10.1103/PhysRevB.46.6671.

[26] J. P. Perdew and Y. Wang. Accurate and simple analytic representation of the electron-gas correlation energy. *Phys. Rev. B*, 45:13244–13249, June 1992. doi: 10.1103/PhysRevB.45.13244.

[27] John P. Perdew, Kieron Burke, and Matthias Ernzerhof. Generalized gradient approximation made simple. *Phys. Rev. Lett.*, 77:3865–3868, Oct 1996. doi: 10.1103/PhysRevLett.77.3865. URL https://link.aps.org/doi/10.1103/PhysRevLett.77.3865.

[28] A. D. Becke. Density-functional exchange-energy approximation with correct asymptotic behavior. *Phys. Rev. A*, 38:3098–3100, Sep 1988. doi: 10.1103/PhysRevA.38.3098. URL https://link.aps.org/doi/10.1103/PhysRevA.38.3098.

[29] Chengteh Lee, Weitao Yang, and Robert G. Parr. Development of the colle-salvetti correlation-energy formula into a functional of the electron density. *Phys. Rev. B*,

37:785–789, Jan 1988. doi: 10.1103/PhysRevB.37.785. URL https://link.aps.org/doi/10.1103/PhysRevB.37.785.

[30] Swapan K. Ghosh and Robert G. Parr. Phase-space approach to the exchange-energy functional of density-functional theory. *Phys. Rev. A*, 34:785–791, Aug 1986. doi: 10.1103/PhysRevA.34.785. URL https://link.aps.org/doi/10.1103/PhysRevA.34.785.

[31] A. D. Becke and M. R. Roussel. Exchange holes in inhomogeneous systems: A coordinate-space model. *Phys. Rev. A*, 39:3761–3767, Apr 1989. doi: 10.1103/PhysRevA.39.3761. URL https://link.aps.org/doi/10.1103/PhysRevA.39.3761.

[32] Stefan Kurth, John P. Perdew, and Peter Blaha. Molecular and solid-state tests of density functional approximations: Lsd, ggas, and meta-ggas. *International Journal of Quantum Chemistry*, 75(4-5):889–909, 1999. ISSN 1097-461X. doi: 10.1002/(SICI)1097-461X(1999)75:4/5⟨889::AID-QUA54⟩3.0.CO;2-8. URL http://dx.doi.org/10.1002/(SICI)1097-461X(1999)75:4/5<889::AID-QUA54>3.0.CO;2-8.

[33] Axel D. Becke. Density-functional thermochemistry. iii. the role of exact exchange. *The Journal of Chemical Physics*, 98(7):5648–5652, 1993. doi: 10.1063/1.464913. URL https://doi.org/10.1063/1.464913.

[34] Axel D. Becke. A new mixing of hartree–fock and local density-functional theories. *The Journal of Chemical Physics*, 98(2):1372–1377, 1993. doi: 10.1063/1.464304. URL https://doi.org/10.1063/1.464304.

[35] P. J. Stephens, F. J. Devlin, C. F. Chabalowski, and M. J. Frisch. Ab initio calculation of vibrational absorption and circular dichroism spectra using density functional force fields. *The Journal of Physical Chemistry*, 98(45):11623–11627, 1994. doi: 10.1021/j100096a001. URL http://dx.doi.org/10.1021/j100096a001.

[36] John P. Perdew, Matthias Ernzerhof, and Kieron Burke. Rationale for mixing exact exchange with density functional approximations. *The Journal of Chemical Physics*, 105(22):9982–9985, 1996. doi: 10.1063/1.472933. URL https://doi.org/10.1063/1.472933.

[37] Jochen Heyd, Gustavo E. Scuseria, and Matthias Ernzerhof. Hybrid functionals based on a screened coulomb potential. *The Journal of Chemical Physics*, 118(18): 8207–8215, 2003. doi: 10.1063/1.1564060. URL `https://doi.org/10.1063/1.1564060`.

[38] Vladimir I. Anisimov, Jan Zaanen, and Ole K. Andersen. Band theory and mott insulators: Hubbard u instead of stoner i. *Phys. Rev. B*, 44:943–954, Jul 1991. doi: 10.1103/PhysRevB.44.943. URL `https://link.aps.org/doi/10.1103/PhysRevB.44.943`.

[39] J. Hubbard. Electron correlations in narrow energy bands. *Proceedings of the Royal Society of London A: Mathematical, Physical and Engineering Sciences*, 276 (1365):238–257, 1963. ISSN 0080-4630. doi: 10.1098/rspa.1963.0204. URL `http://rspa.royalsocietypublishing.org/content/276/1365/238`.

[40] S. L. Dudarev, G. A. Botton, S. Y. Savrasov, C. J. Humphreys, and A. P. Sutton. Electron-energy-loss spectra and the structural stability of nickel oxide: An lsda+u study. *Phys. Rev. B*, 57:1505–1509, Jan 1998. doi: 10.1103/PhysRevB.57.1505. URL `https://link.aps.org/doi/10.1103/PhysRevB.57.1505`.

[41] Nicholas J. Mosey and Emily A. Carter. Ab initio evaluation of coulomb and exchange parameters for dft+u calculations. *Phys. Rev. B*, 76:155123, Oct 2007. doi: 10.1103/PhysRevB.76.155123. URL `https://link.aps.org/doi/10.1103/PhysRevB.76.155123`.

[42] Erich Runge and E. K. U. Gross. Density-functional theory for time-dependent systems. *Phys. Rev. Lett.*, 52:997–1000, Mar 1984. doi: 10.1103/PhysRevLett.52.997. URL `https://link.aps.org/doi/10.1103/PhysRevLett.52.997`.

[43] Robert van Leeuwen. Causality and symmetry in time-dependent density-functional theory. *Phys. Rev. Lett.*, 80:1280–1283, Feb 1998. doi: 10.1103/PhysRevLett.80.1280. URL `https://link.aps.org/doi/10.1103/PhysRevLett.80.1280`.

[44] S.M. Hosseini. Optical properties of cadmium telluride in zinc-blende and wurzite structure. *Physica B: Condensed Matter*, 403(10):1907 – 1915, 2008. ISSN 0921-4526. doi: https://doi.org/10.1016/j.physb.2007.10.370. URL `http://www.sciencedirect.com/science/article/pii/S0921452607012707`.

[45] Su-Hyun Yoo, Keith T. Butler, Aloysius Soon, Ali Abbas, John M. Walls, and Aron Walsh. Identification of critical stacking faults in thin-film cdte solar cells. *Applied Physics Letters*, 105(6):062104, 2014. doi: 10.1063/1.4892844. URL https://doi.org/10.1063/1.4892844.

[46] G. Kresse and J. Furthmüller. Efficient iterative schemes for ab initio total-energy calculations using a plane-wave basis set. *Phys. Rev. B*, 54:11169–11186, Oct 1996. doi: 10.1103/PhysRevB.54.11169. URL https://link.aps.org/doi/10.1103/PhysRevB.54.11169.

[47] Mehmet Aras and Çetin Kılıç. Combined hybrid functional and dft+u calculations for metal chalcogenides. *The Journal of Chemical Physics*, 141(4):044106, 2014. doi: 10.1063/1.4890458. URL https://doi.org/10.1063/1.4890458.

[48] Sándor Kristyán and Péter Pulay. Can (semi)local density functional theory account for the london dispersion forces? *Chemical Physics Letters*, 229(3):175 – 180, 1994. ISSN 0009-2614. doi: https://doi.org/10.1016/0009-2614(94)01027-7. URL http://www.sciencedirect.com/science/article/pii/0009261494010277.

[49] Imad Khan, Iftikhar Ahmad, H.A. Rahnamaye Aliabad, and M. Maqbool. Dft-mbj studies of the band structures of the ii-vi semiconductors. *Materials Today: Proceedings*, 2(10, Part B):5122 – 5127, 2015. ISSN 2214-7853. doi: https://doi.org/10.1016/j.matpr.2015.11.008. URL http://www.sciencedirect.com/science/article/pii/S2214785315009670. International Conference on Solid State Physics 2013 (ICSSP'13).

[50] J. P. Perdew and Alex Zunger. Self-interaction correction to density-functional approximations for many-electron systems. *Phys. Rev. B*, 23:5048–5079, May 1981. doi: 10.1103/PhysRevB.23.5048. URL https://link.aps.org/doi/10.1103/PhysRevB.23.5048.

[51] John P. Perdew, Kieron Burke, and Matthias Ernzerhof. Generalized gradient approximation made simple. *Phys. Rev. Lett.*, 77:3865–3868, Oct 1996. doi: 10.1103/PhysRevLett.77.3865. URL https://link.aps.org/doi/10.1103/PhysRevLett.77.3865.

[52] John P. Perdew, Adrienn Ruzsinszky, Gábor I. Csonka, Oleg A. Vydrov, Gustavo E. Scuseria, Lucian A. Constantin, Xiaolan Zhou, and Kieron Burke. Restoring the

density-gradient expansion for exchange in solids and surfaces. *Phys. Rev. Lett.*, 100:136406, Apr 2008. doi: 10.1103/PhysRevLett.100.136406. URL `https://link.aps.org/doi/10.1103/PhysRevLett.100.136406`.

[53] John P. Perdew, J. A. Chevary, S. H. Vosko, Koblar A. Jackson, Mark R. Pederson, D. J. Singh, and Carlos Fiolhais. Atoms, molecules, solids, and surfaces: Applications of the generalized gradient approximation for exchange and correlation. *Phys. Rev. B*, 46:6671–6687, Sep 1992. doi: 10.1103/PhysRevB.46.6671. URL `https://link.aps.org/doi/10.1103/PhysRevB.46.6671`.

[54] Stefan Grimme. Semiempirical gga-type density functional constructed with a long-range dispersion correction. *Journal of Computational Chemistry*, 27(15):1787–1799, 2006. doi: 10.1002/jcc.20495. URL `https://onlinelibrary.wiley.com/doi/abs/10.1002/jcc.20495`.

[55] Stefan Grimme, Jens Antony, Stephan Ehrlich, and Helge Krieg. A consistent and accurate ab initio parametrization of density functional dispersion correction (dft-d) for the 94 elements h-pu. *The Journal of Chemical Physics*, 132(15):154104, 2010. doi: 10.1063/1.3382344. URL `https://doi.org/10.1063/1.3382344`.

[56] Stefan Grimme, Stephan Ehrlich, and Lars Goerigk. Effect of the damping function in dispersion corrected density functional theory. *Journal of Computational Chemistry*, 32(7):1456–1465, 2011. doi: 10.1002/jcc.21759. URL `https://onlinelibrary.wiley.com/doi/abs/10.1002/jcc.21759`.

[57] Alexandre Tkatchenko and Matthias Scheffler. Accurate molecular van der waals interactions from ground-state electron density and free-atom reference data. *Phys. Rev. Lett.*, 102:073005, Feb 2009. doi: 10.1103/PhysRevLett.102.073005. URL `https://link.aps.org/doi/10.1103/PhysRevLett.102.073005`.

[58] Alexandre Tkatchenko, Robert A. DiStasio, Roberto Car, and Matthias Scheffler. Accurate and efficient method for many-body van der waals interactions. *Phys. Rev. Lett.*, 108:236402, Jun 2012. doi: 10.1103/PhysRevLett.108.236402. URL `https://link.aps.org/doi/10.1103/PhysRevLett.108.236402`.

[59] Stephan N. Steinmann and Clemence Corminboeuf. A generalized-gradient approximation exchange hole model for dispersion coefficients. *The Journal of*

Chemical Physics, 134(4):044117, 2011. doi: 10.1063/1.3545985. URL https://doi.org/10.1063/1.3545985.

[60] L. Vegard. Die Konstitution der Mischkristalle und die Raumfüllung der Atome. *Zeitschrift fur Physik*, 5(1):17–26, Jan 1921. doi: 10.1007/BF01349680.

[61] Mao-Hua Du. Density functional calculations of native defects in ch3nh3pbi3: Effects of spin–orbit coupling and self-interaction error. *The Journal of Physical Chemistry Letters*, 6(8):1461–1466, 2015. doi: 10.1021/acs.jpclett.5b00199. URL https://doi.org/10.1021/acs.jpclett.5b00199. PMID: 26263152.

[62] D. West, Y. Y. Sun, Han Wang, Junhyeok Bang, and S. B. Zhang. Native defects in second-generation topological insulators: Effect of spin-orbit interaction on $\mathrm{bi}_2\mathrm{se}_3$. *Phys. Rev. B*, 86:121201, Sep 2012. doi: 10.1103/PhysRevB.86.121201. URL https://link.aps.org/doi/10.1103/PhysRevB.86.121201.

[63] Zhi Gen Yu and Yong-Wei Zhang. Effect of spin-orbit coupling on formation of native defects in weyl fermion semimetals: The case of tx $(t = \mathrm{Ta},\ \mathrm{Nb}; x = \mathrm{As},\ p)$. *Phys. Rev. B*, 94:195206, Nov 2016. doi: 10.1103/PhysRevB.94.195206. URL https://link.aps.org/doi/10.1103/PhysRevB.94.195206.

[64] E. Menéndez-Proupin, M. Casanova-Páez, A.L. Montero-Alejo, M.A. Flores, and W. Orellana. Symmetry and thermodynamics of tellurium vacancies in cadmium telluride. *Physica B: Condensed Matter*, 2019. ISSN 0921-4526. doi: https://doi.org/10.1016/j.physb.2019.01.013. URL http://www.sciencedirect.com/science/article/pii/S0921452619300134.

[65] Jie Pan, Wyatt K. Metzger, and Stephan Lany. Spin-orbit coupling effects on predicting defect properties with hybrid functionals: A case study in cdte. *Phys. Rev. B*, 98:054108, Aug 2018. doi: 10.1103/PhysRevB.98.054108. URL https://link.aps.org/doi/10.1103/PhysRevB.98.054108.

[66] Thomas A. M. Fiducia, Budhika G. Mendis, Kexue Li, Chris R. M. Grovenor, Amit H. Munshi, Kurt Barth, Walajabad S. Sampath, Lewis D. Wright, Ali Abbas, Jake W. Bowers, and John M. Walls. Understanding the role of selenium in defect passivation for highly efficient selenium-alloyed cadmium telluride solar cells. *Nature Energy*, 4(6):504–511, Jun 2019. ISSN 2058-7546. doi: 10.1038/s41560-019-0389-z. URL https://doi.org/10.1038/s41560-019-0389-z.

[67] J.M. Sanchez, F. Ducastelle, and D. Gratias. Generalized cluster description of multicomponent systems. *Physica A: Statistical Mechanics and its Applications*, 128(1):334 – 350, 1984. ISSN 0378-4371. doi: https://doi.org/10.1016/0378-4371(84)90096-7. URL http://www.sciencedirect.com/science/article/pii/0378437184900967.

[68] A. van de Walle. Multicomponent multisublattice alloys, nonconfigurational entropy and other additions to the Alloy Theoretic Automated Toolkit. *Calphad*, 33:266–278, 2009. doi: 10.1016/j.calphad.2008.12.005.

[69] A. van de Walle, M. D. Asta, and G. Ceder. The Alloy Theoretic Automated Toolkit: A user guide. *Calphad*, 26:539–553, 2002. doi: 10.1016/S0364-5916(02)80006-2.

[70] A. van de Walle and G. Ceder. Automating first-principles phase diagram calculations. *J. Phase Equilib.*, 23:348–359, 2002. doi: 10.1361/105497102770331596.

[71] A. van de Walle and M. D. Asta. Self-driven lattice-model monte carlo simulations of alloy thermodynamic properties and phase diagrams. *Model. Simul. Mater. Sc.*, 10:521, 2002. doi: 10.1088/0965-0393/10/5/304.

[72] A. van de Walle, P. Tiwary, M. M. de Jong, D. L. Olmsted, M. D. Asta, A. Dick, D. Shin, Y. Wang, L.-Q. Chen, and Z.-K. Liu. Efficient stochastic generation of special quasirandom structures. *Calphad*, 42:13–18, 2013. doi: 10.1016/j.calphad.2013.06.006.

[73] Alex Zunger, S.-H. Wei, L. G. Ferreira, and James E. Bernard. Special quasirandom structures. *Phys. Rev. Lett.*, 65:353–356, Jul 1990. doi: 10.1103/PhysRevLett.65.353. URL https://link.aps.org/doi/10.1103/PhysRevLett.65.353.

[74] Steve Plimpton. Fast parallel algorithms for short-range molecular dynamics. *J. Comput. Phys.*, 117(1):1–19, March 1995. ISSN 0021-9991. doi: 10.1006/jcph.1995.1039. URL http://dx.doi.org/10.1006/jcph.1995.1039.

[75] R Grau-Crespo, S Hamad, C R A Catlow, and N H de Leeuw. Symmetry-adapted configurational modelling of fractional site occupancy in solids. *Journal of Physics: Condensed Matter*, 19(25):256201, may 2007. doi: 10.1088/0953-8984/19/25/256201. URL https://doi.org/10.1088%2F0953-8984%2F19%2F25%2F256201.

[76] X. W. Zhou, M. E. Foster, F. B. van Swol, J. E. Martin, and Bryan M. Wong. Analytical bond-order potential for the cd–te–se ternary system. *The Journal of Physical Chemistry C*, 118(35):20661–20679, Sep 2014. ISSN 1932-7447. doi: 10.1021/jp505915u. URL https://doi.org/10.1021/jp505915u.

[77] M. A. Berding. Native defects in CdTe. *Phys. Rev. B*, 60:8943–8950, Sep 1999. doi: 10.1103/PhysRevB.60.8943. URL https://link.aps.org/doi/10.1103/PhysRevB.60.8943.

[78] Li Yujie, Ma Guoli, and Jie Wanqi. Point defects in CdTe. *Journal of Crystal Growth*, 256(3):266 – 275, 2003. ISSN 0022-0248. doi: https://doi.org/10.1016/S0022-0248(03)01373-3. URL http://www.sciencedirect.com/science/article/pii/S0022024803013733.

[79] W. Shockley and W. T. Read. Statistics of the recombinations of holes and electrons. *Phys. Rev.*, 87:835–842, Sep 1952. doi: 10.1103/PhysRev.87.835. URL https://link.aps.org/doi/10.1103/PhysRev.87.835.

[80] Ji-Hui Yang, Lin Shi, Lin-Wang Wang, and Su-Huai Wei. Non-radiative carrier recombination enhanced by two-level process: A first-principles study. *Scientific Reports*, 6:21712 EP –, Feb 2016. URL http://dx.doi.org/10.1038/srep21712. Article.

[81] Li-Bo Han, Qi An, Rong-Shan Fu, Lianqing Zheng, and Sheng-Nian Luo. Melting of defective cu with stacking faults. *The Journal of Chemical Physics*, 130:024508, 02 2009.

[82] Michael Watts, Thomas Fiducia, Biplab Sanyal, Roger Smith, Michael Walls, and Pooja Goddard. Enhancement of photovoltaic efficiency in $CdSe_xTe_{1-x}$ (where $0 \leq x \leq 1$): insights from density functional theory. *J. Phys. Condensed Matter*, 32:125702, March 2020. URL https://doi.org/10.1088/1361-648X/ab5bba.